Adaptive Fringe Projection and Error-Compensated Calibration for Compact 3D Shape-Measurement Systems

by

Dong Li

A thesis
presented to the University of Waterloo
in fulfillment of the
thesis requirement for the degree of
Doctor of Philosophy
in
Systems Design Engineering

Waterloo, Ontario, Canada, 2014

AUTHOR'S DECLARATION

I hereby declare that I am the sole author of this thesis. This is a true copy of the thesis, including any required final revisions, as accepted by my examiners.

I understand that my thesis may be made electronically available to the public.

Abstract

Measurement of the three-dimensional (3-D) shape of an object is needed for both industrial and consumer applications. In industrial applications, compact measurement systems are needed to accomplish certain tasks such as measuring an interior surface in a confined space. In consumer applications, compact measurement systems are also needed for common consumers to conveniently get access to 3D data for a wide range of everyday uses. Fringe-projection techniques have been increasingly used for 3D shape measurement due to the advantage of dense full-field measurement.

For a camera-projector measurement system, system geometry (the relative camera-projector position and angle) determine the system compactness. Analysis of the relation of system geometry to measurement accuracy is challenging owing to the effect of the various factors that vary with system geometry on measurement accuracy. It is thus necessary to experimentally determine how measurement accuracy varies with system geometry, in order to determine the most compact design that satisfies a desired measurement accuracy. This has been achieved in a compactness study, in which the measurement accuracy is evaluated at different relative camera-projector positions and angles.

Measurement results in the compactness study have shown that there is a tradeoff in loss of accuracy for increased compactness and loss of compactness for increased accuracy. The smallest camera-projector angle (for an industrial system) or the smallest physical distance between the camera and projector (for a consumer system) that satisfies the desired accuracy would provide the most compact design. Several new methods including 1) an improved heterodyne phase-unwrapping method, 2) an adaptive fringe-pattern projection (AFPP) method for surfaces of high variation in reflectivity and illumination, and 3) a pixel-wise adaptive fringe-pattern projection (PWAFPP) method for such surfaces, have been developed in this research to improve measurement accuracy, thus contributing to enable a more compact system design to achieve a desired measurement accuracy.

First, the new improved heterodyne phase-unwrapping method detects and compensates for the spike-like errors in absolute phase maps. The method has demonstrated improved

projector calibration accuracy from 18.2 to 0.2 pixels, thus ensuring usable camera-projector stereovision system calibration for 3D measurement. Second, the new AFPP method adapts the projector maximum input gray levels (MIGLs) to local surface reflectivity using only two prior fringe-pattern projection and image-capture rounds. The method demonstrated greatly improved 3D measurement accuracy by avoiding image saturation in highly-reflective surface regions while maintaining high intensity modulation of captured fringe patterns across the entire surface with large range in reflectivity. Third, the new PWAFPP method projects a MIGL adapted to the surface reflectivity and illuminance for each pixel. The method has demonstrated a 34% root-mean-square (RMS) error reduction in 3D measurement for pixels that remained saturated after applying the AFPP method. The new method can thus be used to measure surfaces with more complex variation in surface reflectivity.

Acknowledgements

I would like to thank Professor Jonathan Kofman for his supervision of my PhD thesis research. I would also like to thank my parents for their support and love.

This research has been funded by the Natural Sciences and Engineering Research Council of Canada.

Table of Contents

List of Figures

List of Tables

Chapter 1
Introduction

Measurement of the three-dimensional (3D) shape of an object is needed for diverse applications including reverse engineering, manufacturing inspection, biomedicine, cultural heritage acquisition, architecture, and computer animation [1]. Optical methods, such as triangulation-based structured-light methods [2], have been commonly used because of the advantage of being non-contacting.

Laser range sensing has been among the most commonly used structured-light methods for decades. A single-line laser range sensor [3] projects a laser stripe onto the object surface, as illustrated in Figure 1-1. A camera with an offset angle from the projector captures an image of the laser stripe that appears distorted in the captured image. The 3D coordinate of every sampled point on the deformed laser stripe can then be calculated by triangulation. One drawback of a single-line laser range sensor is that the laser stripe has to be swept across the object surface and many images must thus be acquired to measure the entire object surface. This makes the surface 3D coordinate data acquisition time-consuming.

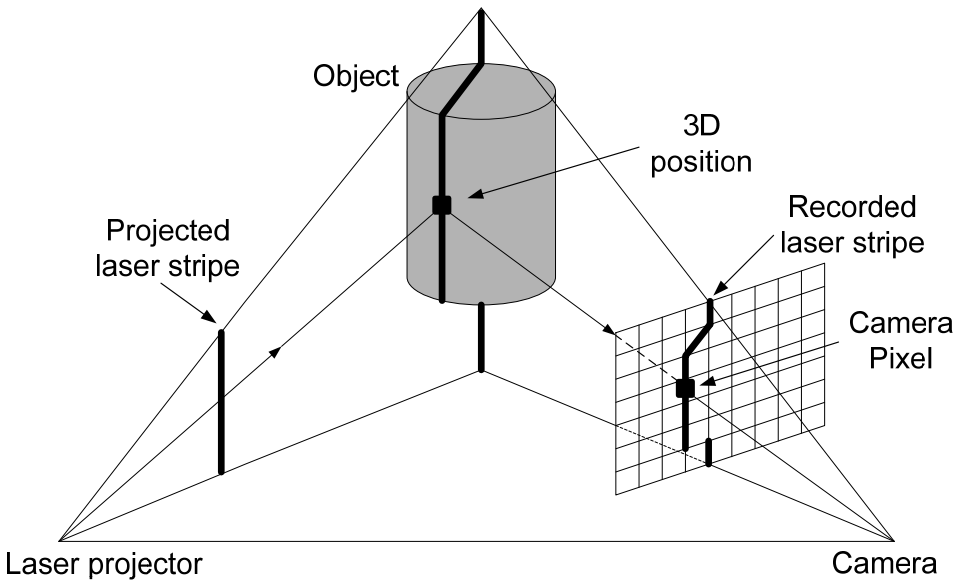

Figure 1-1 Single-line triangulation between a laser projector and a camera.

A multiple-line laser range sensor [4] projects multiple laser stripes simultaneously onto an object surface. The advantage of multiple-line laser range sensors is speed of acquisition, since a single image can acquire data for multiple lines simultaneously. However, there is a problem of low measurement resolution due to laser-stripe spacing. The surface geometric information between laser stripes can only be obtained by interpolation through surface fitting [3].

Fringe projection profilometry (FPP) [5-9] uses spatially-continuous intensity-profile light patterns. Compared with laser range-sensing, fringe-projection techniques offer the advantage of dense full-field measurement, which permits acquisition of 3D coordinates for every camera pixel simultaneously. A camera-projector system that implements fringe projection techniques for 3D shape measurement is referred to as a 3D scanner hereinafter.

1.1 Overview of Fringe-Projection Techniques

1.1.1 3D Surface-Shape Measurement Fundamentals

Many fringe projection techniques have been proposed to measure the surface shape of an object, such as phase-shifting profilometry (PSP) [6], spatial carrier profilometry (SCP) [7], Fourier-transform profilometry (FTP) [8] and wavelet-transform profilometry (WTP) [9]. These techniques use different algorithms to compute phase from images of patterns projected onto a surface. The phase contains information of the surface geometry and is thus important in 3D surface reconstruction (explained further in Section 1.1.2).

The above techniques have been compared based on the number of required patterns, measurement resolution, and measurement accuracy [10-12]. Among these techniques, PSP, which implements a phase-shifting algorithm to compute phase, provides high measurement resolution and accuracy at a cost of requiring projection and capture of multiple patterns. SCP is a single-pattern technique, where the phase-shifting algorithm is applied to sub-sampled images derived from the original single image. This technique has reduced resolution due to the down-sampling of the original image for phase computation and low phase measurement accuracy particularly at abrupt geometric and surface-reflectivity variations on a surface. FTP is another single-pattern technique, where the phase can be

computed from the inverse transform of the band-filtered frequency components of the fringe pattern. The method is sensitive to noise when the noise is at the frequency of the fringe pattern. WTP performs better than FTP in noise suppression because it retrieves the phase from the most reliable point of the local spectrum, however with complex computation [11]. PSP was used in this research for its high measurement resolution and accuracy to measure surfaces with large geometric discontinuity and large range in reflectivity.

A typical 3D scanner based on PSP is shown schematically in Figure 1-2. It consists of a digital projector for projection of computer-generated fringe patterns, a digital camera for acquisition of the reflected fringe patterns at an angle from the projector direction, and a computer for system control and data processing. PSP involves two main procedures: the system calibration and 3D measurement of the surface of interest, as shown in Figure 1-3.

The system calibration is a process that determines the relationship between an absolute phase distribution (detailed in the next section) and the surface 3D coordinates, and only needs to be carried out once to permit unlimited number of 3D shape measurements.

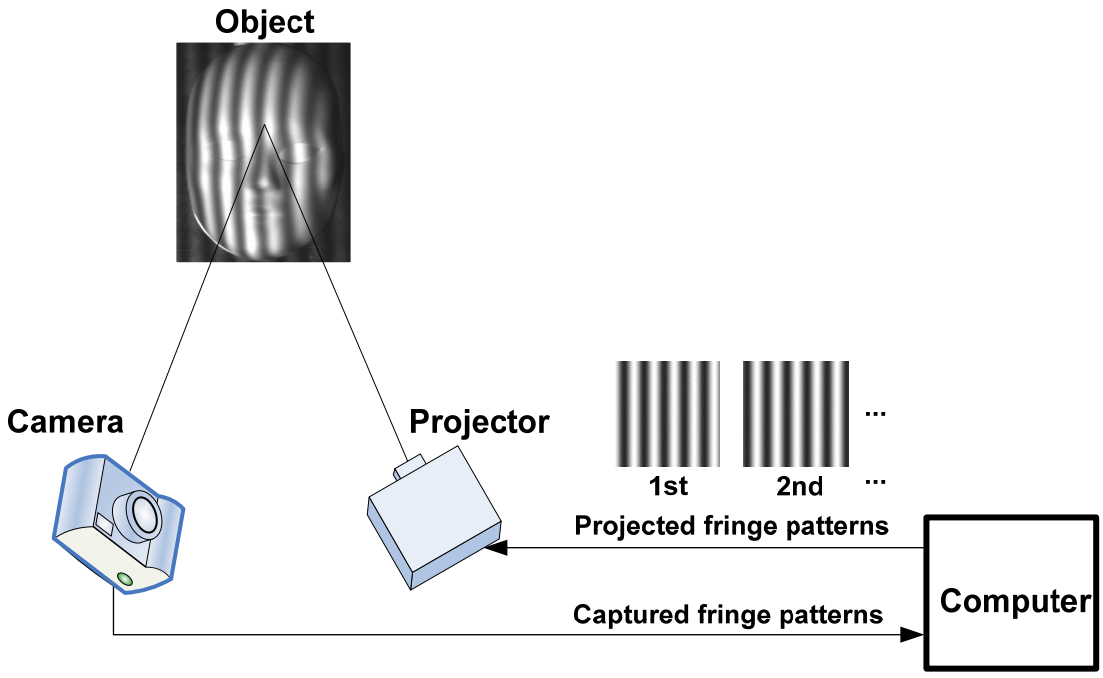

Figure 1-2 Schematic diagram of a PSP system.

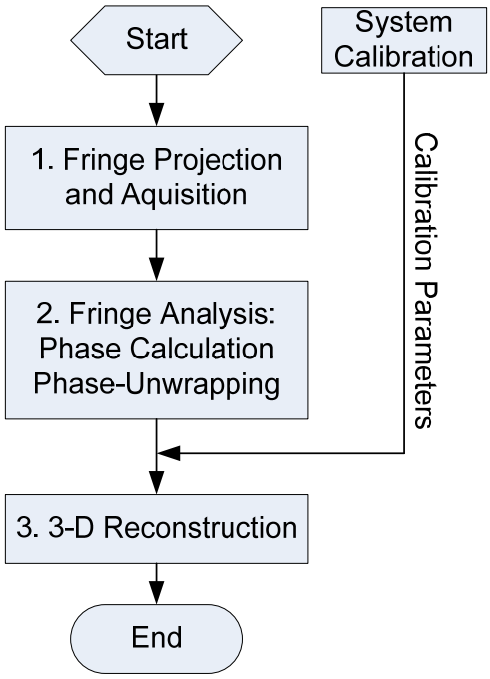

Figure 1-3 Flowchart of a 3D shape measurement using PSP.

The process of a 3D shape measurement involves three main steps: (1) generation and projection of the fringe patterns onto the object surface and image acquisition of the distorted patterns on the object surface; (2) fringe analysis, which includes the phase calculation and phase unwrapping; and (3) 3D reconstruction, which calculates the 3D coordinates for all camera pixels from the absolute phase distributions through a phase-to-3D-coodinate mapping process based on the relationship determined in the calibration. Steps (1) and (2) are referred to as phase measurement in this research.

1.1.2 Phase Measurement in Phase-Shifting Profilometry

In PSP, multiple phase-shifted sinusoidal intensity-profile fringe patterns (Figure 1-4) are typically projected sequentially onto an object surface. The fringe patterns appear distorted in the camera view according to the surface geometry. For a camera pixel with a 2D image coordinate of (x, y), the captured intensities of the deformed fringe patterns can be represented as:

$$I_i(x,y) = a(x,y) + b(x,y)\cos\left[\Phi(x,y) + \delta_i\right], i = 1,2,...N, \quad (1.1)$$

where $a(x,y)$ denotes the background intensity, $b(x,y)$ represents the intensity modulation, $\Phi(x,y)$ is the phase value to be determined, and δ_i are the phase-shifts, which can be expressed as $\delta_i = 2\pi i / N, i = 1,...,N$. N is the number of phase-shifts. The phase value can then be calculated by:

$$\Phi(x,y) = -\tan^{-1}\left(\frac{\sum_{i=1}^{N} I_i(x,y)\sin\delta_i}{\sum_{i=1}^{N} I_i(x,y)\cos\delta_i}\right), i = 1,2,...,N, \quad (1.2)$$

yielding a phase distribution or phase map, $\Phi(x,y), 0 \le x \le m-1, 0 \le y \le n-1$, where $m \times n$ is the size of the camera image. There are three unknowns $a(x,y)$, $b(x,y)$ and $\Phi(x,y)$ in Equation 1.1. Therefore, at least three images I_1, I_2, I_3 ($N=3$) should be used to provide three equations (Equation 1.1) and enable calculation of $\Phi(x,y)$, and three sinusoidal intensity-profile phase-shifted fringe patterns are required (Figure 1-4). The preferred phase shift between the two fringe patterns is $2\pi/3$ for highest accuracy [13].

A phase-unwrapping process is required to eliminate fringe ambiguity and acquire an absolute phase map or distribution. The main task of phase-unwrapping is to add multiples of 2π corresponding to the proper fringe order in a phase distribution that was obtained in wrapped form (values limited to the range $[-\pi, \pi]$), due to the computation of the inverse tangent function in Equation 1.2.

The absolute phase distribution is modulated by the surface geometry of the measured object and therefore contains information of the object surface height (or depth). Thus, the obtained absolute phase distribution can be used to calculate the 3D coordinates for every camera pixel through the phase-to-3D-coordinate mapping process with known system calibration parameters.

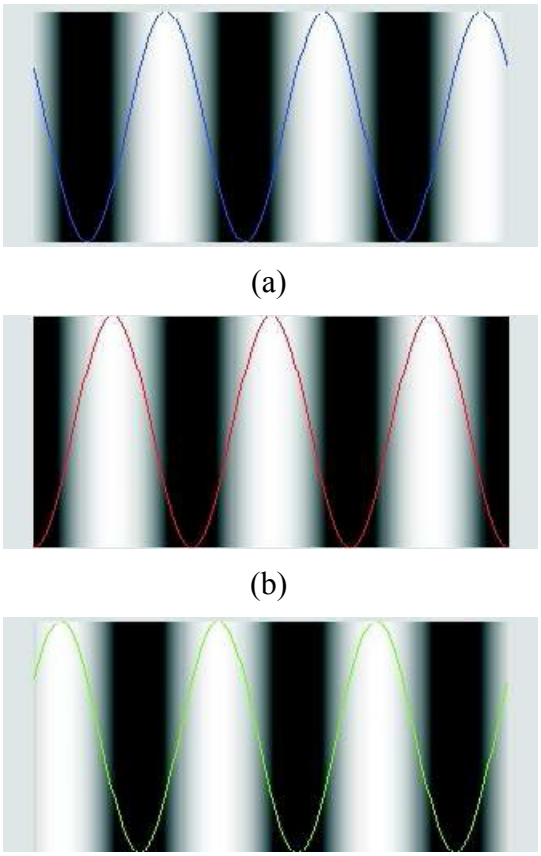

Figure 1-4 Three sinusoidal intensity-profile fringe patterns with $2\pi/3$ phase shift: (a) Fringe pattern 1; (b) Fringe pattern 2; (c) Fringe pattern 3. (The blue, red, and green overlaid sinusoidal curves of intensity versus *x* pixel do not exist in the real projection. They are only used in this figure to help illustrate the sinusoidal intensity profile of the fringe patterns and the phase shift along the horizontal (*x*) axis).

It is worth noting that phase measurement is also performed in system calibration to generate the absolute phase distributions of a calibration-object surface. The obtained absolute phase distributions will then be used to construct the camera-projector pixel correspondence. Phase measurement accuracy is therefore crucial to both system calibration and 3D shape measurement.

1.1.3 Problems in Phase-Shifting Profilometry

There exist problems in the phase measurement for phase-shifting profilometry that will lead to significant phase errors and associated system calibration and 3D shape measurement errors.

1) In the first step of phase measurement, the generation, projection and image capture of the fringe pattern, the captured intensity values (Equation 1.1) for phase calculation by Equation 1.2 can be affected by image saturation, which occurs when a captured intensity exceeds the upper limit of the dynamic range of the camera. The pixel intensity can only be captured as the maximum gray-level of the camera and the true intensity is thus not captured; there is loss of information. This has the effect of capturing an incorrect intensity pattern in some portion of the captured image. Pixel saturation can be caused by many factors such as improper setting of the aperture and exposure time of the camera, highly reflective (shiny) surfaces, and bright ambient light. Varying surface reflectivity over a surface is particularly difficult to handle. A review of previous image saturation avoidance methods is given in Section 2.3.

2) In the second step of phase measurement, previous phase-unwrapping methods still have problems in accurate and unambiguous computation of an unwrapped phase distribution especially for surfaces with geometric discontinuities. Previous phase-unwrapping methods that have been used in system calibration also suffer from various limitations. A review of previous phase-unwrapping methods and system calibration methods is given in Sections 2.1 and 2.2, respectively.

1.2 Research Motivation

1.2.1 Need for Compact 3D Scanners

In industrial metrology, compact 3D scanners are required for measuring interior surfaces, such as the inner profiles of pipes, tubes, vessels, and compartments. The 3D scanners have to be compact enough to firstly go into the inside of the confined space and then perform the measurements. For in-line part inspection in a manufacturing environment, the 3D scanners

should be compact to fit in the limited working space and avoid interfering with other processes.

There is also an increasing need for common people to get access to 3D data for a wide range of personal uses. For example, players of video games may prefer to use the digital 3D models of their faces and body parts as their avatars. This not only makes the avatars look realistic and more appealing to the players, but also enhances the interaction and mutual trust among players in the virtual gaming environment. Players may also prefer to use the 3D models of their living environment as a virtual gaming environment for better gaming experience. In everyday lives, people may prefer to share the 3D models of handcrafts, cars, furniture, tabletop items, small sculptures, store goods, or other items with their remote relatives or friends. The 3D models can be rotated and viewed from any angle of view, and therefore look more real than the 3D images produced by the current stereo 3D cameras. Existing 3D cameras use the stereoscopic technique [14] to only give consumers the impression of 3D but do not provide a real 3D model of object surfaces. Furthermore, 3D models may also enable people to duplicate an item, using low-cost home 3D printers, to replace a missing part not available for purchase. All of the above applications could benefit from a compact 3D scanner that consumers can easily carry along and set up for 3D shape measurement.

1.2.2 Relation of Measurement Accuracy to Compactness

In a camera-projector measurement system, the relation between system geometry (camera-projector angle and baseline) and measurement accuracy may not be the same as in a stereo-camera-pair system: better measurement accuracy at larger camera-projector angle. In fringe-projection techniques, factors such as image noise, image saturation, varying surface reflectivity, complex surface geometry, angles between surface orientation and projector illuminating angle and camera viewing angle, angle between light projection and camera view directions, and depths of field of the camera and projector in addition to the system geometry, will all affect the intensity modulation of captured fringe patterns and the associated phase measurement and 3D shape measurement accuracy. All these factors are

related, making analysis of the effect of system geometry on measurement accuracy difficult to predict mathematically. It is thus necessary to determine experimentally how measurement accuracy of a fringe-projection 3D scanner varies with system geometry, in order to determine the most compact design that satisfies a desired measurement accuracy.

All methods that contribute to improving the measurement accuracy will contribute to enabling a more compact design to achieve a desired measurement accuracy. Any method that improves measurement accuracy will offset any loss of accuracy associated with a more compact design.

1.3 Research Objectives

The main objectives of this research are to analyze and gain a better understanding of the effect of various parameters on measurement accuracy and compactness of a 3D scanner, and to develop methods that aim at better solving: (1) the inaccurate phase-unwrapping problem that limits the phase measurement accuracy in both system calibration and 3D shape measurement, and (2) the image saturation problem. The expected outcome of the research work is to achieve improved compactness of a 3D scanner, while maintaining a desired measurement accuracy, in order to better meet the needs for a compact 3D scanner in practical applications. Specific objectives are to:

- Develop measures in measurement accuracy assessment for a 3D scanner; the measures would be used to representatively report the 3D scanner's performance in measuring different surface shapes;
- Develop an improved phase-unwrapping method that would achieve unambiguous phase-unwrapping at geometric discontinuities and compensation for spike-like errors; the method would not only preserve more measured points, but also guarantee a more accurate projector-camera system calibration robust to image noise;
- Develop new adaptive fringe-pattern projection methods to avoid camera image saturation; the methods would permit camera-independent measurements under non-uniform object-surface reflectivity;

- Analyze the effect of camera-projector system geometry (relative camera-projector position and angle) on 3D shape measurement accuracy. The relative camera-projector position and angle determine the compactness of a camera-projector measurement system. Knowledge of the relation between camera-projector system geometry (and thus system compactness) and measurement accuracy would enable better selection of geometric parameters to employ when designing a compact 3D scanner to have a specified measurement accuracy.

1.4 Thesis Organization

The reminder of the thesis is organized as follows. Chapter 2 reviews existing phase unwrapping, system calibration, and image saturation avoidance methods in fringe-projection 3D shape measurement. Existing compact 3D scanners are also reviewed.

Chapter 3 presents the formulation of several statistical measures used in accuracy assessment for 3D scanners.

Chapter 4 presents a new improved heterodyne phase-unwrapping method to compensate for the spike-like errors that may lead to system calibration failure. Simulations and real-system experiments were performed to compare phase unwrapping and system calibration without and with the method. Real-system experiments were performed to verify the method in measuring a flat plate and a spherical ball translated to different depths, and a free-form mask.

Chapter 5 presents a new adaptive fringe-pattern projection (AFPP) method for image saturation avoidance in 3D shape measurement. Real-system experiments were performed to compare measurements of a planar board and a free-form mask with no AFPP, simplified AFPP, and AFPP, respectively.

Chapter 6 presents a new pixel-wise adaptive fringe-pattern projection (PWAFPP) method for image saturation avoidance in 3D shape measurement. Real-system experiments were performed to evaluate the AFPP and PWAFPP methods by measurement of two objects with a large range in surface reflectivity.

Chapter 7 presents analyses of the relation between camera-projector system geometry, and thus system compactness, and 3D shape measurement accuracy. Real-system experiments were performed on a flat plate translated to different depths, and a double-sphere object to compare measurements with different system geometry. These analyses were performed for two scanners, one for industrial use and one for consumer use.

Chapter 8 summarizes contributions and future work.

Chapter 2
Literature Review

In this chapter, previous methods for solving problems in phase-shifting profilometry (PSP), identified in Section 1.1.3, and existing compact 3D scanners that implement PSP are reviewed.

2.1 Phase Unwrapping

The main task of phase-unwrapping is to add multiples of 2π corresponding to the proper fringe order in a phase map that was obtained in wrapped form (values limited to the range $[-\pi, \pi]$). As an example, Figure 2 shows the generation of an absolute phase map (Figure 2-1f) from a wrapped phase map (Figure 2-1e) obtained from four images (Figure 2-1a to 2-1d) of four vertical phase-shifted sinusoidal fringe patterns with phase shifts $0, \pi/2, \pi, 2\pi/3$, respectively. An algorithm that detects a phase change of more than π between two adjacent pixels is used to accomplish the task. When vertical fringe patterns are used, the wrapped phase difference between two adjacent pixels at the same row is

$$\Delta\varphi_W(x, y) = \varphi_W(x_i, y) - \varphi_W(x_{i-1}, y), \tag{2.1}$$

If $|\Delta\varphi_W(x, y)| > \pi$, the unwrapped phase $\varphi_U(x, y)$ can be calculated by

$$\varphi_U(x, y) = \begin{cases} \varphi_W(x_i, y) - 2\pi, & \Delta\varphi_W(x, y) > \pi \\ \varphi_W(x_i, y) + 2\pi, & \Delta\varphi_W(x, y) < -\pi \end{cases}. \tag{2.2}$$

Equations 2.1 and 2.2 will be performed for every row to obtain the unwrapped (absolute) phase map, as shown in Figure 2-1f.

Full-field phase-unwrapping results by following different paths may vary and an incorrect wrapped phase value of a pixel would result in accumulated phase-unwrapping errors at subsequent pixels. Spatial phase-unwrapping methods aim to avoid this problem. Details on problems in phase-unwrapping and spatial phase-unwrapping methods can be found in a

review by Judge and Bryanston-Cross [15], and in a comparison study of eight spatial phase-unwrapping methods by Zappa and Busca [16].

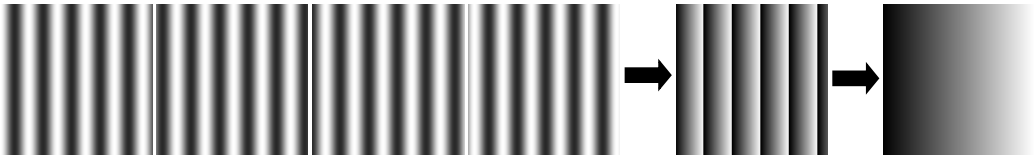

(a) (b) (c) (d) (e) (f)

Figure 2-1 Generation of an absolute phase map: (a-d) four images of four vertical phase-shifted sinusoidal fringe patterns with phase shifts $0, \pi/2, \pi, 3\pi/2$, respectively, (e) vertical wrapped phase map computed from (a-d), (f) vertical absolute phase map computed from (e).

Although spatial methods have worked well to measure smooth surfaces, they suffer from two main problems: first, the spatial methods used in system calibration require projection of a single line pattern as an absolute-phase reference line [17], and the line detection may contribute to calibration error; second, the spatial methods cannot handle geometric discontinuities, such as sharp edges and surfaces of multiple objects, which lead to fringe order ambiguity. Several methods have been proposed to solve these two problems:

(1) Gray-Code and Phase Shifting

The Gray-code approach [18] projects a sequence of black-and-white stripe patterns $P_0, P_1, ..., P_{t-1}$ at times $t = 0, 1, ..., n-1$. Each pattern is formed in such a way that the projection of $P_0, P_1, ..., P_{t-1}$ corresponds to the formation of a Graycode of n bits and each fringe of a sinusoidal pattern can be assigned a unique Gray-code word. The number of the Gray-code words 2^n should be no less than the fringe number of the sinusoidal patterns, in order to assign a unique order to each fringe. The main drawback of this method is that a large number of the back-and-white stripe patterns is required.

(2) Temporal Phase Unwrapping

Huntley and Saldner [19] firstly proposed a temporal phase-unwrapping method that is based on 1-D unwrapping along the time axis rather than on a 2-D spatial unwrapping, where the phase at each pixel is measured as a function of time and unwrapped independently from other pixels. Several sets of phase-shifted fringe-patterns using different spatial frequencies

are used. The method offers two advantages. First, it relaxes the constraint of path-dependence in the spatial phase-unwrapping methods and thus removes the influence of pixels with poor wrapped phase accuracy on other pixels. Second, it enables correct phase-unwrapping at geometric discontinuities.

The main drawback of the temporal phase-unwrapping method is that because it unwraps over time, a large number of fringe patterns are required. Fast measurement is therefore difficult to achieve. Huntley and Saldner [20] proposed a new method in which the spatial frequency is changed exponentially with time in order to use fewer fringe-pattern sets. They also proposed a method [21] to improve the signal-to-noise ratio (SNR) of the total phase change by incorporating data from the intermediate phase values. The number of projected frequencies is dependent on the required unwrapped phase range and the noise level in the wrapped phase distribution. Towers et al. [22] proposed an optimization criterion to utilize the minimum number of projected fringe frequencies to give the largest possible unwrapped phase range at a certain noise level. The criterion can be used to determine when the two-frequency [23] and three-frequency [24] methods can be used. The heterodyne method [25] extends the unwrapped phase range to the beat frequency of two close frequencies. The method allows the use of high frequency patterns only, which leads to lower random errors in the phase values, compared with low-frequency patterns used in all the other temporal phase-unwrapping methods.

Because of the above advantages, the heterodyne method was used in this research in both system calibration and 3D shape measurement. However, this original method still needs to be improved because of the spike-like errors it suffers, detailed in Section 4.1.2. The spike-like errors result in outliers in 3D shape measurement, which require post-processing for their removal, and therefore reduction in the number of measured points. Furthermore, the spike-like errors result in camera-projector stereovision system calibration failure, detailed in Section 4.2.1. In this thesis, an improved heterodyne phase-unwrapping method that compensates for the spike-like errors and thus increases accuracy over the original method is detailed in Section 4.3.

2.2 System Calibration

System calibration is a process of determining the parameters that relate the phase distribution to the 3D coordinates of points on an object surface. Previous system calibration methods can be categorized into three groups: least-squares phase-to-height mapping, known-parameter optimization, and the projector-camera stereovision method used in this thesis.

(1) Least-Squares Phase-to-Height Mapping

Least-squares phase-to-height mapping methods [26-31] determine the coefficients of the function that best fit the phase-to-height mapping. One drawback of these methods is the need for precision in the optical geometry of the setup. For example, the line between the projector and camera optical centres should ideally be parallel with the reference plane. However, this is difficult to achieve in practice. Modified least-squares phase-to-height mapping methods [32-33] relax the constraint by permitting arbitrary experimental setup. However, these methods still require a physical reference plane which needs to be translated to several known positions either by a precision translation stage or using precision gauge blocks of different heights or precisely positioned. This requirement impedes the application of fringe projection profilometry systems outside laboratory environments, unless the system is pre-calibrated. Traditional least-squares phase-to-height mapping methods [26-31] also suffer from the assumption that the fringe spacing in the captured image of the reference plane is uniform. However, the diverging rays of the projector and the angle between the projector and camera optical axes make uniform spacing difficult to achieve. While it is still possible to use least-squares phase-to-height-mapping methods, the assumption of uniform fringe-pattern spacing contributes to measurement error. Non-parallel projection and carrier-removal techniques [31, 34] have been proposed to solve this problem.

(2) Known-Parameter Optimization

Known-parameter optimization methods [35-38] measure calibration parameters directly. The approximately measured parameters are then optimized through iteration by measuring gauge objects with known geometric features. However, the procedures are time-consuming

and complicated. Improper initial measured parameter values may also make the subsequent iterations take considerable time for the method to converge or even fail to converge.

(3) Camera-Projector Stereovision

Camera-projector stereovision methods [17, 39-41] treat the projector as an inverse camera, and offer the advantage that the calibration can be performed using a calibration board (a checkerboard is commonly used) positioned somewhat arbitrarily at several positions without the precise position and orientation having to be known. System calibration then becomes similar to stereo-camera calibration. The essential and most difficult step of stereovision-system calibration is determining the corresponding pixels between images captured from two or more viewpoints at the same time (in the overlapping observable area of the cameras). Unlike cameras, a projector can only project images. Thus, one key procedure in camera-projector system calibration methods is utilizing two orthogonal phase distributions of the same calibration board at different positions and orientations to determine the correspondence between projector and camera pixels (further detailed in Chapter 4). Therefore, virtual images at different calibration board positions and orientations can be constructed for the projector, and the projector can then be calibrated using well-developed camera calibration methods [42-43].

In summary, camera-projector stereovision methods avoid not only the complicated and time-consuming procedures in known-parameter optimization methods but also the requirement of a physical reference plane in least-squares phase-to-height mapping methods. Fundamentals of the camera-projector stereovision methods will be detailed in Section 4.2.1. As mentioned in Section 2.1, the heterodyne phase-unwrapping method used in system calibration easily introduces spike-like errors in the computed absolute phase distributions. If spike-like errors happen to occur at camera pixels of control points (corners of the checkerboard squares), positions of the control points in the projector image cannot be correctly determined. The projector calibration will fail, and no measurement can be done because no calibration parameter is available. This problem can be overcome by the newly developed heterodyne phase-unwrapping method that can detect and compensate for the

spike-like errors in the absolute phase maps and thus ensure usable projector calibration, as detailed in Section 4.3.

2.3 Image Saturation Avoidance

There are several types of light reflection that affect pixel saturation and ultimately have an effect on PSP. Diffuse reflection is the reflection of light from a surface such that an incident ray is reflected at many angles. An illuminated ideal diffuse reflecting surface will have equal luminance from all directions in the hemisphere surrounding the surface. Specular reflection is the mirror-like reflection of light from a surface. Light from a single incoming direction is reflected into a single outgoing direction. For both human eyes and cameras, the visibility of objects is primarily caused by diffuse reflection of light. For shiny surfaces, the reflected light involves both diffuse and specular reflection components; the latter accounts for the major percentage of the light power. If the detected reflected light power is beyond the upper limit of the dynamic range of the camera, the camera pixels that detect the reflected light will be saturated. The captured intensity will be truncated to the maximum gray-level of the camera. The phase-shifting algorithm will be affected if one or more captured intensities of the phase-shifted fringe patterns are distorted by truncation. Traditional methods of 3D surface measurement often include surface treatments, such as coating or spraying powders or other materials over the shiny surfaces, to eliminate the specular reflected light. However, it has been long desired that 3D scanners be able to measure shiny surfaces without pre-treatments, because the thickness of the coat might be near the desired level of measurement accuracy, and the measurement accuracy of the original surfaces will be affected. Furthermore, coating or modifying a surface is often undesirable, for example in measuring archaeological artifacts. Other saturation avoidance methods can be divided into four groups.

(1) Multiple Camera Views and Projection Directions

Image saturation caused by specular light reflection has been handled using multiple camera viewpoints [44] and projection directions [45] to ensure that at least one projector-lighting and camera-viewing angle combination permits measurement without saturation in previously saturated image regions. These approaches have worked well because specular

light reflection is highly dependent on lighting and viewing angles, although greater complexity in system hardware, data acquisition, and data processing have been necessary. Richard *et al.* [46] proposed a method that measures a shiny object at different viewing angles by repositioning the 3D scanner. At each viewing angle, the saturation problem occurs at different parts of the object surface. Complete three-dimensional (3D) point cloud data of the object surface can be acquired by registration (aligning and merging) of several measurement data sets obtained from the different viewing angles that avoid specular reflection. The main drawback of this method is that it requires a large number of measurements to handle a shiny object with complex surface geometry. This method also involves the complicated and time-consuming registration of multiple surface data sets.

(2) Polarimetric Imaging

A polarimetric imaging method [47] prevents the specular reflected light from entering the camera by utilizing a polarizer to separate the diffuse and specular components of the reflected light according to their different polarization characteristics. This method suffers from two main problems. First, using a polarizer, the removal of specular reflection is related to the direction of the specular reflected light. For a shiny object with complex surface geometry, it is impossible to remove all the specular reflected light by simply adjusting the orientation of the polarizer or the object. Second, the output power of the reflected light using a polarizer would be reduced, and so would the signal-to-noise ratio (SNR). When the SNR is low, the fringe intensities are less distinguishable and the noise causes the captured intensities to have error. These problems can be partly overcome by a multi-polarization imaging technique [48] using a multi-polarization camera that captures four images at four different polarization states. A composite image is generated pixel-by-pixel by finding an intensity that gives the best fringe quality from the four images. One drawback of the method is the reduced spatial resolution needed to capture four polarization states.

(3) Increased Phase Shifts

Chen *et al.* [49] proposed a phase-shifting algorithm that can calculate the phase when partial intensity saturation occurs (when one or more captured intensities in multiple images of

different projected fringe patterns at the same pixel are beyond the maximum gray-level of the camera). The technique involves capturing more than three images in order to obtain at least three unsaturated intensities at each pixel. However, an increased number of phase-shifted patterns would be needed to handle a higher number of saturated intensity signals at the same pixel.

(4) High-Dynamic-Range (HDR) Imaging

Saturation problems occurring from shiny object surfaces can be avoided by lowering the aperture or exposure-time of the camera to limit the reflected light that enters the camera. Because the power of the specular reflected light is much greater than that of the diffuse reflected light, a specific setting of aperture or exposure time of the camera cannot realize maximal signal-to-noise (SNR) over the whole camera field of view. Thus, accurate measurement of surfaces with a large range in reflectivity can be difficult using a single aperture setting or global exposure time. Zhang and Yau [50] proposed a method that repeatedly captures a reflected fringe pattern from a shiny object surface at different exposure times. A composite fringe pattern image was then constructed pixel-by-pixel from the obtained sequence of fringe-pattern images by choosing the brightest but unsaturated intensities from the images. Thus, a maximal SNR can be achieved over the whole camera field of view. However, a large number of exposures were used. Zhang and Yau [50] used 23 exposures to obtain good quality. Jiang *et al.* [51] improved this method by projecting white and red light separately to increase the brightness of the diffuse reflected light and decrease the brightness of the specular reflected light, respectively. Based on an analysis of measurement sensitivity to illuminance and fringe-pattern gray-levels [52], Waddington and Kofman [53] proposed a method that gradually decreases the maximum intensity gray-level (MIGL) of computer-generated fringe patterns using a fixed gray-level step size for all iterations, and then combines the brightest unsaturated pixels in a composite image before computation of phase. A limitation of the method is that either many iterations are used when the gray-level step size is small, or if few iterations are used, the gray-level step size will be large, and the decreased intensity modulation at each pixel may be beyond what is necessary to avoid saturation, resulting in an overly low accuracy of the calculated phase distribution.

Waddington [54] proposed a dynamic pixel-wise adaptive (DPA) method to improve the measurement efficiency. At each iteration, the gray-level step size was adapted by thresholding the estimated percentage of pixels that would be saturated at each MIGL reduction step, using a cumulative distribution function (CDF) of the estimated intensities that would occur without camera sensor saturation. Again, the intensity modulation at each pixel may not be ideal, resulting in an overly low accuracy.

Although all of the HDR 3D imaging methods above have handled a surface with a large range in reflectivity, one major common drawback is that a global setting of exposure time or MIGL across the entire fringe pattern or image were used during the acquisition of 2-D images, and only in a post-process the composite images (with different exposure time or MIGL across pixels) were computed. This was coupled with the problem of a large number of sets of fringe patterns projected and images captured (where all images within a set are acquired at the same MIGL or exposure time). (In this thesis, a "set" thus refers to all fringe patterns at multiple phase shifts, fringe frequencies, and fringe directions that are used in the shape measurement, depending on the specific phase-measurement based technique). The drawback of previous HDR techniques was therefore the large number of sets of fringe patterns used with global projector and camera settings that are uniform across the entire pattern or image during fringe pattern projection and image acquisition, respectively.

As an alternative to the use of a single global exposure-time setting across the entire image optical techniques have been used to control the camera exposure time at individual pixels, for example, using a controllable optical attenuator [55]; however, the final exposure setting at saturated pixels was also determined from multiple iterations to generate the final composite images, and additional optical and control hardware were required.

An advantage of changing the projected MIGL instead of the camera exposure time is that the MIGL adjustment can be performed locally on a pixel-to-pixel basis at the initial fringe-pattern projection stage of FPP without additional hardware. In this thesis, two new adaptive fringe-pattern projection (AFPP) methods that modify the MIGL locally in the projected fringe patterns based on the saturated pixels in the captured images of the surface being

measured are presented in Chapter 5 and Chapter 6. The first method locally modifies the projected intensities by individual saturated regions (presented in Chapter 5), and the second method further improves on this by modifying the MIGL in the projected fringe patterns pixel-by-pixel based on the saturated pixels in the captured images of the surface being measured (presented in Chapter 6).

2.4 Compact 3D Scanners using Phase-Shifting Profilometry

With an interest to make 3D measurement systems more compact, fringe-projection 3D scanners [56-57] have been miniaturized by positioning the projector and camera together with a small angle and distance between them; however, it is unclear what the real measurement accuracy was. Although some other existing compact 3D scanners [58-60] are much smaller compared with the ones in [56-57], they are used for performing measurement in extremely space-restricted environments only, with small measurement areas 25 mm × 15 mm in [58], 10 mm × 8 mm in [59] and 3 mm × 3 mm in [60], respectively. Such small measurement areas do not enable measurement of common tabletop items or human faces in a single measurement, as desired in this research.

The compactness of a 3D scanner using digital fringe projection partly depends on the physical size of the employed pattern projection and image capture systems. While a variety of small cameras exist with different capabilities, the size of projectors remains the dominating limiting size factor, since only recently has there been an attempt to reduce projector size. Huang *et al*. [61] and Lohry *et al*. [62] used pico (pocket) projectors (small off-the-shelf video projectors compared with more commonly-used large off-the-shelf video or data projectors) in their compact 3D scanners. However, no details about the measurement accuracy were provided in [61-62]. Yoshizawa *et al*. [63] explored using a micro-electro-mechanical (MEMS) scanner as the projection unit in their compact measurement system. The MEMS scanner offers the advantage of a large scanning field of view, high-speed scanning, low-noise and a light-weight system. It also does not suffer from the projector nonlinearity of video projectors. However, phase-shifted sinusoidal intensity-profile fringe patterns were not generated and phase-shifting profilometry was not performed. Wakayama

and Yoshizawa [64] also used a MEMS scanner in their compact 3D scanner. It is unclear what the real measurement error was since they reported a "variation of about 0.3 mm" and it is unclear if negative and positive errors were averaged.

The design of a compact 3D scanner is complicated by the various object-system geometry and measurement-setup factors that affect measurement accuracy. Based on knowledge of camera-stereovision systems, a small camera-projector angle (small triangulation angle or baseline between camera and projector) would tend to lower depth measurement sensitivity. Based on this factor alone, there is a need to better understand the tradeoff in loss of accuracy with more compact design, in other words, to fully understand what 3D scanner compactness can be achieved for a specified desired accuracy. Furthermore, as mentioned in Section 1.2.2, other factors, such as surface geometry, angles between surface orientation and projector illuminating angle and camera viewing angle, distance between camera and projector to the object, in addition to the angle between light projection and camera view directions, influence measurement accuracy. As the level of intensity noise related to these multiple factors may be difficult to reliably model, in order to understand whether a certain configuration of compact 3D scanner can achieve a desired accuracy, or whether there is still room to improve the compactness of the 3D scanner to achieve the desired accuracy, it is necessary, as explained in Section 1.2.2, to assess the measurement accuracy of the 3D scanner with different camera-projector geometry, such as angle (and thus distances) between the camera and projector and working (standoff) distance between the camera-projector and object). There is only one research work [65] related to this issue. In one of the simulation and real-system experiments, only a single point was measured at different camera-projector angles and only the precision (repeatability) was reported. The dependency of the 3D measurement accuracy on camera-projector angle is therefore still unknown. Additionally, single-point measurement is insufficient in reflecting the distribution of measurement errors across the fields of view of the camera and projector at multiple camera-projector angles, because the distribution is also dependent on the camera-projector angle.

In this research, object-system geometry and measurement-setup factors that influence the relationship of system measurement accuracy to system compactness were studied using a

system built from off-the-shelf camera and projector components. A pico projector was used due to its small physical size and low cost. The experimental approach and analysis are presented in Chapter 7 to determine the relationship of system compactness to measurement accuracy.

Chapter 3

Measurement Accuracy Assessment for 3D Scanners

In this chapter, error measures are defined for measurement of three different types of objects with known surface geometry. The measures will be used in the following chapters for accuracy assessment, aiming at testing multiple techniques that have been developed to reach the research objectives specified in Section 1.3.

3.1 Flat Plate Measurement

A flat plate, mounted on a micrometer translation stage, is moved to different known positions toward the camera-projector from a reference position, and the plate is measured at each position. At each position, a plane is fitted to the measured points using the least-squares method. A plane fitting error is the distance between a measured point and the fitted plane at each position. (1) The standard deviation (SD) of the plane fitting errors is computed as one error measure. The fitted plane to measured points at a position near the centre of the measurement volume is selected as a reference plane, where the camera and projector are in best focus. (2) The root-mean-square error is computed at each plate position by

$$\mathrm{RMSE} = \sqrt{\frac{\sum_{i=1}^{n}\left(d_i - D\right)^2}{n}}, \tag{3.1}$$

where d_i represents the perpendicular distance between a measured point and the reference plane, D is the true distance, and n is the total number of points.

3.2 Spherical Ball Measurement

A spherical ball, mounted on the same micrometer translation stage, is measured at different known positions with the same reference position. At each position, a sphere is fitted to the measured points and the following computations are made: (1) the standard deviation (SD) of the sphere fitting errors, (2) the mean absolute radius error

$$e_r = \frac{1}{n}\sum_{i=1}^{n}\left|r_i - R\right|, \tag{3.2}$$

where r_i is the distance between a measured surface point and the centre of the fitted sphere, R is the true radius, n is the total number of points, and subscript r refers to radius, and (3) the absolute centre-to-centre distance error

$$e_c = \left| d_c - D \right|, \tag{3.3}$$

where d_c is the distance between the centre of a fitted sphere at each position and the centre of the fitted sphere at the reference position, D is the true distance, and subscript c refers to sphere centre.

3.3 Double Spheres Measurement

A double-sphere object with known radii of the two spheres and distance between the centres of the two spheres is measured at the reference position. Two spheres are fitted to the measured points and the following computations are made for the two spheres: (1) the standard deviation (SD) of the sphere fitting errors, (2) the mean absolute radius error

$$e_r = \frac{1}{n} \sum_{i=1}^{n} \left| r_i - R \right|, \tag{3.4}$$

where r_i is the distance between a measured surface point and the centre of the fitted sphere, R is the true radius, n is the total number of points, and subscript r refers to radius, and (3) the absolute centre-to-centre distance error

$$e_c = \left| d_c - D \right|, \tag{3.5}$$

where d_c is the computed distance between the centres of the two fitted spheres, D is the true distance and subscript c refers to sphere centre.

3.4 Summary

While much effort have been put in method development in fringe-projection 3D shape measurement, accuracy assessment for 3D scanners has not adequately progressed. As has been reviewed in Section 2.4, unclear information about the measurement accuracy is

sometimes reported. The measures defined in this chapter provide the following preferable features:

- computation of every measure involves a large number of measured points, thus enabling reliable statistical analysis;
- The influence of depth on measurement precision and accuracy can be studied by measuring the flat plate and spherical ball at multiple positions on the translate stage;
- At each position, because each object covers large fields of view of the camera and projector, the measures can thus reflect how the measurement error distributes across the fields of view of the camera and projector.

Chapter 4
Camera-Projector Stereovision System Calibration

In a camera-projector stereovision system for 3D shape measurement (Figure 4-1), a point $P(\mathrm{X_W}, \mathrm{Y_W}, \mathrm{Z_W})$ on an object surface projects to the camera image plane at $M_\mathrm{P}(x_\mathrm{p}, y_\mathrm{p})$ $p_\mathrm{c}(u_\mathrm{c}, v_\mathrm{c})$ and projector image plane at $p_\mathrm{p}(u_\mathrm{p}, v_\mathrm{p})$. The purpose of camera-projector system calibration is to find the mapping of the camera and projector image coordinates to the world coordinates for 3D shape measurement. Camera-projector calibration is performed as for a two-camera system except that the projector is treated as an inverse camera [17], and virtual projector images of a calibration object are constructed based on the correspondence between camera pixels and projector pixels. This correspondence is determined from two orthogonal absolute phase maps computed from vertical and horizontal phase-shifted sinusoidal fringe patterns (Figure 4-2), as explained in the following sections. In this chapter, a new error-compensation heterodyne phase-unwrapping method is presented. The newly developed method prevent spikes in the absolute phase maps that may occur when the original heterodyne phase unwrapping method is used. These spikes may lead to large camera-projector stereovision-system calibration error if not compensated for.

4.1 Phase Measurement

4.1.1 Absolute Phase-Map Generation

In fringe-projection phase-shifting for surface-shape measurement, a phase map is generated by projecting a set of phase-shifted sinusoidal intensity-profile fringe patterns onto an object surface, and capturing images of the patterns with intensity distributions described by:

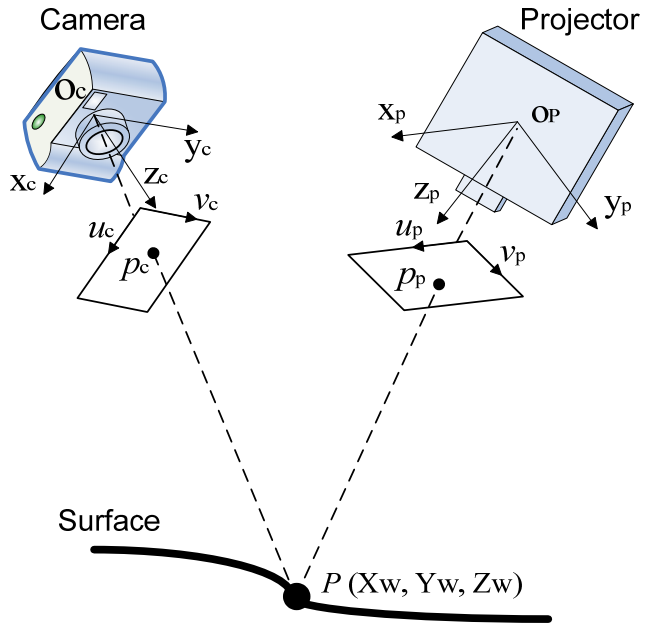

Figure 4-1 Configuration of a camera-projector setup for 3-D shape measurement.

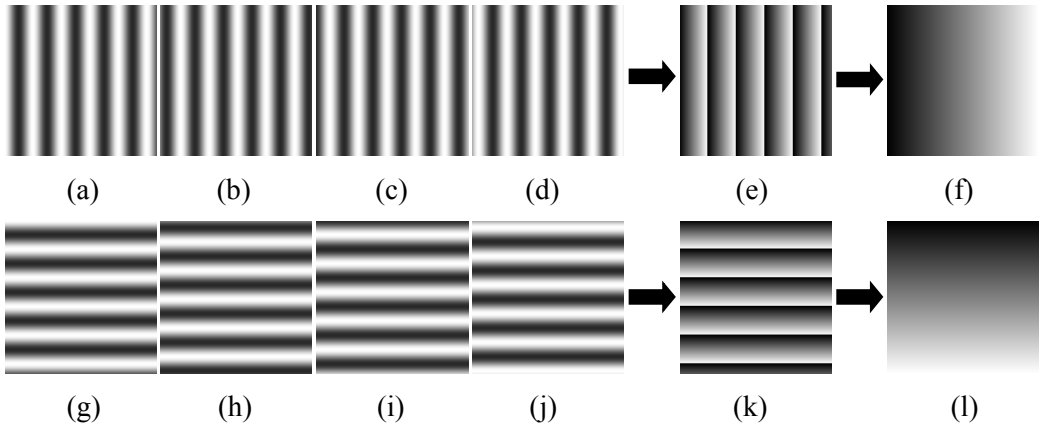

Figure 4-2 Generation of two orthogonal absolute phase maps: (a-d) four vertical phase-shifted sinusoidal fringe patterns with phase shifts $0, \pi/2, \pi, 3\pi/2$, respectively, (e) vertical wrapped phase map computed from (a-d), (f) vertical absolute phase map computed from (e); (g-j) four horizontal phase-shifted sinusoidal fringe patterns with phase shifts $0, \pi/2, \pi, 3\pi/2$, respectively, (k) horizontal wrapped phase map computed from (g-j), (l) horizontal absolute phase map computed from (k).

$$I_i(x,y) = a(x,y) + b(x,y)\cos\left[\Phi(x,y) + \delta_i\right], i = 1,2,...N, \tag{4.1}$$

where (x, y) are the images coordinates, $a(x, y)$ denotes the background intensity, $b(x, y)$ represents the intensity modulation, $\Phi(x, y)$ is the phase map, and $\delta_i = 2\pi i / N$ are the phase-shifts between images. At least three phase-shifted fringe patterns are required to solve for the three unknowns, $a(x, y)$, $b(x, y)$ and $\Phi(x, y)$. The phase map can then be computed by

$$\Phi(x, y) = -\tan^{-1}\left(\frac{\sum_{i=1}^{N} I_i(x, y)\sin\delta_i}{\sum_{i=1}^{N} I_i(x, y)\cos\delta_i}\right), i = 1, 2, ..., N \ . \tag{4.2}$$

Due to the inverse tangent operator, Equation 4.2 calculates a wrapped phase map $\Phi(x, y)$, as shown in Figure 4-3e and Figure 4-3k. Phase unwrapping is a process whereby multiples of 2π are added to the wrapped phase map $\Phi(x, y)$ according to fringe order, to remove the 2π periodicity and thus eliminate fringe ambiguity in the wrapped phase map, resulting in an absolute phase map $\varphi(x, y)$, as shown in Figure 4-3f and Figure 4-3l.

4.1.2 Spike-Like Errors in Heterodyne Phase Unwrapping

The heterodyne phase-unwrapping method [41] has been used to extend the unwrapped phase range to the beat frequency of two close frequencies. Assuming the two frequencies of the two sets of fringe patterns are $f_1, f_2 (f_1 > f_2)$, the two wrapped phase values $\varphi_{W1}(x, y)$, $\varphi_{W2}(x, y)$ can be initially computed through Equation 4.2. The beat frequency f_{12} can be computed by Equation 4.3

$$f_{12} = f_1 - f_2 \ . \tag{4.3}$$

The phase value $\varphi_{W12}(x, y)$ that corresponds to the beat frequencies f_{12} can then be computed from the initial two wrapped phase values by Equation 4.4

$$\varphi_{W12}(x, y) = \begin{cases} \varphi_{W1}(x, y) - \varphi_{W2}(x, y), & \varphi_{W1}(x, y) > \varphi_{W2}(x, y) \\ 2\pi + \varphi_{W1}(x, y) - \varphi_{W2}(x, y), & \text{otherwise} \end{cases} . \tag{4.4}$$

The beat frequency f_{12} covers the whole field view of the camera, meaning there is no phase ambiguity in $\varphi_{W12}(x,y)$. $\varphi_{W1}(x,y)$ can be unwrapped by

$$\varphi_{U1}(x,y) = \varphi_{W1}(x,y) + \text{Round}\left[\frac{\varphi_{W12}(x,y)(f_1/f_{12}) - \varphi_{W1}(x,y)}{2\pi}\right], \tag{4.5}$$

where $\varphi_{U1}(x,y)$ is the unwrapped phase of $\varphi_{W1}(x,y)$.

In Equation 4.4, residual phase errors in the wrapped phase maps $\varphi_{W1}(x,y), \varphi_{W2}(x,y)$ may result in spike-like errors in phase map $\varphi_{W12}(x,y)$ if 2π is mistakenly added because of incorrect comparison between $\varphi_{W1}(x,y)$ and $\varphi_{W2}(x,y)$ due to noise in the phase values. The spike-like errors would be further amplified by f_1/f_{12} in the computed unwrapped (absolute) phase map $\varphi_{U1}(x,y)$ if not compensated for, as in Equation 4.5. If the spike-like errors in the unwrapped phase map correspond to camera image coordinates (pixels) where control points used in projector-camera calibration are located, coordinates of the control points in the projector image cannot be correctly determined and the projector calibration will fail, as further explained in Section 4.2.1.

4.2 Camera-Projector Correspondence Construction

4.2.1 Camera-Projector Correspondence from Two Absolute Phase Maps

Correspondence between camera and projector pixels is determined using two orthogonal absolute phase maps. Using a checkerboard planar calibration object (Figure 4-3a), where the inner corners of squares define the control (calibration) points, for each control point $P_c(u_c, v_c)$ of the calibration object in the calibration-object camera image, the correspondence between the camera pixel and projector pixel is determined by matching the absolute phase value pair (φ_V, φ_H) (computed from vertical and horizontal phase-shifted sinusoidal fringe patterns, respectively, Figure 4-2), in the camera and projector images, respectively. Matched point $P_p(u_p, v_p)$ in the projector image (Figure 4-3b), which occurs at the intersection of a

vertical line $u = u_{\mathrm{p}}$ with absolute phase value $\varphi = \varphi_{\mathrm{V}}$ and a horizontal line $v = v_{\mathrm{p}}$ with absolute phase value $\varphi = \varphi_{\mathrm{H}}$, corresponds to control point $P_c(u_c, v_c)$ in the camera image plane (Figure 4-3a). This technique is referred to as the (camera-projector) CP calibration technique hereinafter. Construction of a virtual projector image of the checkerboard is complete once all the control points have been matched.

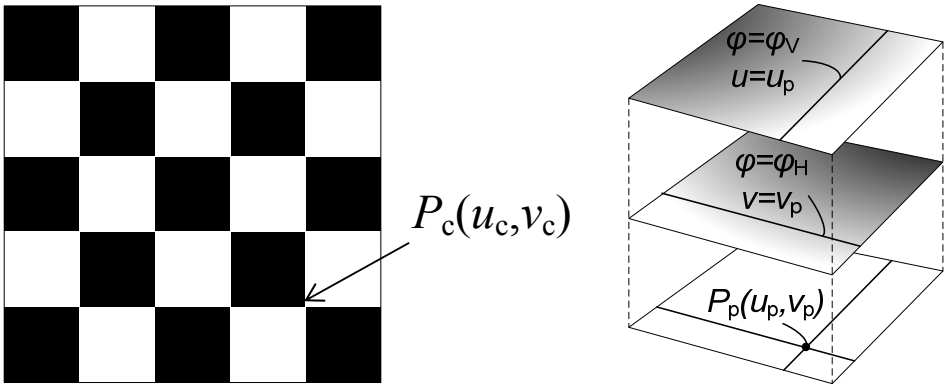

(a) (b)

Figure 4-3 Determination of correspondence between camera and projector pixels showing: (a) camera-captured checkerboard image with calibration point P_{c}, (b) intersection of two absolute phase lines from orthogonal absolute phase maps to locate projector image-plane point P_{p} corresponding to calibration point P_{c}.

Mapping of the camera and projector image coordinates to the world coordinates can be described by

$$s_{\mathrm{c}} \begin{bmatrix} u_{\mathrm{c}} \\ v_{\mathrm{c}} \\ 1 \end{bmatrix} = M_{\mathrm{c}} \begin{bmatrix} \mathrm{X_W} \\ \mathrm{Y_W} \\ \mathrm{Z_W} \\ 1 \end{bmatrix}, \tag{4.6}$$

$$s_{\mathrm{p}} \begin{bmatrix} u_{\mathrm{p}} \\ v_{\mathrm{p}} \\ 1 \end{bmatrix} = M_{\mathrm{p}} \begin{bmatrix} \mathrm{X_W} \\ \mathrm{Y_W} \\ \mathrm{Z_W} \\ 1 \end{bmatrix}, \tag{4.7}$$

where s_c and s_p are scale factors, and M_c implicitly represents the intrinsic and extrinsic parameters for the camera and M_p for the projector. Camera images and the virtual projector images of the checkerboard at several orientations are used to perform camera and projector calibrations [43], where M_c and M_p are solved for in a least-squares sense, using known camera image coordinates (u_c, v_c) and the corresponding world coordinates (X_W, Y_W, Z_W), and using computed projector image coordinates (u_p, v_p) and the corresponding world coordinates, respectively.

During the system calibration, if either or both of the two absolute phase values φ_V, φ_H suffer from spike-like errors, the position of the control point in the projector image cannot be correctly determined, and the projector calibration and associated camera-projector calibration will fail. Compensation for spike-like errors in the absolute phase maps is therefore critical in the camera-projector stereovision-system calibration. The ideal approach (detailed in Section 4.3) to handle the spike-like errors would be to preserve the phase values rather than remove them, in order to preserve the calibration points.

During a surface-shape measurement (once camera-projector system calibration is completed), 3D reconstruction of a surface point P (Figure 4-1) can be performed from its corresponding camera and projector coordinates (u_c, v_c) and (u_p, v_p), and M_c and M_p, respectively, determined during the camera-projector system calibration.

4.2.2 Camera-Projector Correspondence from Absolute Phase Map and Epipolar Geometry

Once the system has been calibrated, the epipolar geometry of the system, well established for stereovision [66], can be known. In epipolar geometry, for a camera pixel, its matching projector pixel must lie on a unique epipolar line that corresponds to the camera pixel. This epipolar geometry, known from the system calibration, permits 3D shape measurement using projection of only one set of fringe patterns (either horizontal or vertical rather than both). Assuming only vertical fringe patterns are used, resulting in an absolute phase map

$\varphi_V(x, y)$, for a camera pixel $P_c(u_c, v_c)$, its matching projector pixel $P_p(u_p, v_p)$ occurs at the intersection of a vertical line with absolute phase value $\varphi = \varphi_V$ and the corresponding epipolar line. This technique will be referred to as the camera-projector-epipolar (CPE) calibration technique hereinafter. The CPE technique can reduce the total number of fringe patterns used for 3D shape measurement to half, compared with the CP technique. However, the CPE technique may suffer from compromised measurement accuracy due to the uncertainty of the computed epipolar line.

4.3 Error-Compensation Heterodyne Phase Unwrapping

A new error-compensation heterodyne phase-unwrapping method was developed to handle the spikes in the absolute phase maps that occur when the original heterodyne method is used. The heterodyne phase-unwrapping method requires projection of at least two sets of sinusoidal fringe patterns, with two frequencies $f_1, f_2 (f_1 > f_2)$, respectively. The two corresponding wrapped phase maps $\varphi_{W1}(x, y), \varphi_{W2}(x, y)$ are determined by Equation 4.2. The phase values $\varphi_{W12}(x, y)$ that correspond to the beat frequency $f_{12} = f_1 - f_2$ can then be computed by

$$\varphi_{W12}(x, y) = \begin{cases} \varphi_{W1}(x, y) - \varphi_{W2}(x, y), & \varphi_{W1}(x, y) > \varphi_{W2}(x, y) \\ 2\pi + \varphi_{W1}(x, y) - \varphi_{W2}(x, y), & \text{otherwise} \end{cases}. \tag{4.8}$$

The random phase errors in the wrapped phase maps $\varphi_{W1}(x, y), \varphi_{W2}(x, y)$, which have Gaussian distribution with standard deviations $\sigma_{\varphi 1}$ and $\sigma_{\varphi 2}$, respectively, may result in spike-like errors in the phase maps $\varphi_{W12}(x, y)$ when 2π is mistakenly added in Equation 4.8 because of incorrect comparison between $\varphi_{W1}(x, y)$ and $\varphi_{W2}(x, y)$ due to noise in the phase values.

As mentioned in Section 4.2.1, preservation of phase values is preferred over removal of phase value outliers to ensure usable camera-projector stereovision-system calibration.

Spike-like errors in the wrapped phase map $\varphi_{W12}(x,y)$, determined in Equation 4.8, should be compensated for as follows:

$$\varphi'_{W12}(x,y)=\begin{cases}\varphi_{W12}(x,y)-2\pi, & -2\sigma_{\varphi}<\varphi_{W1}(x,y)-\varphi_{W2}(x,y)<0 \ \text{ AND} \\ & \varphi_{W1}(x,y)<0 \ \text{ AND } \varphi_{W2}(x,y)<0 \\ 2\pi+\varphi_{W12}(x,y), & 0<\varphi_{W1}(x,y)-\varphi_{W2}(x,y)<2\sigma_{\varphi} \ \text{ AND }, \\ & \varphi_{W1}(x,y)>0 \text{ AND } \varphi_{W2}(x,y)>0 \\ \varphi_{W12}(x,y), & \text{otherwise}\end{cases} \tag{4.9}$$

where σ_{φ} is determined by projecting two sets of phase-shifted patterns onto a flat plate, computing $\sigma_{\varphi 1}$ and $\sigma_{\varphi 2}$ over $\varphi_{W1}(x,y)$ and $\varphi_{W2}(x,y)$, respectively, and selecting $\sigma_{\varphi}=\max\{\sigma_{\varphi 1},\sigma_{\varphi 2}\}$. Equation 4.9 generates a corrected wrapped phase map $\varphi'_{W12}(x,y)$ and thus prevents random errors in the wrapped phase maps from generating spike-like errors in the unwrapped phase map.

If the frequencies f_1 and f_2 are selected such that the period corresponding to the beat frequency $f_{12}=f_1-f_2$ covers the entire field of view of the projector, there would be a single fringe across the field and thus no fringe ambiguity in $\varphi_{W12}(x,y)$. In this case, $\varphi_{W1}(x,y)$ can be unwrapped by

$$\varphi'_{U1}(x,y)=\varphi_{W1}(x,y)+2\pi\times\text{Round}\left[\frac{\varphi'_{W12}(x,y)\times f_1/f_{12}-\varphi_{W1}(x,y)}{2\pi}\right]. \tag{4.10}$$

$\varphi'_{U1}(x,y)$ is the unwrapped phase map of $\varphi_{W1}(x,y)$, and its computation completes the two-frequency phase-unwrapping correction. The ratio between the measurement frequency f_1 and beat frequency f_{12} can be defined as a scale factor, and the period that corresponds to the beat frequency can be defined as the phase-unwrapping range. In Equation 4.10, the spike-

like errors in $\varphi'_{W12}(x,y)$ would be further amplified by the scale factor f_1/f_{12} if not compensated for, and would lead to calibration failure.

Using two-frequency heterodyne phase-unwrapping, the period $P_{12}=1/f_{12}$ corresponding to the beat frequency should be no smaller than the projector resolution R (i.e. $P_{12}\geq R$) for the phase unwrapping range to extend over the projector field of view, and the scale factor is constrained by $f_1/f_{12}\leq 2\pi/6\sqrt{2}\sigma_\varphi$ [22]. Depending on the projector resolution R and σ_φ, two frequencies may not be sufficient to extend the phase-unwrapping range over the entire projector field of view.

Three-frequency heterodyne phase-unwrapping uses three sets of fringe patterns with three frequencies $f_1,f_2,f_3(f_1>f_2>f_3)$. Two scale factors f_1/f_{12} and f_{12}/f_{123} from three beat frequencies, $f_{12}=f_1-f_2$, $f_{23}=f_2-f_3$, and $f_{123}=f_{12}-f_{23}$, are used in the phase-unwrapping process to extend the phase-unwrapping range by $(f_1/f_{12})\times(f_{12}/f_{123})=f_1/f_{123}$, and thus permit a phase-unwrapping range that covers the entire projector field of view. Three wrapped phase maps $\varphi_{W1}(x,y),\varphi_{W2}(x,y),\varphi_{W3}(x,y)$ are determined by Equation 4.2, and have Gaussian distributions with standard deviations $\sigma_{\varphi1},\sigma_{\varphi2}$ and $\sigma_{\varphi3}$, respectively. $\varphi_{W23}(x,y)$ is computed from $\varphi_{W2}(x,y)$ and $\varphi_{W3}(x,y)$ in a similar manner to $\varphi_{W12}(x,y)$ computed in Equation 4.8. Compensation for spike-like errors in the wrapped phase map $\varphi_{W23}(x,y)$ is computed by:

$$\varphi'_{W23}(x,y)=\begin{cases}\varphi_{W23}(x,y)-2\pi, & -2\sigma_\varphi<\varphi_{W2}(x,y)-\varphi_{W3}(x,y)<0 \ \text{AND} \\ & \varphi_{W2}(x,y)<0 \ \text{AND} \ \varphi_{W3}(x,y)<0 \\ 2\pi+\varphi_{W23}(x,y), & 0<\varphi_{W2}(x,y)-\varphi_{W3}(x,y)<2\sigma_\varphi \ \text{AND} \\ & \varphi_{W2}(x,y)>0 \ \text{AND} \ \varphi_{W3}(x,y)>0 \\ \varphi_{W23}(x,y), & \text{otherwise}\end{cases} \quad (4.11)$$

where σ_φ is determined by selecting $\sigma_\varphi = \max\{\sigma_{\varphi 2}, \sigma_{\varphi 3}\}$. $\varphi_{W123}(x,y)$ is computed from $\varphi'_{W12}(x,y)$ and $\varphi'_{W23}(x,y)$ in a similar manner to $\varphi_{W12}(x,y)$ computed in Equation 4.8. Compensation for spike-like errors in the wrapped phase map $\varphi_{W123}(x,y)$ is computed by:

$$\varphi'_{W123}(x,y) = \begin{cases} \varphi_{W123}(x,y) - 2\pi, & -2\sigma_\varphi < \varphi'_{W12}(x,y) - \varphi'_{W23}(x,y) < 0 \text{ AND} \\ & \varphi'_{W12}(x,y) < 0 \text{ AND } \varphi'_{W23}(x,y) < 0 \\ 2\pi + \varphi_{W123}(x,y), & 0 < \varphi'_{W12}(x,y) - \varphi'_{W23}(x,y) < 2\sigma_\varphi \text{ AND }, \\ & \varphi'_{W12}(x,y) > 0 \text{ AND } \varphi'_{W23}(x,y) > 0 \\ \varphi_{W123}(x,y), & \text{otherwise} \end{cases} \quad (4.12)$$

where σ_φ is determined by selecting $\sigma_\varphi = \max\left\{\sqrt{2}\max\{\sigma_{\varphi 1}, \sigma_{\varphi 2}\}, \sqrt{2}\max\{\sigma_{\varphi 2}, \sigma_{\varphi 3}\}\right\}$. $\varphi'_{U1}(x,y)$, the unwrapped phase map of $\varphi_{W1}(x,y)$, is then determined using Equations 4.13 and 4.14, where corrected phase values are used:

$$\varphi'_{U12}(x,y) = \varphi'_{W12}(x,y) + 2\pi \times \text{Round}\left[\frac{\varphi'_{W123}(x,y) \times f_{12}/f_{123} - \varphi'_{W12}(x,y)}{2\pi}\right], \quad (4.13)$$

$$\varphi'_{U1}(x,y) = \varphi_{W1}(x,y) + 2\pi \times \text{Round}\left[\frac{\varphi'_{U12}(x,y) \times f_1/f_{12} - \varphi_{W1}(x,y)}{2\pi}\right]. \quad (4.14)$$

The resulting unwrapped phase map $\varphi'_{U1}(x,y)$ without spike-like errors can then be used in the camera-projector stereovision-system calibration. Simulations and real-system experiments were performed to demonstrate the advantage of the proposed method of phase unwrapping in the system calibration.

4.4 Experiments and Results

4.4.1 Simulation of Phase Unwrapping Without and With Error Compensation

Simulation of phase unwrapping without and with error compensation were carried out using three sets of four camera-captured images of four fringe patterns ($N = 4$ in Equation 4.2)

with phase shifts $0, \pi/2, \pi, 3\pi/2$ along the *x*-axis. The three sets used three frequencies f_1, f_2, f_3 of 1/24, 1/26, and 1/28, respectively, and the three associated beat frequencies f_{12}, f_{23}, f_{123} were 1/312, 1/364, and 1/2184, respectively. The resulting phase-unwrapping range is suitable for a digital projector having a resolution of 2184 or less pixels. Four-step phase-shifting (Equation 4.2) was used to calculate three ideal wrapped phase maps, to which zero mean Gaussian noise was added to simulate real measured wrapped phase maps $\varphi_{W1}(x,y), \varphi_{W2}(x,y)$ and $\varphi_{W3}(x,y)$, with $\sigma_\varphi = 0.05$ rad.

Wrapped phase maps $\varphi_{W12}(x,y_i), \varphi_{W23}(x,y_i)$ and $\varphi_{W123}(x,y_i)$ using the heterodyne method without error compensation are plotted for a single camera-image row with index i in Figure 4-4a. The associated errors in the uncorrected wrapped phase maps are shown in Figure 4-4b. The spike-like errors occurred at pixels 1, 310, and 622 for $\varphi_{W12}(x,y_i)$, pixels 2, 363, and 364 for $\varphi_{W23}(x,y_i)$, and several pixels between 1 and 58 for $\varphi_{W123}(x,y_i)$ (Figure 4-4a and Figure 4-4b). The unwrapped phase map $\varphi_{U1}(x,y_i)$ without error compensation (Figure 4-4c) shows that the spike-like errors in $\varphi_{W123}(x,y_i)$ (Figure 4-4a and Figure 4-4b) are magnified by the frequency ratio f_1/f_{123}, resulting in large spike-like errors of up to 587 rad in Figure 4-4c. The corresponding results using the proposed error compensation are plotted in Figure 4-4d to Figure 4-4f. The corrected wrapped phase maps $\varphi'_{W12}(x,y_i), \varphi'_{W23}(x,y_i)$ and $\varphi'_{W123}(x,y_i)$ using the proposed error-compensation method are plotted for the same single camera-image row with index i in Figure 4-4d. The spike-like errors in the phase maps in Figure 4-4a have been successfully corrected for in Figure 4-4d. Only random errors remain after removal of

Figure 4-4 Simulation results of phase-unwrapping: top row (a, b, c) computed without error compensation: (a) wrapped phase maps $\varphi_{W12}(x,y_i), \varphi_{W23}(x,y_i)$ and $\varphi_{W123}(x,y_i)$, (b) phase errors in wrapped phase maps $\varphi_{W12}(x,y_i), \varphi_{W23}(x,y_i)$ and $\varphi_{W123}(x,y_i)$, (c) unwrapped phase map $\varphi_{U1}(x,y_i)$; and bottom row (d, e, f) computed by the proposed error compensation: (d) wrapped phase maps $\varphi'_{W12}(x,y_i), \varphi'_{W23}(x,y_i)$ and $\varphi'_{W123}(x,y_i)$, (e) phase errors in wrapped phase maps $\varphi'_{W12}(x,y_i), \varphi'_{W23}(x,y_i)$ and $\varphi'_{W123}(x,y_i)$, and (f) unwrapped phase map $\varphi'_{U1}(x,y_i)$.

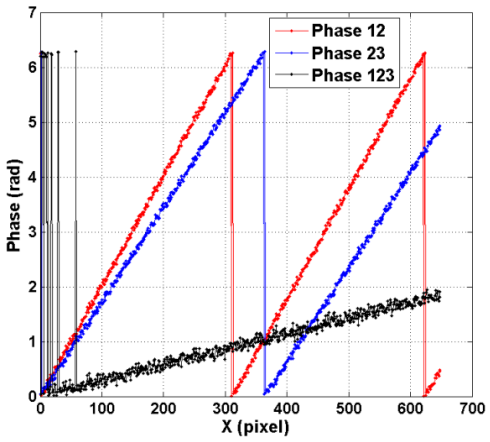
Phase 12
Phase 23
Phase 123
Phase (rad)
X (pixel)

(a)

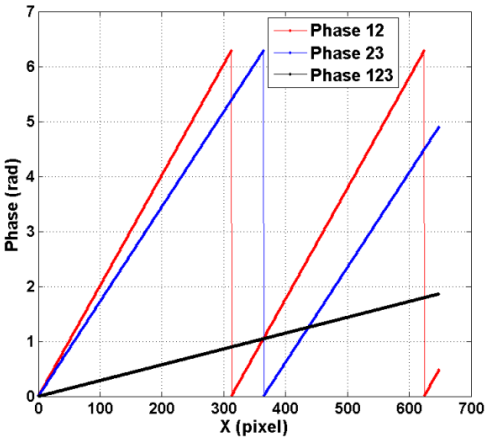
Phase 12
Phase 23
Phase 123
Phase (rad)
X (pixel)

(d)

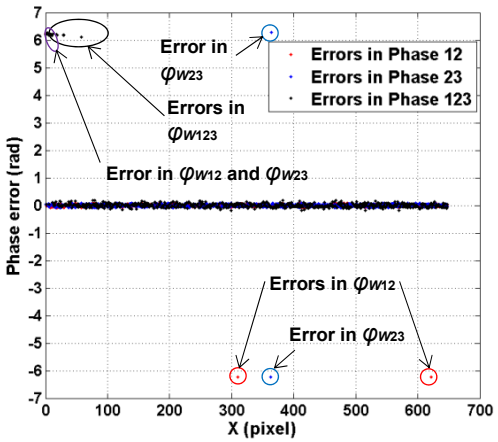
Error in φw23
Errors in φw123
Error in φw12 and φw23
Errors in Phase 12
Errors in Phase 23
Errors in Phase 123
Errors in φw12
Error in φw23
Phase error (rad)
X (pixel)

(b)

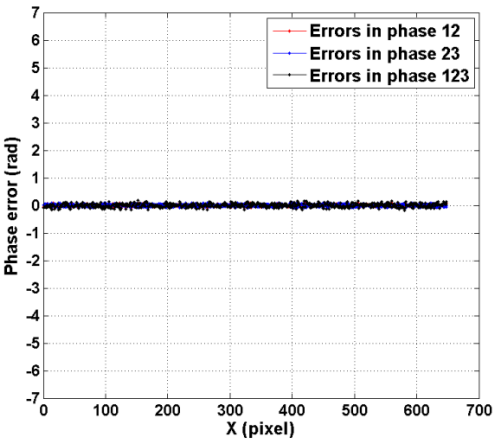
Errors in phase 12
Errors in phase 23
Errors in phase 123
Phase error (rad)
X (pixel)

(e)

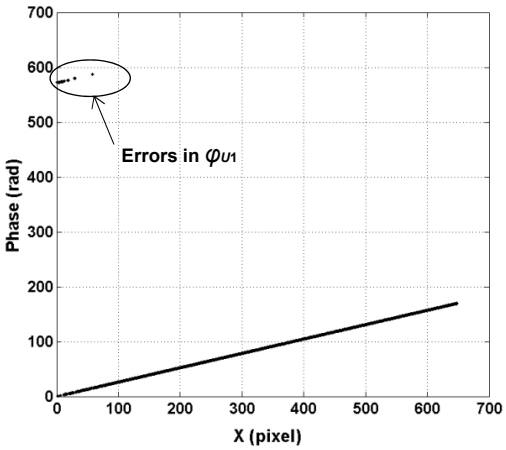
Errors in φU1
Phase (rad)
X (pixel)

(c)

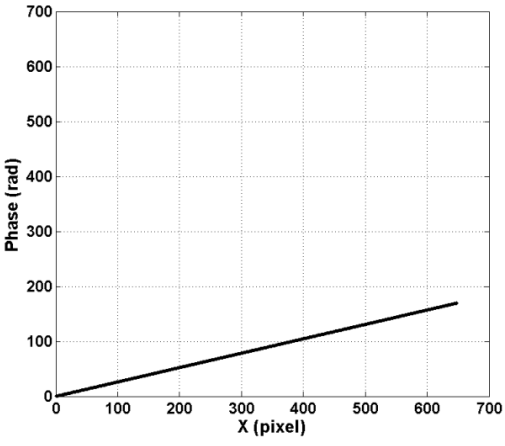
Phase (rad)
X (pixel)

(f)

the spike-like errors (Figure 4-4e). The resulting unwrapped phase map $\varphi'_{U1}(x, y_i)$ continuously increases as expected (Figure 4-4f) without any spike-like errors. This simulation demonstrates the advantage of the proposed method in correcting errors at the phase-unwrapping stage before proceeding with system calibration, and thus in preventing calibration failure.

4.4.2 System Calibration using Phase Unwrapping Without and With Error Compensation

The proposed heterodyne phase-unwrapping method with error compensation was compared to the method without error compensation in a calibration of a real camera-projector stereovision system, as shown schematically in Figure 4-1. A digital light processing (DLP) projector (Optoma PK301, 1024×768, 8-bit) was used for computer-generated fringe-pattern projection. A monochrome CCD camera (Sony XCHR50, 648×494, 8-bit) was used for image capture via a frame-grabber image-processing board (Matrox Odyssey XA). A computer was used for data-processing and process control. A red-and-blue checkerboard with 16×10 inner corners and square size 8×8 mm^2 was used as a calibration object, to achieve a uniform signal-to-noise ratio (SNR) in both red and blue squares in camera-captured fringe pattern images [17].

Two system calibrations were performed where the unwrapped phase maps were obtained by two heterodyne phase-unwrapping methods, without and with error compensation, respectively. For both calibrations, the checkerboard was placed at nine different unknown poses (positions and orientations). Three sets (at three frequencies corresponding to periods 24, 26, and 28 pixels, respectively) of four phase-shifted patterns, projected both horizontally and vertically, were used. The two system calibrations (without and with error compensation) were performed using the exact same camera-captured raw-data images.

Unwrapped phase maps from vertical fringe patterns computed using the two heterodyne phase-unwrapping methods are shown in Figure 4-5a and Figure 4-5b, respectively. Phase values were computed at each pixel within the rectangular area (250 pixel rows × 400 pixel columns) of the camera-captured image that covers all control points. Spike-like errors in the

unwrapped phase computed without error compensation (seen in Figure 4-5a), were corrected using the proposed method, to obtain a continuously increasing unwrapped phase map without spike-like errors, as shown in Figure 4-5b, at all image rows. A sample camera-captured checkerboard image and the detected 2D positions of the control points are shown in Figure 4-6a. The corresponding virtual projector image using phase-unwrapping without error compensation is shown in Figure 4-6b, where 2D positions of three matched control points in the projector image could not be correctly determined. This is because, for each incorrectly matched control point, the phase value of at least one of the four neighboring pixels at the associated control-point 2D position in the camera image, suffered from spike-like errors.

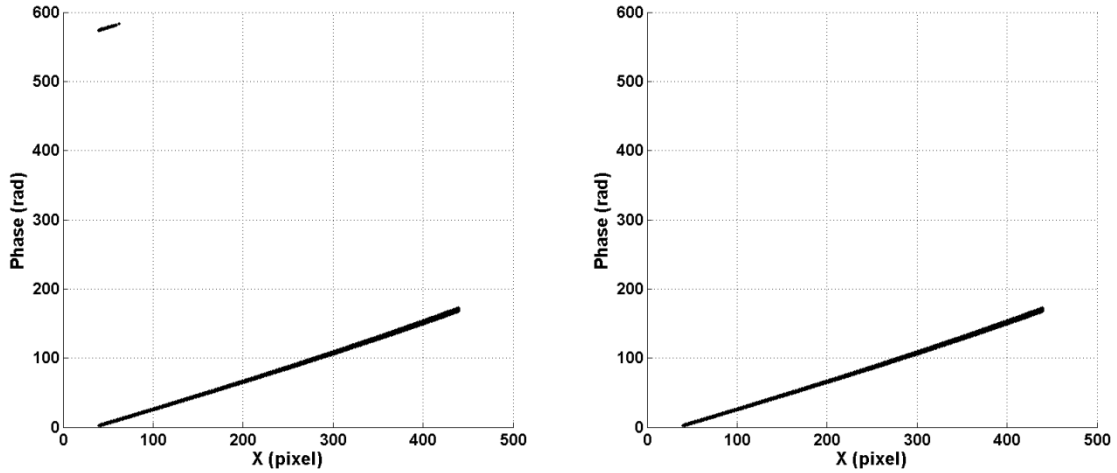

(a) (b)

Figure 4-5 Experimental results of phase-unwrapping: (a) unwrapped phase map computed without error compensation, and (b) unwrapped phase map using the proposed method with error compensation.

The reprojection error, defined as the sum of the squared 2D image distances between 3D corner (control) points projected back to the image plane and the corresponding detected corner points, is the standard measure used to evaluate camera-calibration accuracy. The projector reprojection error computed using phase-unwrapping without error compensation was 18.2 pixels. This large reprojection error indicates that the projector calibration failed and no reasonably accurate measurement would be possible with the stereovision system.

Figure 4-6c shows the virtual projector image using the proposed error-compensation method where the projector reprojection error has been reduced by 99% to 0.2 pixels.

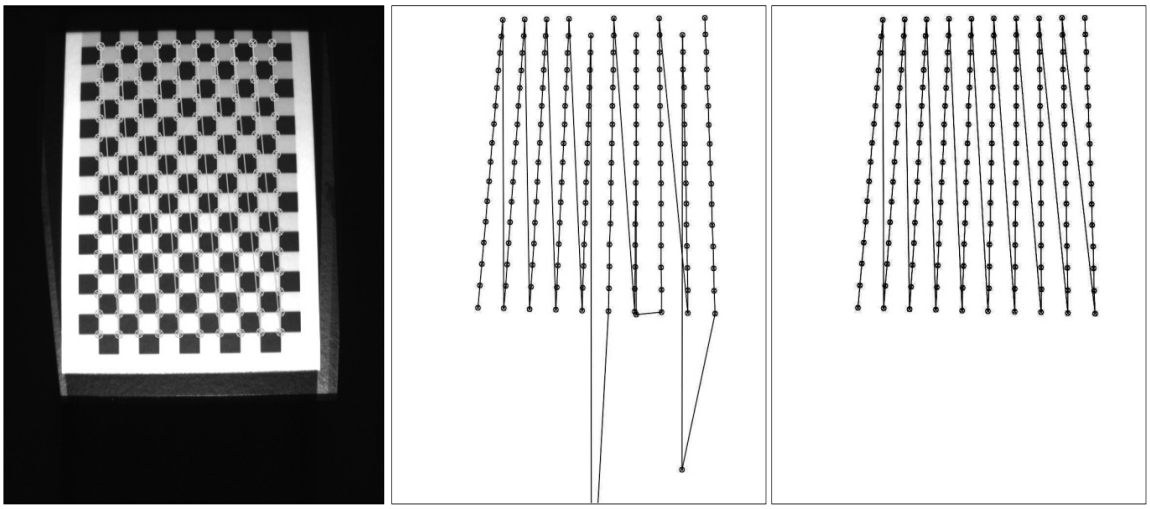

(a) (b) (c)

Figure 4-6 Results of corner detection to locate control points on calibration board: (a) checkerboard with indicated positions of detected corners in the camera image, (b) positions of the matched corners in the projector image using phase unwrapping without error compensation, and (c) positions of the matched corners in the projector image using the proposed phase unwrapping method with error compensation.

Measurements of a flat plate, spherical ball, and mask were enabled by implementing the improved heterodyne phase-unwrapping in the system calibration. The experiments and results are detailed in the following sections.

4.4.3 Real-System Measurement

(1) Flat plate measurement

A flat plate, mounted on a micrometer translation stage, was moved to 26 known positions (0-50 mm with 2 mm intervals) toward the camera-projector, and the plate was measured at each position. At each position, a plane was fitted to the measured points using the least-squares method. The fitted plane at position 26 mm, the centre of the measurement volume, was selected as a reference plane, where the camera and projector were in best focus. The root-mean-square (RMSE) and the standard deviation (SD) of the plane fitting errors, defined in Section 3.1, were computed at each plate position. The RMSE and plane fitting error SD at

the 26 known positions are shown in Figure 4-7. The RMSE decreased to 0.045 mm as the plate was moved toward the reference position where the camera and projector were in best focus. The plane fitting error SD was nearly constant across depth.

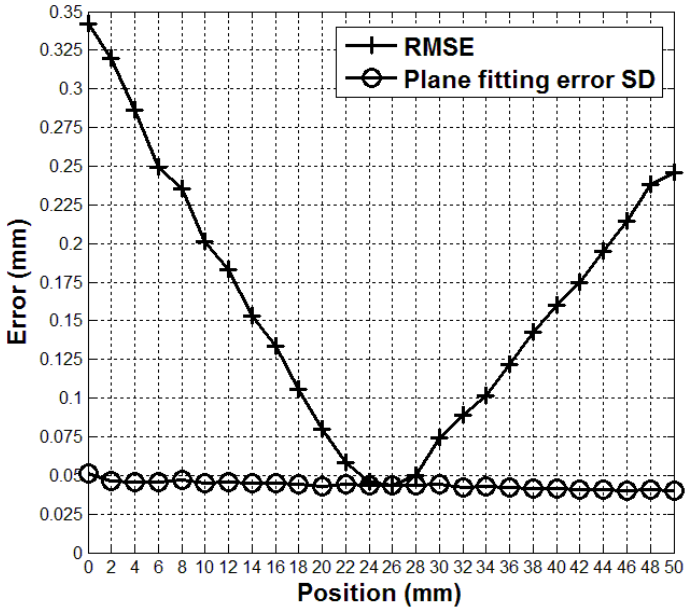

Figure 4-7 RMSE and plane fitting error SD in measuring a flat plate at 26 known positions.

(2) Spherical Ball Measurement

A spherical ball was measured at the same 26 known positions as in the plate measurement with the same reference position. At each position, a sphere was fitted to the measured points and the following computations were made: the SD of the sphere fitting errors, the mean absolute radius error e_r, and the absolute centre-to-centre distance error e_c, as defined in Section 3.2.

The sphere fitting error SD, mean absolute radius error, and absolute centre-to-centre error at the 26 known positions are shown in Figure 4-8. The mean absolute radius error decreased from 0.312 mm at position 0 mm to 0.046 mm at position 28 mm, and then increased to 0.289 mm at position 50 mm. The lowest error 0.046 mm occurred close to where the camera was in best focus. The absolute centre-to-centre distance errors varied from lowest error 0.002 mm at position 28 mm near the best camera focus to 0.080 mm at position 50 mm. The

error curve had an additional minimum at position 6 mm and a peak at 18 mm. This may be due to multiple effects, such as the varying light reflected to the camera and contrast ratio with changing angle between the surface normal and the projector and camera optical axes, with different ball positions. The sphere fitting error SD was nearly constant across depth.

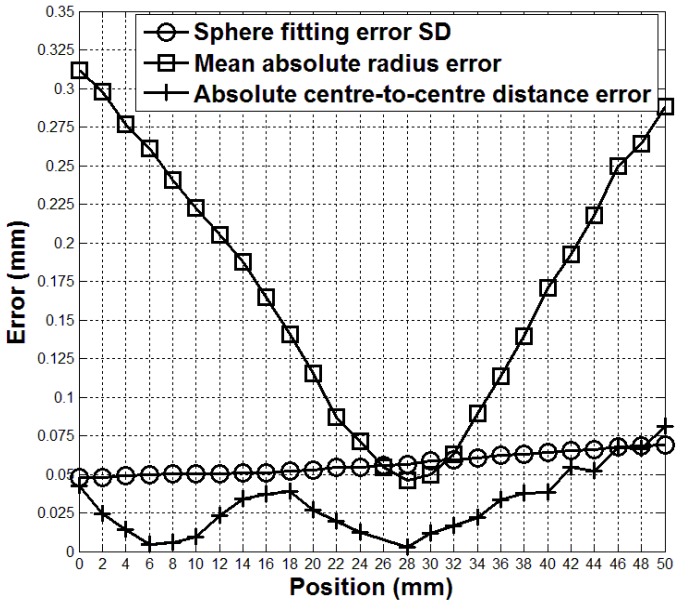

Figure 4-8 Sphere fitting error SD, mean absolute radius error, and absolute centre-to-centre distance error in measuring a spherical ball at 26 known positions.

(3) Mask Measurement

A wooden mask, shown in the 2D image in Figure 4-9a, was measured once the system calibration was completed using the proposed phase unwrapping method. The 3D mask surface reconstructed from the measurement, shown as a 3D point cloud in Figure 4-9b and Figure 4-9c, demonstrates that the proposed heterodyne phase-unwrapping method permitted surface-shape measurement of the mask. Close-up 3D point cloud views show details of wrinkles and teeth, in Figure 4-9d and Figure 4-9e, respectively. The 3D reconstructed mask surface with intensity texture overlaid onto each point of a 3D point cloud is shown in Figure 4-9f. All figures of 3D reconstructions (Figure 4-9b to Figure 4-9f) show raw 3D data points with no smoothing applied.

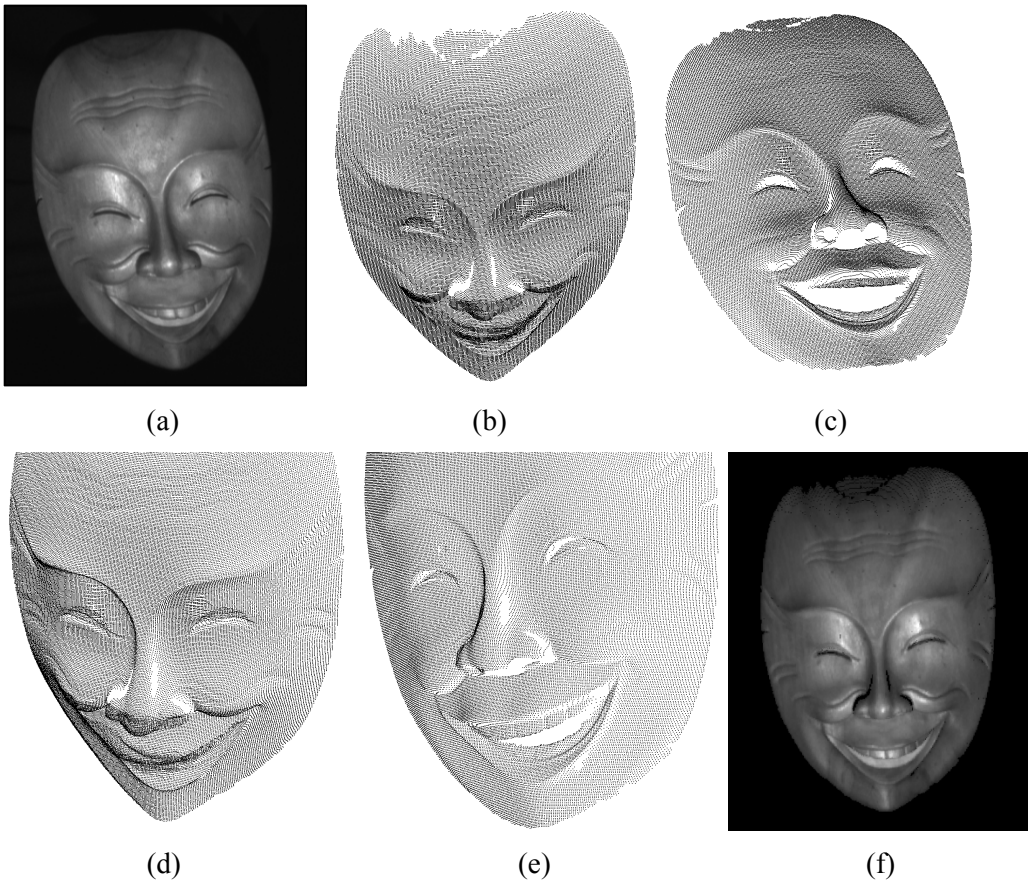

Figure 4-9 Measurement results of a mask: (a) 2D mask image, (b-c) 3-D point clouds of the reconstructed measured surface, (d-e) close-up 3-D point clouds of the reconstructed measured surface, and (f) 3-D point cloud of the reconstructed measured surface with overlaid intensity texture. 3D reconstructions in (b-f) show raw measured 3D data points with no smoothing.

4.5 Summary

The newly-developed error-compensation heterodyne phase-unwrapping method for camera-projector stereovision-system calibration was able to detect and compensate for spike-like errors at the phase-unwrapping stage before proceeding with system calibration in both the simulation and real-system experiments. It was demonstrated that phase values at control points could be preserved for use in the camera-projector stereovision-system calibration. Measurement-system calibration experiments demonstrated that the error-compensation method, compared with the original method [25], could greatly reduce the projector re-projection error. The error compensation thus plays an important role in permitting the camera-projector stereovision-system calibration without failure. Furthermore, preservation

of calibration points on the perimeter of the control-point grid maintains a larger calibration volume. The error-compensation heterodyne phase-unwrapping method was successfully applied in a system calibration used in surface-shape measurement of test objects.

Chapter 5
Adaptive Fringe-Pattern Projection

This chapter presents a newly developed adaptive fringe-pattern projection (AFPP) method that modifies the maximum input gray level (MIGL) locally in the projected fringe patterns based on the saturated pixels in the captured images of the surface being measured. The method enables only three sets of fringe-pattern images to be required for phase computation and 3D surface-shape measurement. The AFPP method thus improves over existing high-dynamic-range (HDR) 3D imaging methods (reviewed in Section 2.3) by requiring many fewer sets of fringe patterns projected and images captured to achieve image saturation avoidance.

5.1 Principles of Adaptive Fringe-Pattern Projection

Using a high MIGL to the projector may result in image saturation, where the camera-captured image intensities $I_i(x_c, y_c)$ of the fringe patterns would be truncated to the maximum gray level of the camera (255 for an 8-bit camera), shown by flat regions in Figure 5-1. The resulting incorrect intensities would generate phase error and associated 3D surface-shape measurement error. Image saturation should thus be compensated for in the fringe-pattern projection and image capture procedures before phase computation.

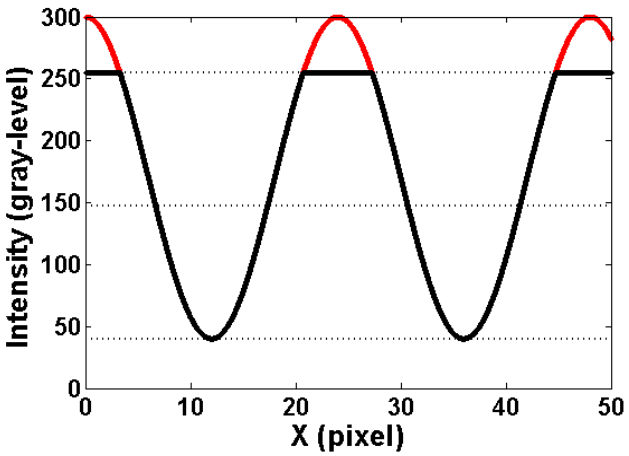

Figure 5-1 Truncated fringe-pattern intensity profile (flat region) due to image saturation

Previous approaches of using global parameters that are constant for the entire pattern or image (e.g. global MIGL or exposure time) require the acquisition of multiple sets of phase-shifted images with a different value of global parameter for each set of phase-shifted images, in order to compose composite images for phase computation. The adaptive fringe-pattern projection (AFPP) method presented in this thesis locally modifies MIGL parameter values across the projected pattern, and thus camera image, to avoid image saturation, instead of repeatedly employing a single global value that is constant across the image, and forming a composite image as a postprocess. This allows local pixel-level fringe pattern adaptation in regions that would otherwise be saturated, and the method is performed at the initial stage of fringe-projection profilometry, during pattern projection, rather than forming composite images as a postprocess to image acquisition, as in current HDR methods. The method enables only three sets of fringe-pattern images to be required for phase computation and surface-shape measurement.

The adaptive fringe-pattern projection (AFPP) method achieves image saturation avoidance using three rounds of fringe-pattern projection with 1) a high global MIGL (constant globally across all pixels of the entire pattern) to identify the saturated camera pixels and determine the corresponding projector pixels to modify, 2) a low global MIGL to determine the local adaptation of MIGLs required, and 3) locally adapted MIGLs to perform adaptive fringe-pattern projection for 3D surface-shape measurement, as detailed below.

1) Round One: Determination of saturated camera pixels and projector pixels to modify

Identification and clustering of saturated pixels is performed using a high global MIGL set to 255 in all fringe patterns as it is the highest possible gray level input to the projector (for an 8-bit projector). The camera exposure time is adjusted to ensure high intensity modulation of captured fringe patterns in dark image regions, regardless of image saturation occurring in bright image regions. For each camera pixel, if the captured intensity $I_{ijq}(x_c, y_c)$ from any fringe-pattern image (for any phase shift $i \in [1, N]$, fringe frequency $j \in [1, J]$, or fringe direction $q \in [1, Q]$) reaches 255, the pixel is identified as a saturated pixel. A camera mask image $M_C(x_c, y_c)$ is then generated by:

$$M_{\mathrm{C}}\left(x_{\mathrm{c}}, y_{\mathrm{c}}\right)=\begin{cases}255, & \text{for any } I_{ijq}\left(x_{\mathrm{c}}, y_{\mathrm{c}}\right)=255 \\ 0, & \text{otherwise}\end{cases}. \tag{5.1}$$

In the camera mask image, connected saturated pixels form saturated-pixel clusters. Contours just outside of each saturated-pixel cluster, cluster-bounding contours, are determined by border following [67]. Contour pixels are unsaturated and can thus be used to determine matching contour pixels in a projector image, and thus determine projector-image matching cluster-bounding contours. For each contour pixel with camera coordinates $\left(x_{\mathrm{c}}, y_{\mathrm{c}}\right)$, the matching contour pixel projector coordinates $\left(x_{\mathrm{p}}, y_{\mathrm{p}}\right)$ can be computed by:

$$\begin{cases}x_{\mathrm{p}}=T\times\phi_{\mathrm{V}}\left(x_{\mathrm{c}}, y_{\mathrm{c}}\right)/2\pi \\ y_{\mathrm{p}}=T\times\phi_{\mathrm{H}}\left(x_{\mathrm{c}}, y_{\mathrm{c}}\right)/2\pi\end{cases}, \tag{5.2}$$

where absolute phase maps $\phi_{\mathrm{V}}(x_{\mathrm{c}}, y_{\mathrm{c}})$ and $\phi_{\mathrm{H}}(x_{\mathrm{c}}, y_{\mathrm{c}})$ are computed from vertical and horizontal fringe patterns, respectively, and T is the projected fringe period. As done for the camera, a projector mask image $M_{\mathrm{P}}\left(x_{\mathrm{p}}, y_{\mathrm{p}}\right)$ can be generated to include all matching saturated-pixel clusters, where pixels on and inside all matching cluster-bounding contours are labeled 255 (saturated), and the remaining pixels are labeled 0 (unsaturated). The matching clusters in the projector mask thus indicate where MIGLs should be adapted in all fringe patterns, to specially illuminate surface regions that lead to image saturation when a high global MIGL is used.

2) Round Two: Determination of local MIGL adaptation required

The adapted MIGLs are determined using a low global MIGL set to 120 in all fringe patterns. The low global MIGL 120 is an approximate median value over the projector input gray level range and was selected to be sufficiently low to ensure that saturation does not occur at any of the K saturated-pixel clusters in the camera mask image determined in Round One. Too high a MIGL value in Round Two would cause some pixels to be saturated in Round Two, and one or more additional rounds would be required to obtain phase values at those remaining saturated pixels. For all saturated pixels that belong to the kth $(k=1,2,...,K)$

cluster, the matching projector coordinates $(x_{\mathrm{p}}, y_{\mathrm{p}})$ corresponding to the camera coordinates $(x_{\mathrm{c}}, y_{\mathrm{c}})$ are determined using Equation 5.2 from two absolute phase maps $\phi_{\mathrm{V}}(x_{\mathrm{c}}, y_{\mathrm{c}})$ and $\phi_{\mathrm{H}}(x_{\mathrm{c}}, y_{\mathrm{c}})$ newly computed from the vertical and horizontal fringe patterns, respectively, using the low global MIGL. To determine the relationship of camera-captured intensities to projector-input intensities for each cluster, the captured intensities $I_{ijq,k}(x_{\mathrm{c}}, y_{\mathrm{c}})$ at saturated camera pixels $(x_{\mathrm{c}}, y_{\mathrm{c}})$, wherever $M_{\mathrm{C}}(x_{\mathrm{c}}, y_{\mathrm{c}}) = 255$, are mapped to their corresponding input intensities $I_{ijq,k}(x_{\mathrm{p}}, y_{\mathrm{p}})$ at projector pixels $(x_{\mathrm{p}}, y_{\mathrm{p}})$, wherever $M_{\mathrm{P}}\left(x_{\mathrm{p}}, y_{\mathrm{p}}\right) = 255$, by:

$$I_{ijq,k}(x_{\mathrm{p}}, y_{\mathrm{p}}) = a_{1,k} \times I_{ijq,k}^{\ a_{2,k}}(x_{\mathrm{c}}, y_{\mathrm{c}}) + a_{3,k}, \tag{5.3}$$

where $a_{1,k}, a_{2,k}, a_{3,k}$ are the coefficients that define the intensity mapping for the kth cluster and need to be determined. The coefficients $a_{1,k}, a_{2,k}, a_{3,k}$ are determined for the kth cluster through weighted nonlinear least-squares regression, which iteratively optimizes the three coefficients using the Levenberg-Marquardt algorithm:

$$\underset{\{a_{1,k}, a_{2,k}, a_{3,k}\}}{\arg\min} \left\{ \sum_{i\in[1,N], j\in[1,J], q\in[1,Q]} \left[\left[a_{1,k}^{\ -1} \times \left(I_{ijq,k}(x_{\mathrm{p}}, y_{\mathrm{p}}) - a_{3,k} \right) \right]^{1/a_{2,k}} - I_{ijq,k}(x_{\mathrm{c}}, y_{\mathrm{c}}) \right]^2 \right\}. \tag{5.4}$$

The MIGL that maintains the largest intensity modulation without image saturation for the kth cluster is thus determined by:

$$I_{\mathrm{Max},k} = a_{1,k} \times 254^{a_{2,k}} + a_{3,k}. \tag{5.5}$$

Adapted MIGLs $I_{\mathrm{Max},k}$ ($k = 1, 2, ..., K$) can thus be obtained to account for all clusters.

In Round Two, the determination of coefficients by Equation 5.4 essentially fits a curve to map camera-captured intensities to projector-input intensities in order to estimate the best adapted MIGL corresponding to camera-captured intensity 254 by Equation 5.5. Too low a MIGL value in Round Two would cause intensity values to be distributed lower on the curve (farther from 254) and could result in a poorer estimated MIGL corresponding to camera intensity 254.

3) Round Three: Adaptive fringe-pattern projection

Adapted phase-shifted fringe patterns for 3D surface-shape measurement are generated by using the high MIGL 255 (employed in Round One) at projector pixels wherever $M_{\mathrm{P}}\left(x_{\mathrm{p}}, y_{\mathrm{p}}\right)=0$, and the adapted MIGLs $I_{\mathrm{Max},k}\,(k=1,2,...,K)$ at projector pixels wherever $M_{\mathrm{P}}\left(x_{\mathrm{p}}, y_{\mathrm{p}}\right)=255$. Note that if a MIGL value lower than 255 were used in Round One, the system would not be able to detect at which pixels saturation would occur, when MIGL is later set to 255 in Round Three for all pixels that did not saturate in Round One.

Such-generated fringe patterns permit high intensity modulation across each captured fringe-pattern image as in the composite fringe-pattern images obtained by high dynamic range 3D imaging methods, but with additional advantages. Instead of capturing a set of fringe patterns repeatedly at many camera exposure times or MIGLs, the AFPP method captures one set of adapted fringe patterns that locally adjust the illumination according to the reflectivity characteristics of local surface regions after only two preliminary rounds. The AFPP method also does not require any additional optical and control hardware.

5.2 Experiments and Results

To demonstrate the effectiveness of the AFPP method, a board with a large range in surface reflectivity, a black planar board with a 10×8 grid of white circles, was measured in three tests: with no AFPP, simplified AFPP, and AFPP, respectively. For no AFPP, two tests were performed, the first with a high global MIGL set to 255 for all fringe patterns, the second with a low global MIGL set to 120. For simplified AFPP, the adapted fringe patterns were generated using the high MIGL in Round One of AFPP (MIGL=255) at pixels labeled 0 (unsaturated) in the projector mask image, and the low MIGL in Round Two of AFPP (MIGL=120) at pixels labeled 255 (saturated) in the projector mask image. There was no further adaptation of MIGLs for the simplified AFPP. For AFPP, the full method described in the previous section was followed. A wooden mask with different surface colors was also measured using 255, 120, and adaptive MIGL methods.

For all tests, the measurement system used a monochrome 1024×1024 8-bit CCD camera and a 1024×768 8-bit digital-light-processing (DLP) projector. The four-step phase-shifting algorithm was used for phase computation. Three frequencies corresponding to periods 24, 26, and 28, were used for phase unwrapping.

5.2.1 Planar Board Measurement

5.2.1.1 Measurement without AFPP

For the first test, one of the vertical fringe patterns using a high global MIGL 255 is shown in Figure 5-2a, with the corresponding captured fringe-pattern image in Figure 5-2b. With the high MIGL 255, image saturation occurred in some of the white-circle regions in Figure 5-2b, resulting in errors seen as discontinuities in the absolute phase map in Figure 5-2c. For the second test, one of the vertical fringe patterns using a low global MIGL 120 is shown in

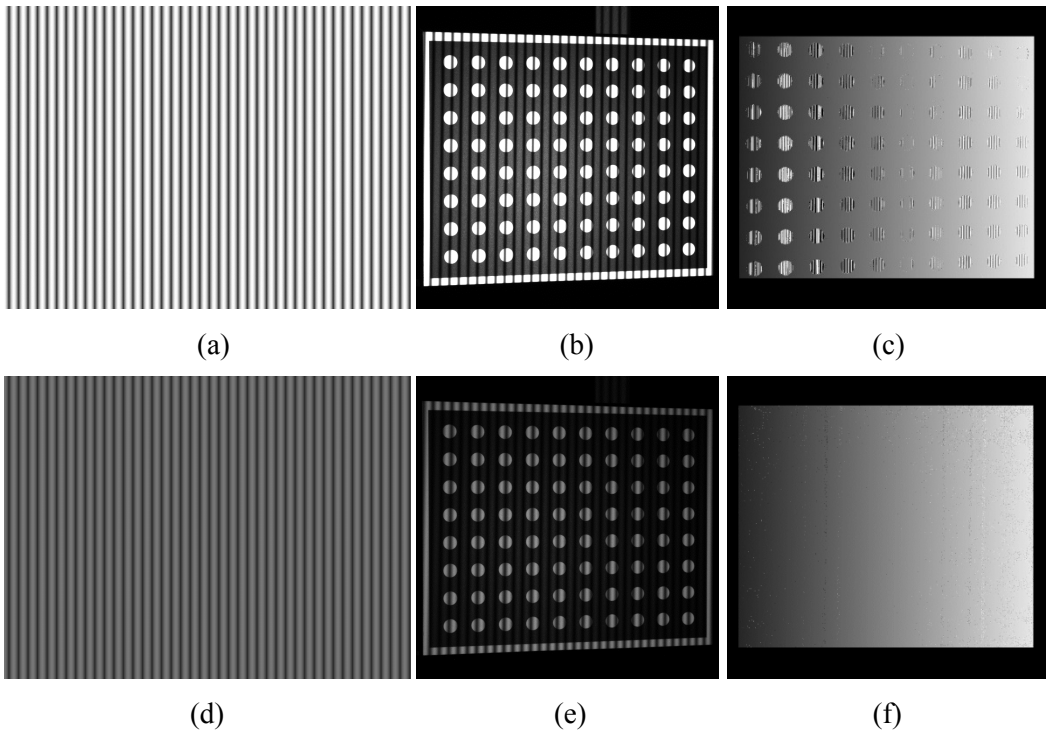

Figure 5-2 A single vertical fringe pattern and corresponding captured image in planar board measurement with no AFPP: (a) fringe pattern with global MIGL 255, (b) captured image of planar board with projection of the pattern in (a), (c) absolute phase map of planar board from (b), (d) fringe pattern with global MIGL 120, (e) captured image of planar board with projection of the pattern in (d), (f) absolute phase map of planar board from (e).

Figure 5-2d, and the corresponding captured fringe-pattern image in Figure 5-2e. With the low MIGL 120, intensity modulation of the captured fringe pattern is very low in the black region, as seen in Figure 5-2e, with resulting errors slightly visible as discontinuities in the absolute phase map in Figure 5-2f. Image saturation and low intensity modulation will both result in large measurement errors, as demonstrated below.

Results of the planar board measurement using a global MIGL 255 are shown in Figure 5-3: Figure 5-3a to Figure 5-3c for the black region and Figure 5-3d to Figure 5-3f for the white-circle regions. Measured points in the black and white-circle regions are shown in Figure 5-3a and Figure 5-3d, respectively. A plane was fit to all measured points excluding the white-circle regions, which had large errors. The measurement error at each point was calculated based on the distance between the measured point and the fitted plane. The 3D reconstruction from the measurement can be clearly seen to properly represent the black region of the board in Figure 5-3a to Figure 5-3b, with most errors in the range [-0.25, +0.25] mm, seen in Figure 5-3b to Figure 5-3c. However, the measurement in the white-circle regions of the board had extremely large errors, the extent of which can be observed in Figure 5-3d and Figure 5-3e, where there is a scatter of 3D points very far from the concentration of points close to the board, seen in Z and in X and Y, respectively, and in Figure 5-3f, where a concentration of large errors up to 1000 mm and more extreme outlier errors are seen. The much larger errors in the white-circle regions (Figure 5-3e to Figure 5-3f) compared to the black regions (Figure 5-3b to Figure 5-3c) are due to image saturation that occurred in the white-circle regions (Figure 5-2b). The root mean square (RMS) error was 0.287 mm in the black region, 558.277 mm in the white-circle regions, and 14.035 mm over the entire surface, respectively.

Figure 5-3 Results of planar board measurement with global MIGL 255 for: (a)-(c) black region: (a) 3D point cloud data, (b) point cloud view of board showing measurement errors in colour, and (c) measurement errors; and (d)-(f) white regions: (d) 3D point cloud data, (e) point cloud view of board showing measurement errors in colour, and (f) measurement errors. Note that scales are different for black and white regions because of the size of errors.

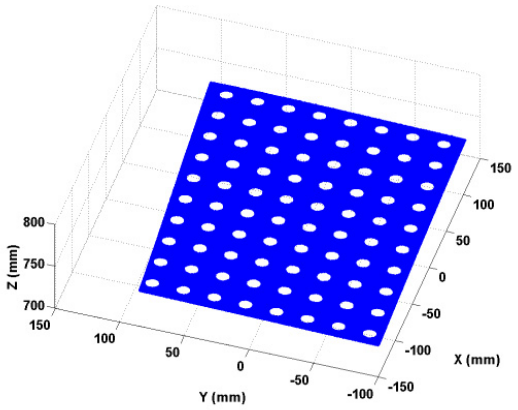
Z (mm)
800
750
700
150
100
50
0
-50
-100
Y (mm)
150
100
50
0
-50
-100
-150
X (mm)

(a)

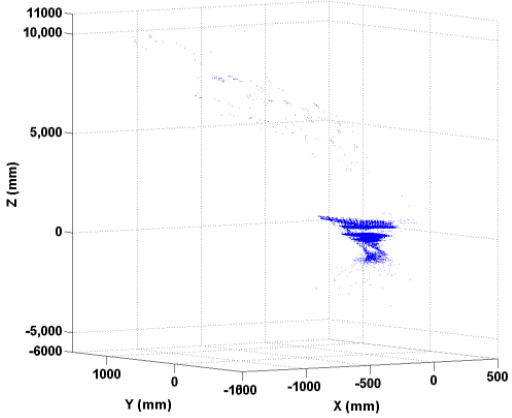
11000
10,000
5,000
0
-5,000
-6000
Z (mm)
1000
0
-1000
Y (mm)
-1800
-1000
-500
0
500
X (mm)

(d)

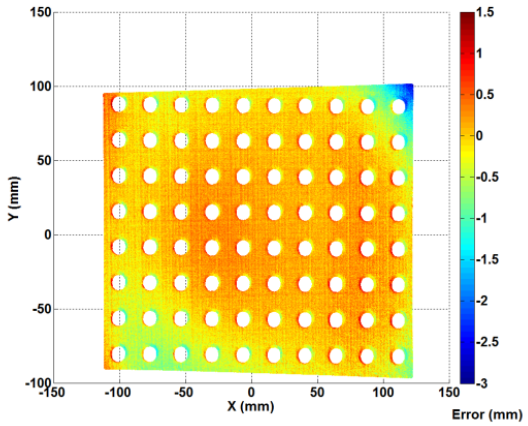
150
100
50
0
-50
-100
Y (mm)
-150
-100
-50
0
50
100
150
X (mm)
1.5
1
0.5
0
-0.5
-1
-1.5
-2
-2.5
-3
Error (mm)

(b)

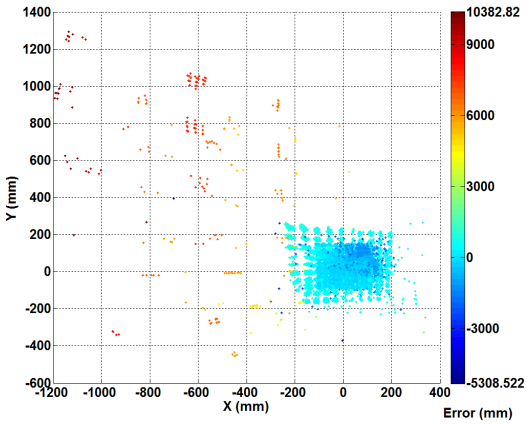
1400
1200
1000
800
600
400
200
0
-200
-400
-600
Y (mm)
-1200
-1000
-800
-600
-400
-200
0
200
400
X (mm)
10382.82
9000
6000
3000
0
-3000
-5308.522
Error (mm)

(e)

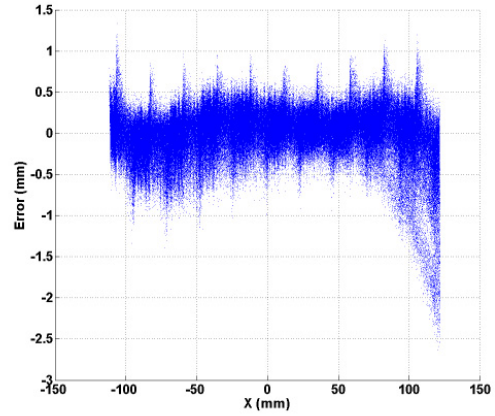
1.5
1
0.5
0
-0.5
-1
-1.5
-2
-2.5
-3
Error (mm)
-150
-100
-50
0
50
100
150
X (mm)

(c)

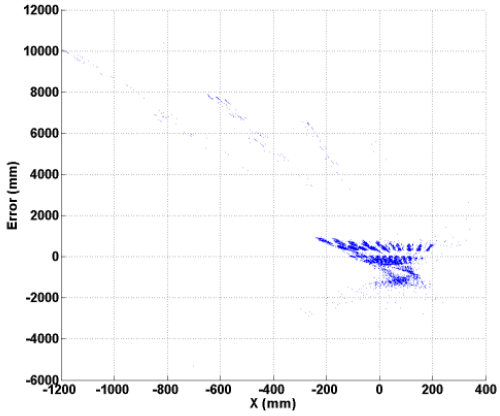
12000
10000
8000
6000
4000
2000
0
-2000
-4000
-6000
Error (mm)
-1200
-1000
-800
-600
-400
-200
0
200
400
X (mm)

(f)

Results of the planar board measurement using a global MIGL 120 are shown in Figure 5-4: Figure 5-4a to Figure 5-4c for the black region and Figure 5-4d to Figure 5-4f for the white-circle regions. Measured points in the black and white-circle regions are shown in Figure 5-4a and Figure 5-4d, respectively. A new plane was fit to all the measured points excluding the black region, which had large errors. As before, the measurement error at each point was calculated based on the distance between the measured point and the fitted plane. The 3D reconstruction from the measurement can be clearly seen to properly represent the white-circle regions of the board in Figure 5-4d to Figure 5-4e, with most errors in the range [-0.25, +0.25] mm, seen in Figure 5-4e to Figure 5-4f. However, the measurement in the black region of the board had large errors, the extent of which can be observed in Figure 5-4a and Figure 5-4b, where there are two large groups of 3D points approximately 250 mm and 500 mm in Z away from the concentration of points close to the board and as high as approximately 100 mm away in X and Y, respectively, and in Figure 5-4c, where large errors are also seen. Even greater errors are seen as scattered 3D points in Figure 5-4a and Figure 5-4b and as outliers in Figure 5-4c. The larger measurement errors in the black region (Figure 5-4b to Figure 5-4c) compared to those in the white-circle regions (Figure 5-4e to Figure 5-4f) are due to the low intensity modulation in the black region (Figure 5-2e), although these errors were not as large as the errors due to image saturation with MIGL 255 (Figure 5-3e to Figure 5-3f). The larger errors due to image saturation compared to those from low intensity modulation are also seen in the absolute phase map discontinuities Figure 5-2c and Figure 5-2f in described earlier. The RMS error was 58.275 mm in the black region, 0.260 mm in the white-circle regions, and 52.235 mm over the entire surface, respectively. Measurement results with no AFPP demonstrate that using a single global MIGL, whether high or low, with a single camera aperture setting and exposure time, accurate measurement cannot be achieved simultaneously at both black and white-circle regions.

Figure 5-4 Results of planar board measurement with global MIGL 120 for: (a)-(c) black region: (a) 3D point cloud data, (b) point cloud view of board showing measurement errors in colour, and (c) measurement errors; and (d)-(f) white regions: (d) 3D point cloud data, (e) point cloud view of board showing measurement errors in colour, and (f) measurement errors. Note that scales are different for black and white regions because of the size of errors. Scales for Figure 5-4d to Figure 5-4f are the same as in Figure 5-3a to Figure 5-3c, where the errors were low.

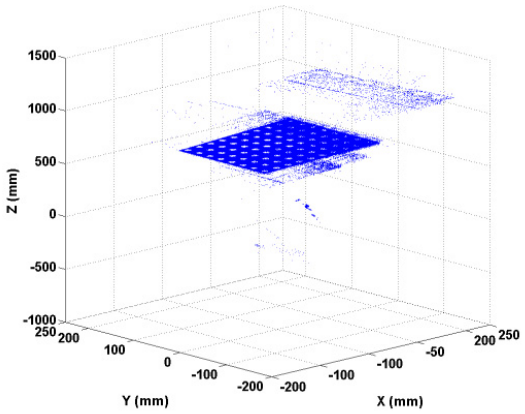
Z (mm)
Y (mm)
X (mm)

(a)

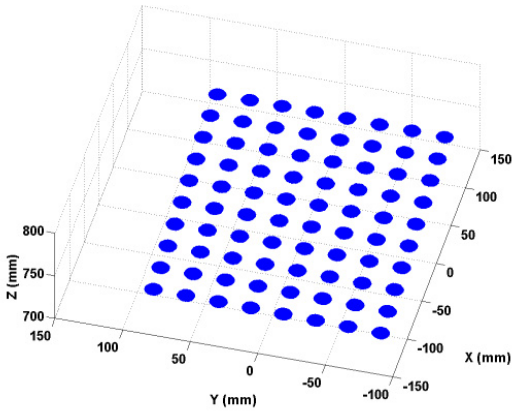
Z (mm)
Y (mm)
X (mm)

(d)

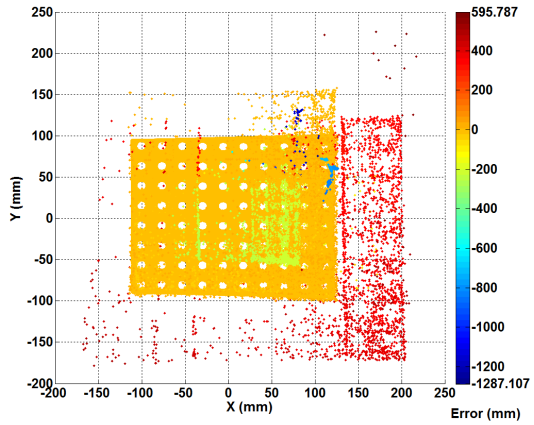
Y (mm)
X (mm)
Error (mm)

(b)

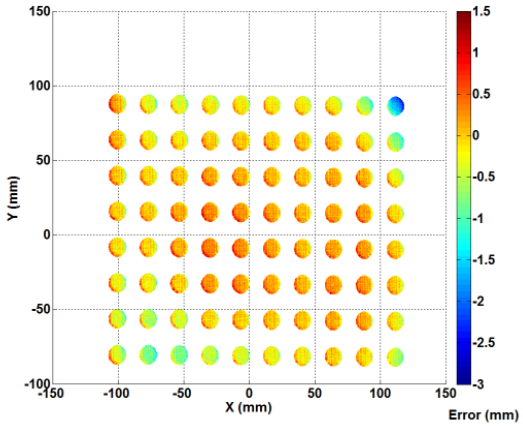
Y (mm)
X (mm)
Error (mm)

(e)

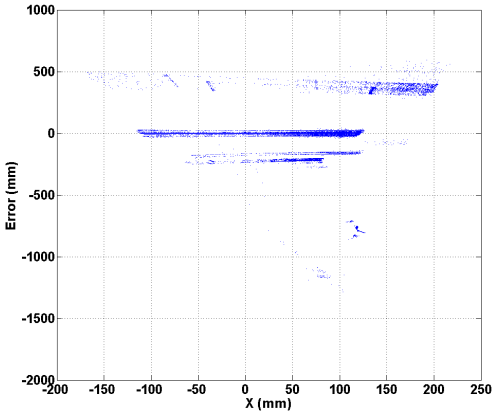
Error (mm)
X (mm)

(c)

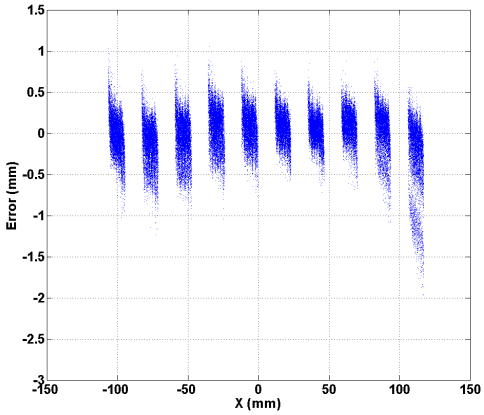
Error (mm)
X (mm)

(f)

5.2.1.2 Measurement with Simplified AFPP

Results of the planar board measurement with simplified AFPP are shown in Figure 5-5. In all of the adapted fringe patterns, the high MIGL 255 was used for illuminating the black region, and the low MIGL 120 was used for illuminating the white-circle regions. Errors in both black and white-circle regions were reduced to similar low levels. Plane fitting was thus performed to all measured points. The RMS error was 0.277 mm in the black region, 0.253 mm in the white-circle regions, and 0.273 mm over the entire surface. The simplified AFPP was an improvement over no AFPP with 99.52% and 99.95% error reductions in the black and white-circle regions, respectively. However, the low MIGL 120 for all white-circle regions may not be ideal. Firstly, the local luminance is, in general, affected by the local surface normal, and the lighting and viewing angles in addition to the local surface reflectivity. The MIGL should ideally be locally adapted for each specific white-circle region to avoid saturation. Secondly, the MIGL 120 may be too low to ensure high intensity modulation without saturation. The improvement by local adaptation was demonstrated in the AFPP (described below).

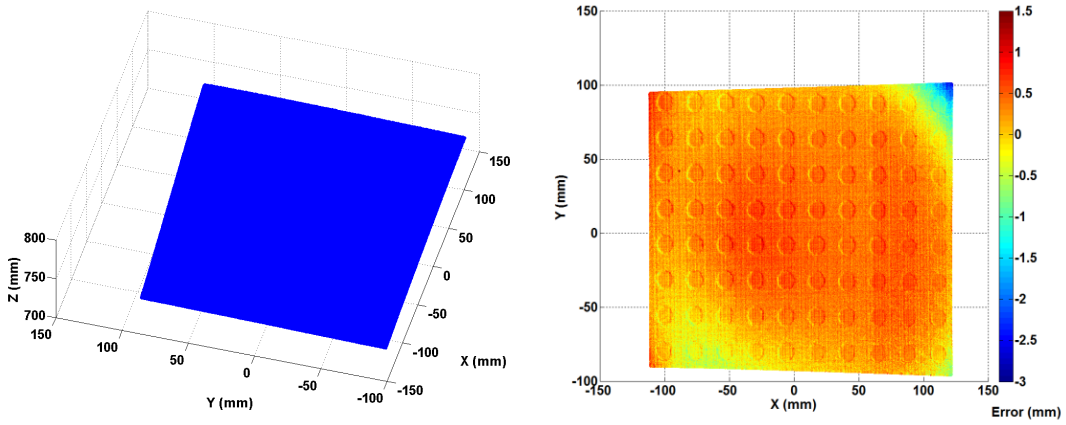

(a) (b)

Figure 5-5 Results of planar board measurement with simplified AFPP: (a) 3D point cloud data of entire surface, (b) point cloud view of board showing measurement errors in colour for entire surface. Scales for Figure 5-5a to Figure 5-5b are the same as in Figure 5-4d to Figure 5-4e and Figure 5-3a to Figure 5-3b, where the errors were low.

5.2.1.3 Measurement with AFPP

One of the adapted vertical fringe patterns used in AFPP is shown in Figure 5-6a. With adapted MIGLs computed in Equation 5.5 ranging from 151 to 185 for illuminating different white-circle regions, large intensity modulation without image saturation can be achieved in both black and white-circle regions in the corresponding captured image of the fringe-pattern on the board (Figure 5-6b). The absolute phase map of the board for AFPP in Figure 5-6c has no apparent discontinuity or visible error, and is an improvement compared to the discontinuities seen in Figure 5-2c due to MIGL 255 in the white regions, and Figure 5-2f due to MIGL 120 in the dark regions. Results of the planar board measurement with AFPP are shown in Figure 5-7. The RMS error was 0.276 mm in the black region, 0.229 mm in the white-circle regions, and 0.269 mm over the entire surface. Compared to measurement with no AFPP, 99.53% and 99.96% error reductions were achieved in the black and white-circle regions, respectively. Compared to measurement with the simplified AFPP, similar measurement accuracy was achieved in the black region, while an error reduction of 9.49% was achieved in the white-circle regions. This is because the adapted MIGLs ranging from 151 to 185 were higher than the MIGL 120 used in the simplified AFPP, generating greater intensity modulation and thus better associated measurement accuracy.

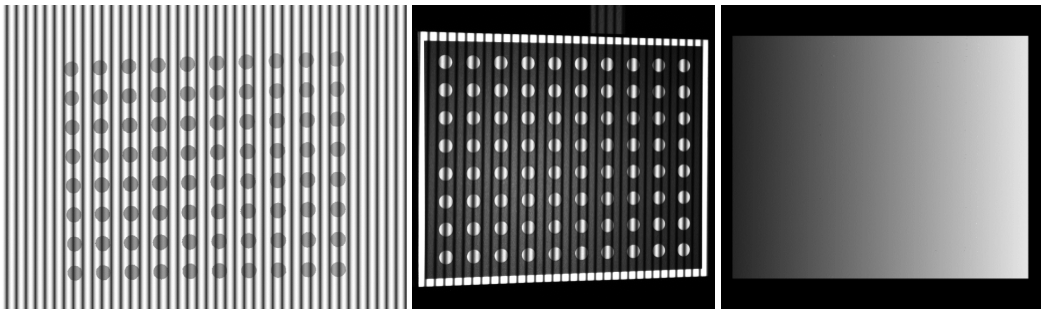

(a) (b) (c)

Figure 5-6 A single adapted vertical fringe pattern and corresponding captured image of the fringe pattern on the board using AFPP: (a) fringe pattern with adapted MIGLs, (b) captured image of the planar board with projection of the pattern in (a), (c) absolute phase map of the planar board from (b).

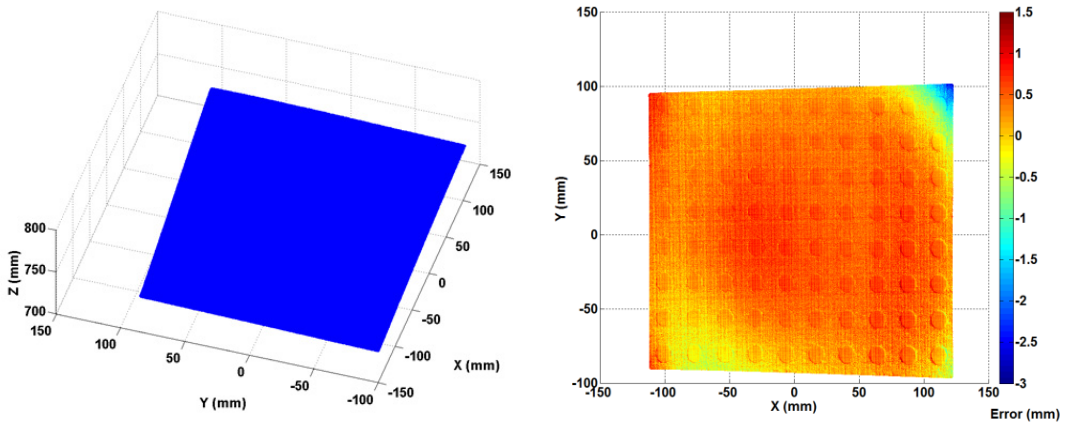

(a) (b)

Figure 5-7 Results of planar board measurement with AFPP: (a) 3D point cloud data of entire surface, (b) point cloud view of board showing measurement errors in colour for entire surface. Scales for Figure 5-7a to Figure 5-7b are the same as in Figure 5-5a to Figure 5-5b, Figure 5-4d to Figure 5-4e, and Figure 5-3a to Figure 5-3b, where the errors were low.

A comparison of the measurement accuracy using three methods, without AFPP, simplified AFPP, and AFPP is presented in Table 5-1. The AFPP method not only solves the problem of large measurement errors due to image saturation at highly-reflective white-circle regions, but also achieves the best measurement accuracy in the white-circle regions by employing locally adapted high intensity-modulation, thus handling the varying luminance across the surface due to projector-lighting and camera-viewing angles. The simplified AFPP uses a low MIGL value set globally across the pattern at previously saturated regions, and thus has reduced computation compared to the AFPP method. Since the AFPP adapts the MIGL locally and ensures the highest MIGL that avoids saturation in all regions, it would be better than the simplified AFPP, especially in handling variation in surface reflectivity or illumination across the surface.

The AFPP method of saturation avoidance adaptively adjusts the MIGL to the highest value that will not cause saturation for all previously saturated regions, and sets the MIGL to the highest possible value, 255, for all regions that do not saturate at this level. Both bright and dark regions are thus optimally handled.

Table 5-1 Comparison of Measurement Accuracy in Fringe-Pattern Projection Methods.

Methods	Root Mean Square Error (mm)		
	Black Region	White-Circle Regions	Entire Surface
Without AFPP (global MIGL 255)	0.287	558.277	14.035
Without AFPP (global MIGL 120)	58.275	0.260	52.235
Simplified AFPP	0.277	0.253	0.273
AFPP	0.276	0.229	0.269

5.2.2 Wooden Mask Measurement

Results of the fringe-pattern projection and image capture procedures in measuring the wooden mask using the AFPP method are shown in Figure 5-8. The wooden mask has both bright and dark colors across the surface (Figure 5-8a). The camera exposure time was set to have high intensity modulation at surface regions with dark color, resulting in image saturation at certain surface regions with bright color, as seen in Figure 5-8b. From a camera mask image, containing saturated-pixel clusters (Figure 5-8c), contours of saturated-pixel clusters are extracted, as shown in Figure 5-8d. The matching contours of saturated-pixel clusters are shown in a projector image (Figure 5-8e). A projector mask image with matching clusters is shown in Figure 5-8f. One of the adapted fringe patterns for 3D measurement is shown in Figure 5-8g. Using adapted MIGLs at matching clusters in Figure 5-8f to illuminate the corresponding saturated-pixel clusters in Figure 5-8c, image saturation can be avoided in the corresponding camera-captured image of the fringe pattern on the wooden mask, as seen in Figure 5-8h.

Figure 5-8 Fringe-pattern projection and camera-image capture in measurement of wooden mask using AFPP: (a) wooden-mask image, (b) camera-captured image of vertical fringe pattern on wooden mask showing saturation, (c) camera mask image with saturated-pixel clusters, (d) camera image contours of saturated-pixel clusters, (e) projector image matching contours corresponding to contours in (d), (f) projector mask image with matching clusters corresponding to saturated-pixel clusters in (c), (g) vertical fringe pattern with adapted MIGLs at matching projector-image clusters in (f), (h) camera-captured image of fringe pattern on wooden mask showing no saturation with projection of adapted MIGLs in (g).

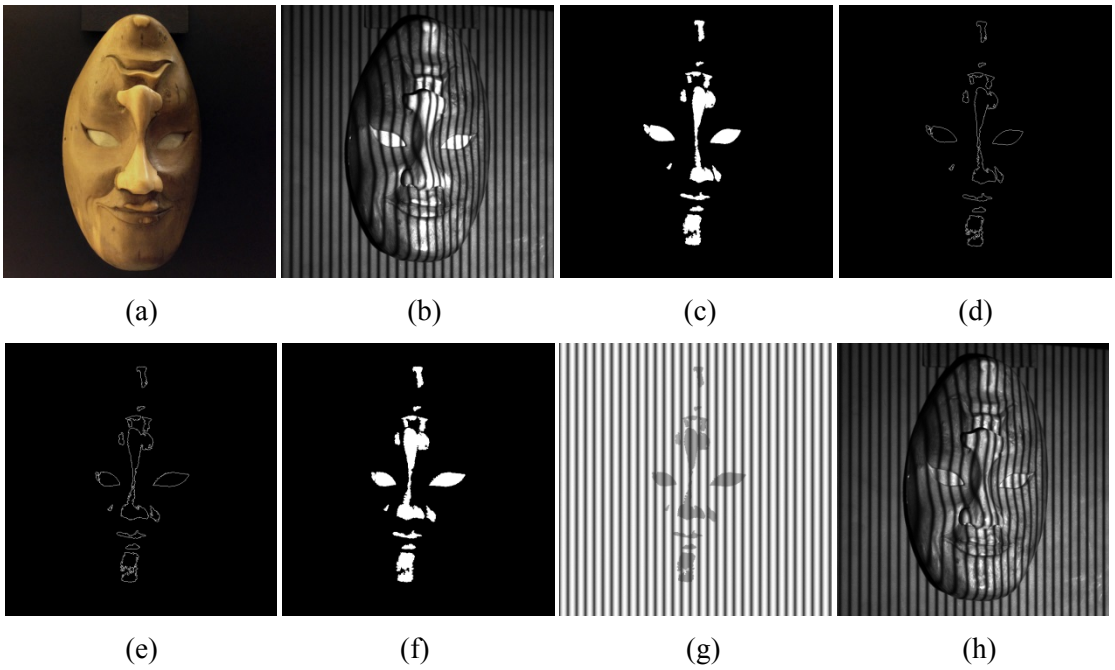

(a) (b) (c) (d)

(e) (f) (g) (h)

Results of the wooden mask measurements are also shown in Figure 5-9 as views of raw 3D point cloud data (Figure 5-9a to Figure 5-9d) and a range image showing depth (Z) values of all measured points (Figure 5-9e). No smoothing was applied for all figures. For global MIGL 255 (Figure 5-9a) holes are seen where large errors occurred due to image saturation occurred. With MIGL 255 at unsaturated regions and MIGL 120 at previously saturated regions (Figure 5-9b) and with MIGL 255 at unsaturated regions and adapted MIGLs by AFPP at previously saturated regions (Figure 5-9c), detailed surface geometry measurement is achieved without the large errors in regions that were previous saturated. The improvement in accuracy of 0.024 mm in the brighter regions with the AFPP method compared to the simplified AFPP method seen for the planar board in Figure 5-5b and Figure 5-7b, respectively, and Table 5-1, is not readily seen for the wooden mask displayed as a 3D cloud of points. However, absolute phase maps of the wooden mask in Figure 5-10a to Figure 5-10c show visible improvement from MIGL 255 to 120 to adapted MIGLs by AFPP, seen as decreased discontinuities in the phase maps.

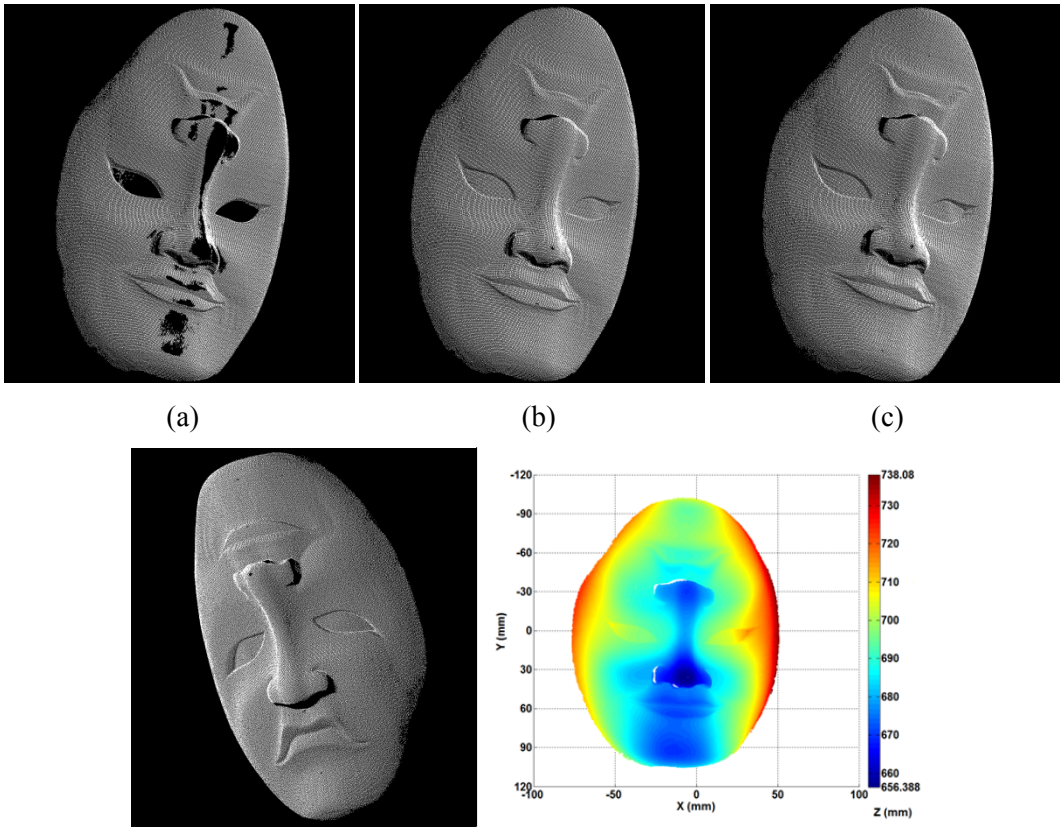

Figure 5-9 Results of the wooden mask measurement: view of raw 3D point cloud data: (a) with global MIGL 255, (b) with MIGL 255 at unsaturated regions and MIGL 120 at previously saturated regions (black holes) in (a), (c) with MIGL 255 at unsaturated regions and adapted MIGLs by AFPP at previously saturated regions in (a), (d) alternate view with AFPP, and (e) colour representation of the wooden mask range image showing depth (*Z*) values of all measured points with AFPP. (No smoothing was applied in all figures).

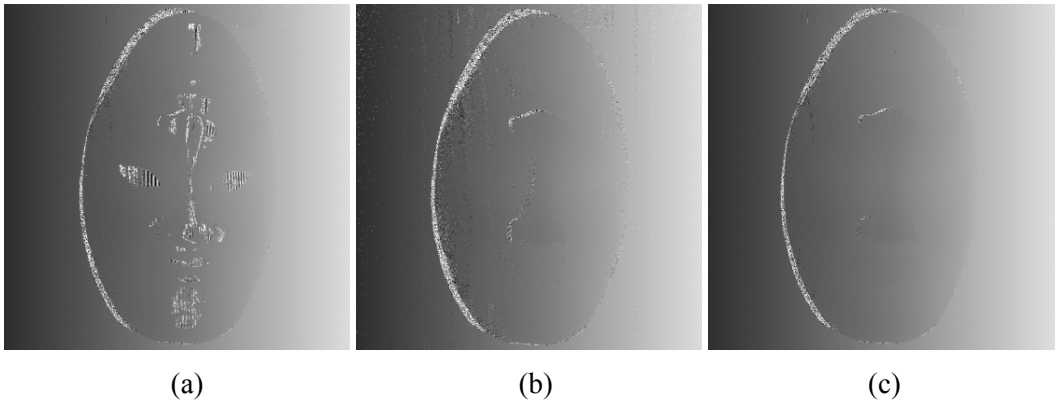

Figure 5-10 Absolute phase maps of the wooden mask: (a) for global MIGL 255, (b) for global MIGL 120, and (c) for AFPP adapted MIGLs.

5.3 Summary

A newly developed adaptive fringe pattern projection (AFPP) method adapts the projector maximum input gray levels (MIGLs) to local surface reflectivity to overcome the image saturation problem in fringe-projection 3D surface-shape measurement. By locally modifying the MIGLs in projected fringe patterns, highly-reflective surface regions can be illuminated with adaptively-lowered MIGLs to avoid image saturation, and surface regions with low reflectivity can be simultaneously illuminated with the highest MIGL to maintain high intensity modulation. Experiments verified that the AFPP method can attain higher 3D measurement accuracy across a surface with a large range in reflectivity than measurement without AFPP. Experiments also demonstrated that the AFPP local adaptation of projected fringe patterns was better than simpler adaptation using a single low MIGL for saturated regions. The AFPP method was able to handle varying luminance across the surface due to lighting and viewing angles in addition to surface reflectivity.

The AFPP method uses only two prior fringe-pattern projection and image-capture rounds to generate the adapted fringe patterns for 3D measurement, without the many fringe-pattern projection and image-capture sets used in previous high-dynamic-range 3D imaging methods [50-51, 53-55], and without the added complexity of multiple camera viewpoints, projection directions, and optical and control hardware in methods [44-45]. The AFPP method aimed to achieve saturation avoidance using minimal number of sets of phase shifted patterns. There was no attempt to optimize other aspects of the AFPP method. A variety of known techniques could be used to minimize computation such as use of many fewer points (projector input and camera-captured intensities) to determine equation coefficients, parallel processing, and GPU processing. Furthermore, methods to attain a linear projector-input to camera-captured intensity mapping can be employed to permit line fitting and linear extrapolation without requiring curve fitting. Improved gamma-correction methods and gamma-free projectors could also be used to eliminate curve fitting and thus allow fast computation of linear extrapolation of the projector-camera intensity mapping. These approaches are recommended for future research.

While the AFPP method has been demonstrated to be useful in avoiding image saturation, requiring fewer sets of projected patterns and acquired images than previous HDR techniques, treatment of saturation at a more local level than by saturated surface region could offer further improvement. In measuring the planar board with a grid of white solid circles on a black background, a single adapted MIGL for the entire cluster may be optimal for all saturated pixels of the cluster. However, the surface reflectivity and surface luminance may vary within a saturated cluster (a white-circle region), the latter due to projector-lighting and camera-viewing angles. For a large range in surface reflectivity and luminance within a saturated cluster, a single adapted MIGL may not be optimal for all the saturated pixels of the cluster. Ideally, the MIGL should be adapted at each pixel to account for the variable surface reflectivity. In the next chapter, an improved method that can achieve pixel-wise fringe-pattern adaptation to surface reflectivity and luminance is presented.

Chapter 6
Pixel-Wise Adaptive Fringe-Pattern Projection

This chapter presents a new pixel-wise adaptive fringe-pattern projection (PWAFPP) method that modifies the maximum input gray level (MIGL) pixel-by-pixel in the projected fringe patterns in order to attain high intensity modulation of captured fringe patterns across an image without saturation. The PWAFPP method preserves the advantage of the newly developed adaptive fringe-pattern projection (AFPP) method (detailed in Chapter 5): requiring only three sets of fringe-patterns to achieve image saturation avoidance. The PWAFPP method is an improvement over the AFPP method, as it is able to handle variable surface reflectivity within a saturated cluster.

6.1 Principles of Pixel-Wise Fringe-Pattern Adaptation to Surface Reflectivity

The PWAFPP method achieves image saturation avoidance using three rounds of fringe-pattern projection (as in the AFPP method) with 1) a high global MIGL (constant globally across all pixels of the entire pattern) to identify the saturated camera pixels and determine the corresponding projector pixels to modify, 2) a low global MIGL to determine the pixel-wise adaptation of MIGLs, and 3) pixel-wise adapted MIGLs to perform adaptive fringe-pattern projection for 3D surface-shape measurement, as detailed below.

1) Determination of saturated camera pixels and projector pixels to modify

Identification and clustering of saturated pixels is performed using a high global MIGL set to 255 in all fringe patterns. The camera exposure time is adjusted to ensure high intensity modulation of captured fringe patterns in dark image regions, regardless of image saturation occurring in bright image regions. For each camera pixel, if the captured intensity $I_{ijq}(x_c, y_c)$ from any fringe-pattern image (for any phase shift $i \in [1, N]$, fringe frequency $j \in [1, J]$, or fringe direction $q \in [1, Q]$) reaches 255, the pixel is identified as a saturated pixel. A camera mask image $M_C(x_c, y_c)$ is then generated by:

$$M_{\mathrm{C}}\left(x_{\mathrm{c}}, y_{\mathrm{c}}\right)=\begin{cases}255, & \text{for any } I_{ijq}\left(x_{\mathrm{c}}, y_{\mathrm{c}}\right)=255 \\ 0, & \text{otherwise}\end{cases}. \tag{6.1}$$

For each saturated pixel with camera coordinates $\left(x_{\mathrm{c}}, y_{\mathrm{c}}\right)$, the matching pixel projector coordinates $\left(x_{\mathrm{p}}, y_{\mathrm{p}}\right)$ can be computed by:

$$\begin{cases}x_{\mathrm{p}}=T\times\phi_{\mathrm{V}}\left(x_{\mathrm{c}}, y_{\mathrm{c}}\right)/2\pi \\ y_{\mathrm{p}}=T\times\phi_{\mathrm{H}}\left(x_{\mathrm{c}}, y_{\mathrm{c}}\right)/2\pi\end{cases}, \tag{6.2}$$

where absolute phase maps $\phi_{\mathrm{V}}(x_{\mathrm{c}}, y_{\mathrm{c}})$ and $\phi_{\mathrm{H}}(x_{\mathrm{c}}, y_{\mathrm{c}})$ are computed from vertical and horizontal fringe patterns, respectively, and T is the projected fringe period. As done for the camera, a projector mask image $M_{\mathrm{P}}\left(x_{\mathrm{p}}, y_{\mathrm{p}}\right)$ can be generated to include all matching saturated pixels labeled 255, and the remaining pixels labeled 0 (unsaturated). The matching saturated pixels in the projector mask thus indicate where MIGLs should be adapted in all fringe patterns, to specially illuminate surface regions that lead to image saturation when a high global MIGL is used.

2) Round Two: Determination of pixel-wise MIGL adaptation required

The adapted MIGLs are determined using a low global MIGL set to 120 in all fringe patterns. The low global MIGL 120 is an approximate median value over the projector input gray level range and was selected to be sufficiently low to ensure that saturation does not occur at any of the K saturated pixels in the camera mask image determined in Round One. Too high a MIGL value in Round Two would cause some pixels to be saturated in Round Two, and one or more additional rounds would be required to obtain phase values at those remaining saturated pixels.

For the kth $(k=1,2,...,K)$ saturated pixel, the matching projector coordinates $(x_{\mathrm{p}}, y_{\mathrm{p}})$ corresponding to the camera coordinates $(x_{\mathrm{c}}, y_{\mathrm{c}})$ are determined using Equation 6.2 from two absolute phase maps $\phi_{\mathrm{V}}(x_{\mathrm{c}}, y_{\mathrm{c}})$ and $\phi_{\mathrm{H}}(x_{\mathrm{c}}, y_{\mathrm{c}})$ newly computed from the vertical and horizontal fringe patterns, respectively, using the low global MIGL. To determine the

relationship of camera-captured intensities to projector-input intensities for each saturated pixel, the captured intensities $I_{ijq}(x_c, y_c)$ at saturated camera pixel (x_c, y_c) wherever $M_C(x_c, y_c) = 255$, are mapped to their corresponding input intensities $I_{ijq}(x_p, y_p)$ at projector pixel (x_p, y_p), wherever $M_P(x_p, y_p) = 255$ by:

$$I_{ijq}(x_p, y_p) = a_{1,k} \times I_{ijq}^{a_{2,k}}(x_c, y_c) + a_{3,k}, \tag{6.3}$$

where $a_{1,k}, a_{2,k}, a_{3,k}$ are the coefficients that define the intensity mapping for the kth saturated pixel and need to be determined. The coefficients $a_{1,k}, a_{2,k}, a_{3,k}$ are determined for the kth saturated pixel through weighted nonlinear least-squares regression, which iteratively optimizes the three coefficients using the Levenberg-Marquardt algorithm:

$$\arg\min_{\{a_{1,k}, a_{2,k}, a_{3,k}\}} \left\{ \sum_{i\in[1,N], j\in[1,J], q\in[1,Q]} \left[\left[a_{1,k}^{-1} \times \left(I_{ijq,k}(x_p, y_p) - a_{3,k} \right) \right]^{1/a_{2,k}} - I_{ijq,k}(x_c, y_c) \right]^2 \right\}. \tag{6.4}$$

The MIGL that maintains the largest intensity modulation without image saturation for the kth saturated pixel is thus determined by:

$$I_{\text{Max},k} = a_{1,k} \times 254^{a_{2,k}} + a_{3,k}. \tag{6.5}$$

Adapted MIGLs $I_{\text{Max},k}$ ($k = 1, 2, ..., K$) can thus be obtained to account for all saturated pixels.

In Round Two, the determination of coefficients by Equation 6.4 essentially fits a curve to map camera-captured intensities to projector-input intensities in order to estimate the best adapted MIGL corresponding to camera-captured intensity 254 by Equation 6.5. Too low a MIGL value in Round Two would cause intensity values to be distributed lower on the curve (farther from 254) and could result in a poorer estimated MIGL corresponding to camera intensity 254.

4) Round Three: Adaptive fringe-pattern projection

Adapted phase-shifted fringe patterns for 3D surface-shape measurement are generated by using the high MIGL 255 (employed in Round One) at projector pixels wherever

$M_{\mathrm{P}}\left(x_{\mathrm{p}}, y_{\mathrm{p}}\right)=0$, and the adapted MIGLs $I_{\mathrm{Max},k}\,(k=1,2,...,K)$ at projector pixels wherever $M_{\mathrm{P}}\left(x_{\mathrm{p}}, y_{\mathrm{p}}\right)=255$. Note that if a MIGL value lower than 255 were used in Round One, the system would not be able to detect at which pixels saturation would occur, when MIGL is later set to 255 in Round Three for all pixels that did not saturate in Round One.

Instead of a single adapted MIGL used at all pixels of a saturated cluster in the AFPP method (Chapter 5), the PWAFPP method feeds each and every saturated pixel with a MIGL specifically adapted to the particular surface reflectivity and illuminance of the surface point that corresponds to that particular saturated pixel. The method thus improves the AFPP method by using multiple adapted MIGLs, instead of one, to account for the variable surface reflectivity and illuminance that occurs across different pixels of a saturated cluster.

6.2 Experiments and Results

The PWAFPP and AFPP methods were compared in measuring two types of planar boards both with a large range in surface reflectivity: 1) a planar board with a white-solid-circle grid on black, as shown in Figure 6-1a, and 2) a planar board with stepped gray levels: ten gray-scale steps, nine from gray level 0 to 240 in increments of 30, left to right, and additionally, a right-most gray level of 255, as shown in Figure 6-1b. The two planar boards were measured with high global MIGL 255, low global MIGL 120, AFPP, and PWAFPP, respectively. For simple referencing purposes hereinafter, the two planar boards are referred to as Board One for the white-solid-circle grid on black, and Board Two for the stepped gray levels.

For all tests, the measurement system used a monochrome 1024×1024 8-bit CCD camera and a 1024×768 8-bit digital-light-processing (DLP) projector. The four-step phase-shifting algorithm was used for phase computation. Three frequencies corresponding to periods 24, 26, and 28, were used for phase unwrapping.

Figure 6-1 Two planar boards with large range in surface reflectivity: (a) Board One: white-solid-circle grid on black, (b) Board Two: stepped gray levels (gray levels 0 to 240 in increments of 30 and additionally 255).

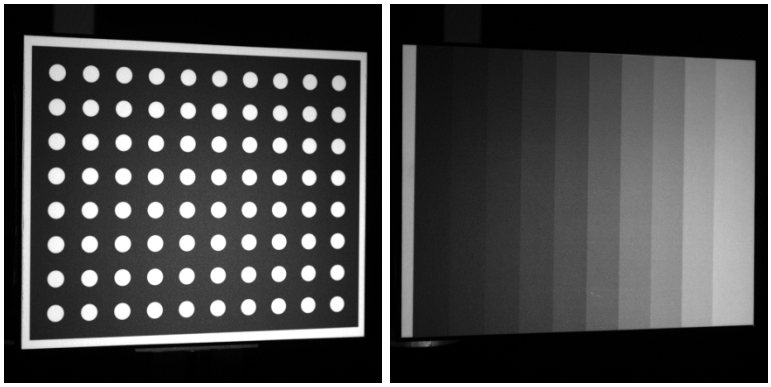

(a) (b)

6.2.1 Measurement of Planar Board with White-Solid-Circle Grid on Black

The results of tests with the four methods using Board One (white-solid-circle grid) are shown in rows 1 to 4 of Figure 6-2 for: (a-c) high global MIGL 255, (d-f) low global MIGL 120, (g-i) AFPP, and (j-l) PWAFPP, respectively. For all tests (rows), one of the vertical fringe patterns for the test is in column 1, the corresponding captured fringe-pattern image in column 2, and an absolute phase map in column 3. With the high global MIGL 255 (Figure 6-2a), image saturation occurred in the white regions in Figure 6-2b, resulting in errors seen as discontinuities in the absolute phase map in Figure 6-2c. With the low global MIGL 120 (Figure 6-2d), intensity modulation of the captured fringe pattern was very low in the black region, as seen in Figure 6-2e, with resulting errors slightly visible as discontinuities in the absolute phase map in Figure 6-2f. With locally adapted MIGLs in Figure 6-2g and pixel-wise adapted MIGLs in Figure 6-2j, large intensity modulation without image saturation was achieved in both black and white regions, as seen in Figure 6-2h and Figure 6-2k. The resulting absolute phase maps (Figure 6-2i and Figure 6-2l) thus have no apparent discontinuity or visible error.

Figure 6-2 Sample projected fringe pattern and captured and processed images for Board One for measurements using different fringe-pattern projection techniques. By rows: (a-c) high global MIGL 255, (d-f) low global MIGL 120, (g-i) AFPP, and (j-l) PWAFPP. By columns: (a, d, g, j) vertical fringe pattern, (b, e, h, k) captured image of planar board with projection of pattern in column 1, (c, f, i, l) absolute phase map of planar board from column 2.

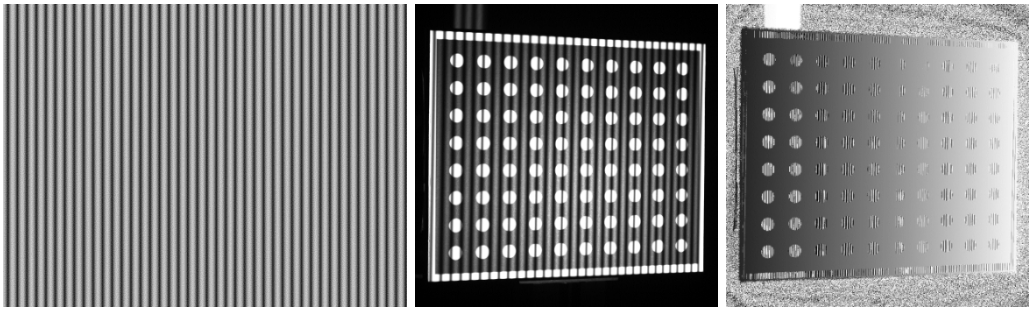

(a) (b) (c)

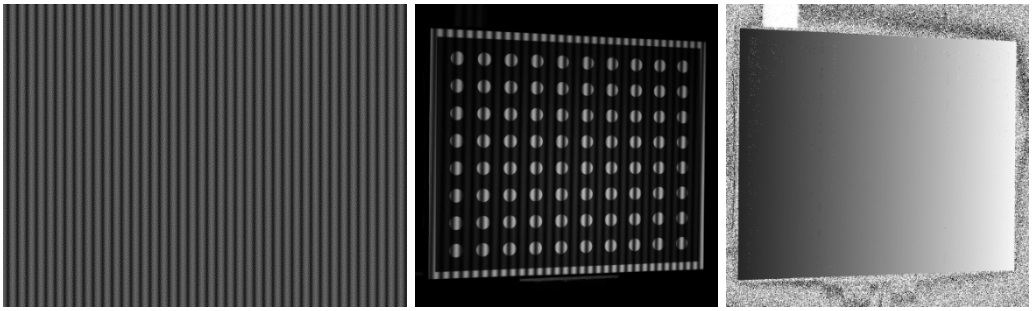

(d) (e) (f)

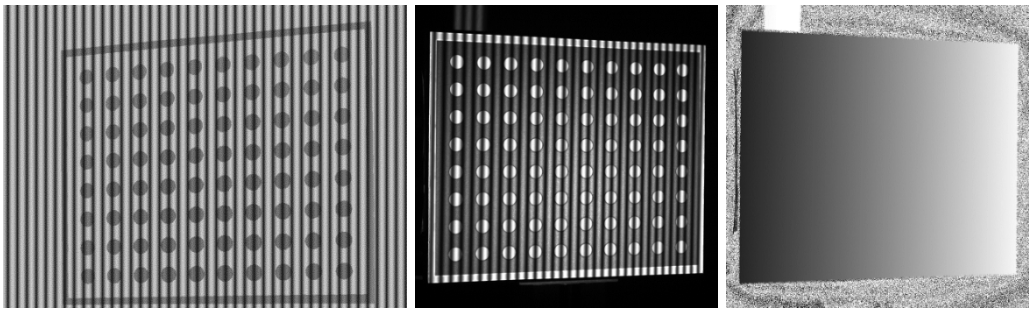

(g) (h) (i)

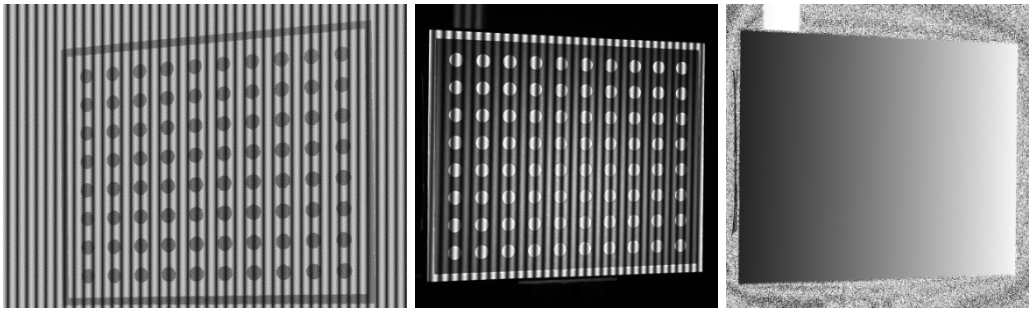

(j) (k) (l)

Table 6-1 Comparison of accuracies of Board One (white-solid-circle grid) measurements using different fringe-pattern projection methods.

	Root Mean Square Error (mm)		
Methods	Black Region	White Regions	Entire Surface
High global MIGL 255	0.123	1389.870	724.745
Low global MIGL 120	32.963	0.201	28.128
AFPP	0.121	0.193	0.157
PWFPA	0.118	0.195	0.150

Results of the Board One planar board measurement using different fringe-pattern projection techniques are presented in Table 6-1. With the high global MIGL 255, the much larger error in the white regions, RMS error (RMSE) 1389.870 mm compared to 0.123 mm in the black region was due to image saturation that occurred in the white regions (Figure 6-2b). With the low global MIGL 120, the larger measurement error in the black region 32.963 mm compared to 0.201 mm in the white regions was due to the low intensity modulation in the black region (Figure 6-2e), although the error was not as large as the errors due to image saturation with MIGL 255.

With locally adapted MIGLs in the AFPP method, the RMSE was 0.121 mm in the black region, 0.193 mm in the white regions, and 0.157 mm over the entire surface. The AFPP method simultaneously achieved 99.99% error reduction in the white regions compared to measurement with global MIGL 255, and 99.63% error reduction in the black regions compared to measurement with global MIGL 120. The measurement results of the first three tests (high global MIGL 255, low global MIGL 120, and AFPP) are consistent with the results in Section 5.2.1, for which the advantages of the AFPP method over no MIGL adaptation to surface reflectivity have been explained in detail.

With pixel-wise adapted MIGLs in the PWAFPP method, the RMS error was 0.118 mm in the black region, 0.195 mm in the white regions, and 0.150 mm over the entire surface. Compared to measurements with global MIGLs 255 and 120, 99.99% and 99.64% error reductions were achieved in the white and black regions, respectively. The measurement

results of the AFPP and PWAFPP methods are quite similar (last two rows in Table 6-1). The two methods perform similarly on Board One, where there may be only slight variation in surface reflectivity and illuminance across pixels of a white solid circle.

For a surface with more gray levels than the black and white used on Board One, there will be greater variation in intensity within a captured image region corresponding to a bright surface region, compared to the small intensity variation within a saturated cluster for which the AFPP method was designed. The single adapted MIGL value used at all pixels within a cluster by the AFPP method will fail to account for intensity variation within the cluster. The PWAFPP method, however, estimates a MIGL specifically adapted to each pixel according to the particular reflectivity and illuminance at the surface point corresponding to that particular pixel, and would thus be able to handle the intensity variation within a saturated region or cluster. To this end, Board Two with stepped gray levels between 0 (black) and 255 (white) were measured to demonstrate the advantage of the PWAFPP method over the AFPP method in handling greater intensity variation.

6.2.2 Measurement of Planar Board with Stepped Gray Levels

The results of tests with the four methods using Board Two (stepped gray levels) are shown in rows 1 to 4 of Figure 6-3, for: (a-c) high global MIGL 255, (d-f) low global MIGL 120, (g-i) AFPP, and (j-l) PWAFPP, respectively. For all tests (rows), one of the vertical fringe patterns for the test is in column 1, the corresponding captured fringe-pattern image in column 2, and an absolute phase map in column 3. With the high global MIGL 255 in Figure6-3a, image saturation occurred in the region with high gray-level (right side) in Figure 6-3b, resulting in errors seen as discontinuities in the absolute phase map in Figure 6-3c. With the low global MIGL 120 in Figure 6-3d, intensity modulation of the captured fringe pattern was very low in the region with darker gray-level (left side), as seen in Figure 6-3e, with resulting errors slightly visible (top left corner) as discontinuities in the absolute phase map in Figure 6-3f.

Using the AFPP method, the saturated clusters were determined in captured fringe-pattern images in the first round of fringe-pattern projection and image capture. For Board Two,

there are only two saturated clusters over the entire surface, as shown in Figure 6-4a. In Figure 6-1b, at the surface region that corresponds to the saturated cluster on the right side, the surface gray level is not uniform. In AFPP, only a single adapted MIGL was used at all pixels of the matching cluster in Figure 6-4b. With this single adapted MIGL value for the entire right cluster in the adapted fringe pattern projected in Figure 6-3g, image saturation can be avoided at the left half of the right cluster in Figure 6-3h. However, some pixels of the left half, particularly ones near the border of the saturated and unsaturated regions, appear darker. This demonstrates that the single adapted MIGL cannot generate the largest possible intensity modulation at those pixels. Additionally, image saturation still occurs at some pixels of the right half of the cluster. Thus, for the stepped gray levels of Board Two, the AFPP method, which generates a single adapted MIGL value for a cluster, cannot generate a sufficiently high uniform intensity modulation without saturation for the cluster as it could in measuring Board One (Figure 6-2h).

The varying pixel-wise adapted MIGLs (increasing in gray level from right to left) in Figure 6-3j by the PWAFPP method reflects how those adapted MIGLs account for the varying surface reflectivity within the cluster (of the AFPP method): brighter surface regions (pixel size) illuminated by lower MIGLs, darker surface regions (pixel size) illuminated by higher MIGLs. Unlike the captured fringe-pattern image (Figure 6-3h) by the AFPP method, uniformly large intensity modulation without saturation can be achieved for the cluster (of the AFPP method) on the right side of the cluster, as seen in Figure 6-3k. The resulting absolute phase map (Figure 6-3l) has no apparent discontinuity or visible error. The PWAFPP method would therefore be an improvement over the AFPP method in handling the variable surface reflectivity that can occur within a saturated cluster (of the AFPP method), by more locally adapting the MIGL pixel-by-pixel, as demonstrated below.

Figure 6-3 Sample projected fringe pattern and captured and processed images for Board Two for measurements using different fringe-pattern projection techniques. By rows: (a-c) high global MIGL 255, (d-f) low global MIGL 120, (g-i) AFPP, and (j-l) PWAFPP. By columns: (a, d, g, j) vertical fringe pattern, (b, e, h, k) captured image of planar board with projection of pattern in column 1, (c, f, i, l) absolute phase map of planar board from column 2.

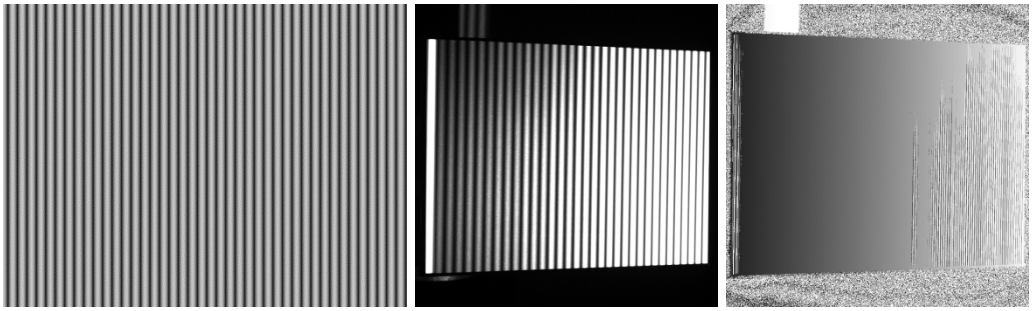

(a) (b) (c)

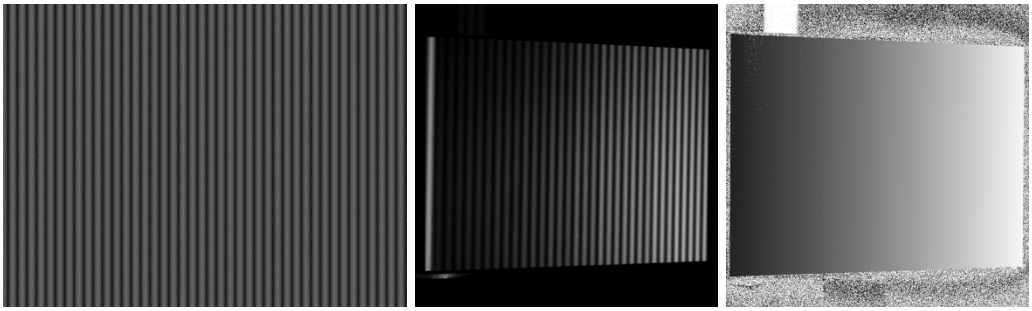

(d) (e) (f)

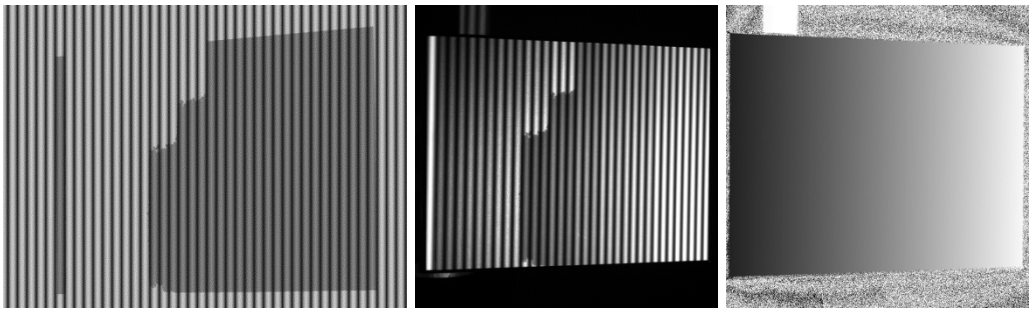

(g) (h) (i)

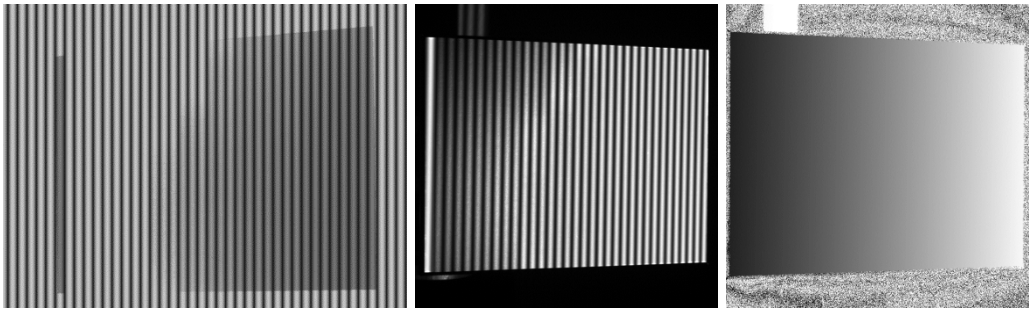

(j) (k) (l)

(a) (b)

Figure 6-4 AFPP saturated clusters with Board Two: (a) Camera mask image with saturated-pixel clusters, (b) projector mask image with matching clusters corresponding to saturated-pixel clusters in (a).

Table 6-2 Comparison of accuracies in Board Two (stepped gray levels) measurements using different fringe-pattern projection methods.

	Root Mean Square Error (mm)		
Methods	Non-Saturated Region	Saturated Regions	Entire Surface
High global MIGL 255	0.118	384.498	303.087
Low global MIGL 120	38.996	0.159	24.017
AFPP	0.115	0.154	0.161
PWFPA	0.113	0.150	0.158

Results of Board Two (stepped gray levels) measurement using different fringe-pattern projection techniques are presented in Table 6-2. With the high global MIGL 255, the RMS error was 0.118 mm in the non-saturated region, 384.498 mm in the saturated regions, and 303.087 mm over the entire surface, respectively. With the low global MIGL 120, the RMS error was 38.996 mm in the non-saturated region, 0.159 mm in the saturated regions, and 24.017 mm over the entire surface, respectively.

With locally adapted MIGLs in the AFPP method, the RMS error was 0.115 mm in the non-saturated region, 0.154 mm in the saturated regions, and 0.161 mm over the entire surface. Compared to measurements with global MIGLs 120 and 255, 99.71% and 99.96% error reductions were achieved in the saturated and non-saturated regions, respectively.

With pixel-wise adapted MIGLs in the PWAFPP method, the RMS error was 0.113 mm in the non-saturated region, 0.150 mm in the saturated regions, and 0.158 mm over the entire surface. Compared to measurements with global MIGLs 120 and 255, 99.71% and 99.96% error reductions were achieved in the non-saturated and saturated regions, respectively. The AFPP and PWAFPP methods are better than methods that use global MIGLs in terms of measurement accuracy.

Again, the measurement accuracies by the AFPP and PWAFPP methods are similar (last two rows in Table 6-2). This result is not expected because the PWAFPP would be expected to be better than AFPP in handling a large variation in surface reflectivity in a single saturated region on Board Two. One possible reason for the unexpected result is that the improvement in measurement accuracy by PWAFPP may occur, but it may not be detectable in the RMS error. The RMS error relates to the measurement errors over the entire surface measured. The number of pixels not handled by the AFPP was small compared to the total number of pixels of the entire board.

To explore this, the RMS error was recalculated only at pixels that remained saturated by AFPP (seen in Figure 6-3h), i.e. at pixels that the AFPP could not handle. The corresponding results are presented in Table 6-3. Compared to AFPP, 34% error reduction was achieved using the PWAFPP method for pixels that remained saturated after applying the AFPP method.

Table 6-3 Comparison of measurement accuracy between AFPP and PWAFPP methods at pixels that remained saturated after implementation of AFPP method for Board Two (stepped gray levels).

Methods	AFPP	PWAFPP
RMS error (mm)	0.091	0.060

6.3 Summary

A pixel-wise adaptive fringe pattern projection (PWAFPP) method was developed to project a maximum input gray level (MIGL) specifically adapted to each pixel according to the particular reflectivity and illuminance at the surface point corresponding to that particular

pixel. Comparing the AFPP and PWAFPP, instead of using only a single adapted MIGL value for all pixels within a saturated cluster as in the AFPP method, the PWAFPP method employs a MIGL specifically adapted for each pixel to account for the non-uniform reflectivity and illuminance within a bright surface region that corresponds to a saturated cluster (of the AFPP method). Experiments demonstrated that the PWAFPP method preserves all the advantages of the AFPP method over measurement with a global MIGL. Experiments also demonstrated that the PWAFPP method can improve the measurement accuracy of measured 3D points suffering from residual image saturation after implementation of AFPP. The PWAFPP method can thus be used to measure surfaces with more complex variation in surface reflectivity.

Chapter 7
Compactness of Fringe-Projection 3D Measurement Systems

In this chapter, analyses of the effect of camera-projector system geometry (relative camera-projector position and angle), which determines the compactness of a camera-projector measurement system, on 3D shape measurement accuracy is presented. The analysis would enable better selection of geometric parameters to employ when designing a compact 3D scanner to have a specified measurement accuracy. Two studies were performed, for industrial and consumer 3D measurement systems, respectively.

7.1 System Configuration for Compactness Study of Industrial System

The system geometry for the compactness study of the industrial system is illustrated in Figure 7-1a. The camera-projector angle is the angle between the camera and projector optical axes. The baseline is the straight line distance (not shown) between the camera optical centre Oc and the projector optical centre Op. The centres of the fields of view of the camera and projector intersect at a point P on an object surface. The camera-projector angles at which the measurement accuracy was tested are from 5° to 35° with 2.5° intervals.

The camera position and the viewing direction were fixed while the projector was moved to 13 different positions to achieve the 13 different camera-projector angles. The camera optical centre Oc and the projector optical centre Op were positioned on the same arc (with centre P and radius equal to the working distance). Working distances of the camera and projector could thus be kept identical and constant during the entire test.

At each camera-projector angle, the orientation of an object surface was positioned perpendicular to a unique baseline determined by the camera-projector angle. Because the camera position and camera optical axis were fixed, the projector optical axis required adjustment each time the projector position was changed, in order to ensure that the centres of fields-of-view of the camera and projector always intersect at the same point P. The 13 black bold solid lines indicate 13 directions (object-surface orientations) perpendicular to 13 baselines that correspond to the 13 camera-projector angles. The 14 black dashed lines

between the two arcs indicate: (1) camera-viewing direction (the left-most one), and (2) 13 corresponding projector-illuminating directions. In Figure 7-1a, two baselines (two yellow solid lines), two projector-illuminating directions (optical axes), and two projector positions that correspond to the narrowest and widest camera-projector angles, are labelled.

Figure 7-1b illustrates the real system that corresponds to the squared region of the CAD drawing in Figure 7-1a. The squared region was printed with 1:1 scale. The printed paper was attached to an aluminum plate to align the measurement object relative to the 3D scanner during experiments (detailed in the following sections). The holes on the aluminum plate for mounting the camera and projector were made according to the positions of the optical centres of the camera and projector in the CAD drawing, ensuring that the camera and projector always have the same stand-off distance to the object, as designed in the CAD drawing.

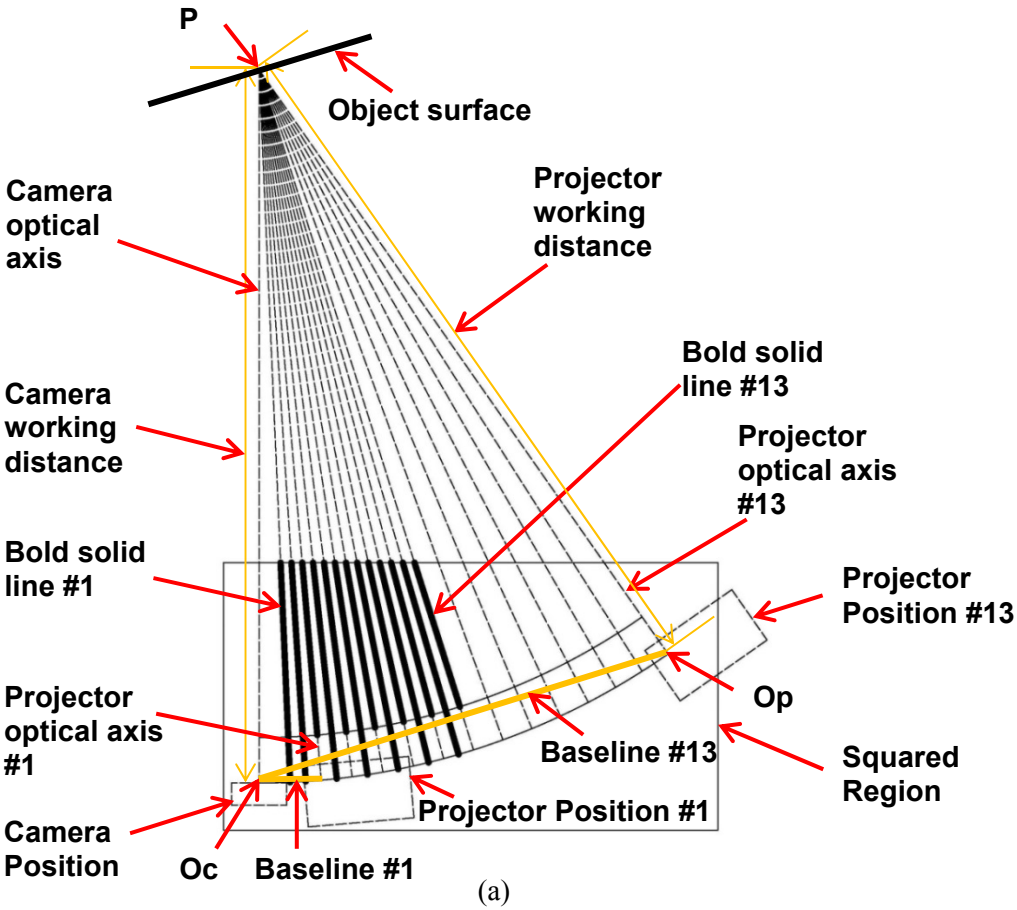

(a)

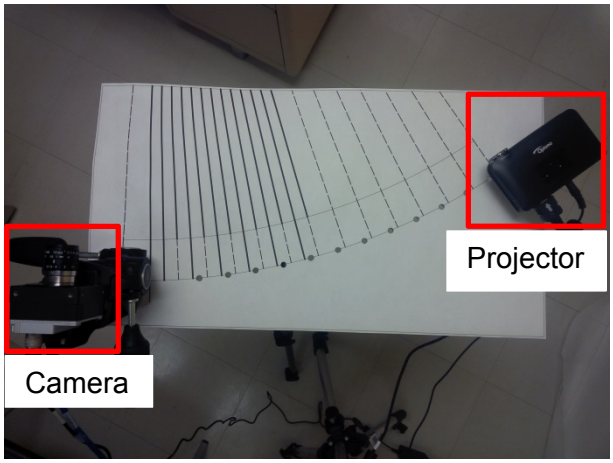

(b)

Figure 7-1 System configuration for compactness study of industrial system: (a) CAD drawing of system geometry, (b) real system corresponding to squared region in (a).

A monochrome GigE camera (Basler avA1000-100gm with 1024 × 1024 resolution and 8 bit depth) and a pico projector (Optoma PK 301 with 1024 × 768 resolution and 8 bit depth) were used. The vertical and horizontal field of view (FOV) angles of the camera were both 28°. The horizontal and vertical FOV angles of the projector were 31° and 16.3°, respectively. The FOV angles of the camera and projector enable measurement of surfaces with dimensions up to 399 mm × 229 mm at a working distance of 800 mm.

7.2 Experiments and Results with Industrial System

7.2.1 Flat Plate Measurement

A flat jig plate mounted on a micrometer translation stage (shown in Figure 7-2a) was measured using the 13 known camera-projector angles. At each angle, the plate was aligned with the 3D scanner such that the plate was parallel to the baseline (between camera and projector). To achieve this, the translation stage (with perpendicularly mounted plate) and inclined white line (shown in Figure 7-2b), attached to the translation stage, were aligned with the appropriate bold solid line (Figure 7-1), which was perpendicular to the corresponding baseline. The alignment was performed by adjusting the orientation of the plate until a laser line, projected by the laser projector shown in Figure 7-2c, was simultaneously coincident with the appropriate bold solid line (perpendicular to the baseline)

and the white line (Figure 7-2b) (perpendicular to the plate), as shown in Figure 7-2d. The plate was positioned using the micrometer to 11 known positions (0 mm to 50 mm with 5 mm intervals) towards the sensor during the experiment. At each position, the plate was measured, and RMSE and plane fitting error SD computed from raw 3D data to assess the measurement accuracy.

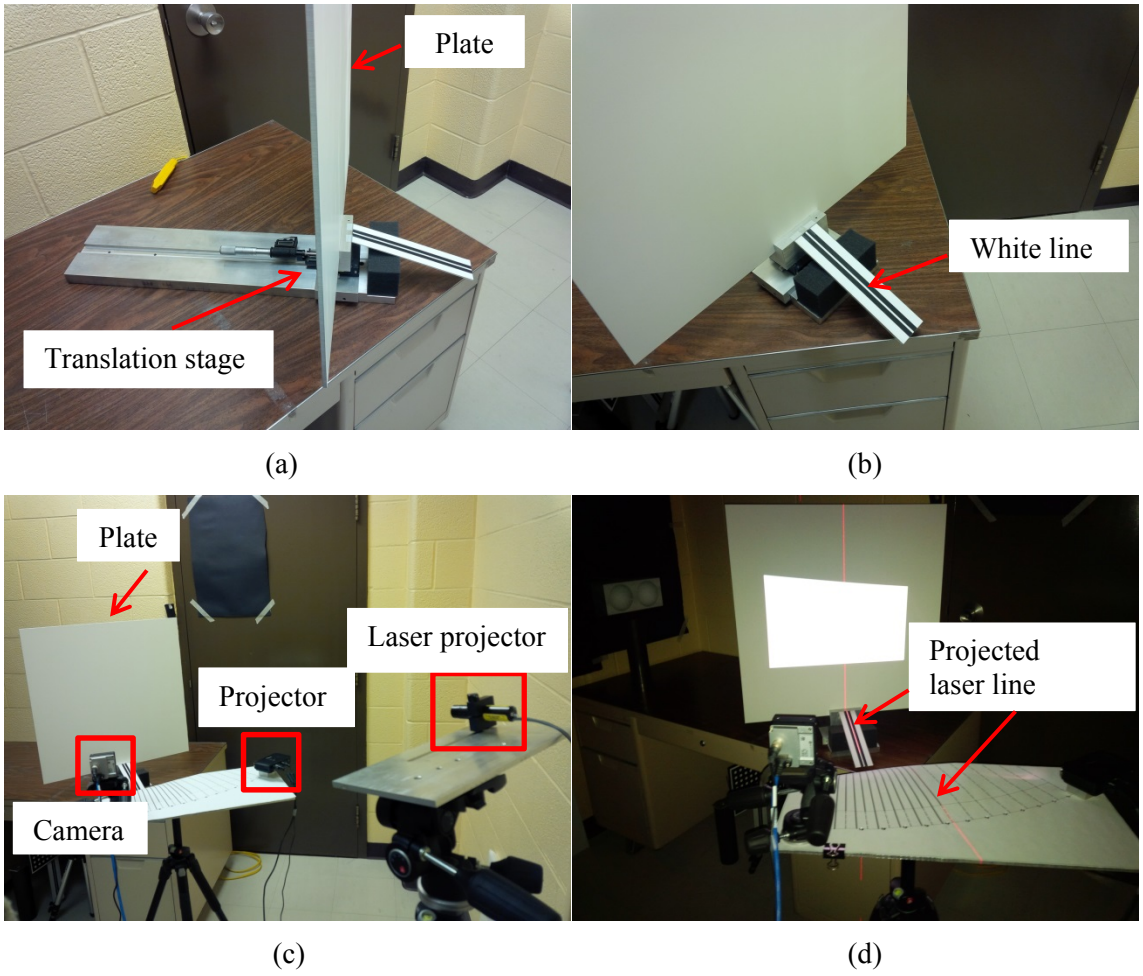

Figure 7-2 System configuration for plate measurement at different known camera-projector angles: (a) translation stage on which flat plate was mounted and moved to known positions; (b) white line aligned with translation stage; (c) laser projector used for alignment; (d) completed alignment with projected laser light simultaneously coincident with a bold solid line in Figure 7-1b and white line in (b).

The plane fitting error SDs and RMSEs of measuring the plate at 11 known plate positions and 13 known camera-projector angles, with CP and CPE techniques, respectively, are presented in Table 7-1 to Table 7-4.

Table 7-1 Plane fitting error SDs of measuring plate at 11 known positions and 13 known camera-projector angles with CP technique.

Position (mm) / Angle	0	5	10	15	20	25	30	35	40	45	50
	Plane Fitting Error SD (mm)										
5°	0.336	0.341	0.343	0.346	0.348	0.351	0.354	0.357	0.360	0.363	0.366
7.5°	0.238	0.239	0.241	0.241	0.242	0.244	0.246	0.247	0.249	0.251	0.253
10°	0.194	0.195	0.195	0.196	0.197	0.198	0.199	0.200	0.203	0.205	0.205
12.5°	0.156	0.156	0.156	0.156	0.157	0.157	0.158	0.159	0.161	0.163	0.163
15°	0.129	0.128	0.129	0.129	0.129	0.130	0.130	0.130	0.132	0.133	0.134
17.5°	0.114	0.114	0.114	0.114	0.115	0.115	0.115	0.116	0.118	0.119	0.120
20°	0.103	0.101	0.101	0.100	0.101	0.101	0.101	0.101	0.102	0.103	0.104
22.5°	0.093	0.093	0.092	0.092	0.092	0.092	0.092	0.093	0.094	0.095	0.096
25°	0.087	0.086	0.085	0.085	0.086	0.086	0.086	0.087	0.088	0.089	0.091
27.5°	0.078	0.077	0.077	0.076	0.076	0.076	0.076	0.076	0.077	0.078	0.078
30°	0.073	0.073	0.072	0.071	0.071	0.071	0.072	0.071	0.072	0.073	0.074
32.5°	0.076	0.075	0.074	0.073	0.072	0.072	0.071	0.071	0.072	0.072	0.073
35°	0.074	0.073	0.071	0.070	0.069	0.069	0.068	0.068	0.069	0.069	0.071

Table 7-2 Plane fitting error SDs of measuring plate at 11 known positions and 13 known camera-projector angles with CPE technique.

Position (mm) / Angle	0	5	10	15	20	25	30	35	40	45	50
	Plane Fitting Error SD (mm)										
5°	1.098	1.084	1.072	1.061	1.051	1.040	1.029	1.016	1.007	0.993	0.983
7.5°	0.709	0.699	0.690	0.680	0.672	0.663	0.653	0.647	0.639	0.629	0.621
10°	0.478	0.472	0.465	0.458	0.450	0.444	0.438	0.430	0.424	0.418	0.413
12.5°	0.372	0.367	0.361	0.355	0.349	0.343	0.337	0.331	0.327	0.322	0.316
15°	0.292	0.288	0.283	0.279	0.273	0.269	0.264	0.259	0.256	0.251	0.246
17.5°	0.239	0.234	0.231	0.226	0.222	0.217	0.213	0.208	0.206	0.202	0.198
20°	0.205	0.200	0.196	0.192	0.188	0.184	0.181	0.177	0.174	0.171	0.167
22.5°	0.177	0.173	0.169	0.165	0.162	0.159	0.155	0.152	0.150	0.147	0.144
25°	0.150	0.146	0.143	0.139	0.137	0.134	0.130	0.128	0.125	0.123	0.122
27.5°	0.135	0.131	0.128	0.124	0.122	0.120	0.117	0.114	0.112	0.109	0.107
30°	0.122	0.119	0.115	0.112	0.109	0.107	0.105	0.102	0.100	0.097	0.096
32.5°	0.124	0.120	0.117	0.114	0.111	0.108	0.105	0.103	0.100	0.098	0.097
35°	0.116	0.112	0.109	0.105	0.103	0.100	0.097	0.095	0.093	0.091	0.090

Table 7-3 RMSEs of measuring plate at 11 known positions and 13 known camera-projector angles with CP technique.

Position (mm) / Angle	0	5	10	15	20	25	30	35	40	45	50
	RMSE(mm)										
5°	0.338	0.342	0.348	0.362	0.348	0.351	0.354	0.358	0.364	0.369	0.396
7.5°	0.280	0.291	0.179	0.275	0.254	0.244	0.257	0.247	0.249	0.253	0.256
10°	0.196	0.196	0.202	0.197	0.203	0.198	0.206	0.206	0.219	0.228	0.226
12.5°	0.157	0.157	0.157	0.162	0.163	0.157	0.162	0.169	0.174	0.179	0.182
15°	0.130	0.130	0.131	0.132	0.129	0.130	0.130	0.133	0.137	0.140	0.148
17.5°	0.119	0.138	0.133	0.122	0.118	0.115	0.116	0.121	0.127	0.134	0.144
20°	0.111	0.119	0.110	0.107	0.104	0.101	0.104	0.112	0.119	0.119	0.126
22.5°	0.099	0.106	0.099	0.094	0.093	0.092	0.092	0.095	0.094	0.100	0.105
25°	0.093	0.104	0.103	0.094	0.090	0.086	0.087	0.092	0.098	0.111	0.118
27.5°	0.083	0.081	0.083	0.077	0.076	0.076	0.080	0.089	0.094	0.097	0.104
30°	0.082	0.079	0.082	0.075	0.073	0.071	0.075	0.074	0.082	0.091	0.094
32.5°	0.093	0.093	0.083	0.077	0.073	0.072	0.072	0.079	0.080	0.085	0.094
35°	0.078	0.076	0.075	0.070	0.071	0.069	0.073	0.076	0.083	0.086	0.092

Table 7-4 RMSEs of measuring plate at 11 known positions and 13 known camera-projector angles with CPE technique.

Position (mm) / Angle	0	5	10	15	20	25	30	35	40	45	50
	RMSE (mm)										
5°	1.100	1.086	1.073	1.063	1.052	1.040	1.034	1.019	1.009	0.996	0.988
7.5°	0.717	0.704	0.696	0.682	0.673	0.663	0.662	0.659	0.652	0.653	0.657
10°	0.482	0.484	0.468	0.460	0.453	0.444	0.441	0.431	0.430	0.426	0.437
12.5°	0.376	0.372	0.367	0.357	0.355	0.343	0.337	0.340	0.328	0.328	0.326
15°	0.298	0.290	0.284	0.280	0.274	0.269	0.264	0.262	0.262	0.258	0.264
17.5°	0.252	0.249	0.242	0.232	0.224	0.217	0.213	0.210	0.211	0.208	0.213
20°	0.215	0.211	0.203	0.194	0.190	0.184	0.182	0.185	0.191	0.191	0.187
22.5°	0.192	0.197	0.181	0.170	0.165	0.159	0.155	0.154	0.158	0.153	0.154
25°	0.158	0.164	0.159	0.144	0.141	0.134	0.131	0.132	0.140	0.145	0.155
27.5°	0.145	0.136	0.134	0.127	0.123	0.120	0.119	0.125	0.122	0.125	0.132
30°	0.136	0.126	0.124	0.116	0.113	0.107	0.106	0.104	0.109	0.116	0.114
32.5°	0.138	0.134	0.123	0.116	0.112	0.108	0.106	0.110	0.107	0.111	0.115
35°	0.122	0.170	0.112	0.106	0.105	0.100	0.100	0.101	0.106	0.107	0.111

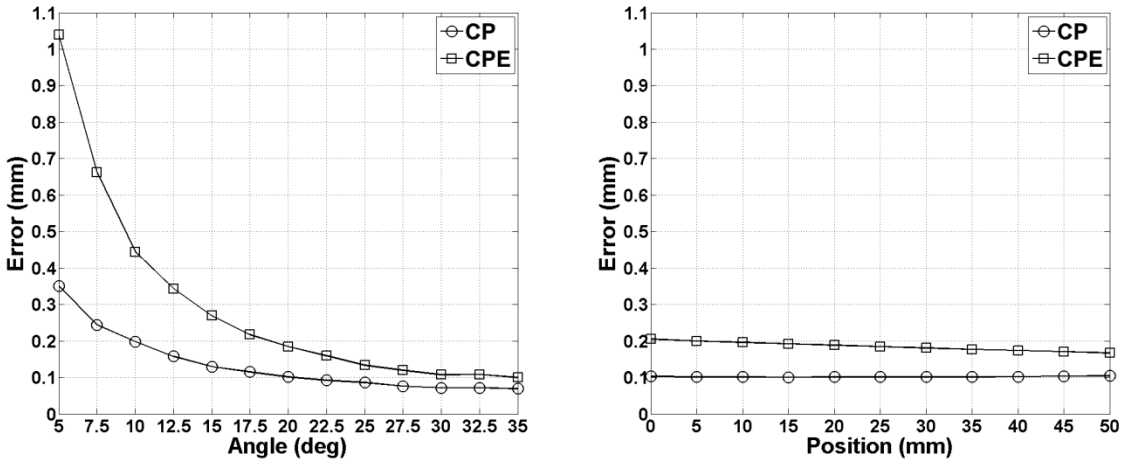

(a) (b)

Figure 7-3 Plane fitting error SDs using CP and CPE techniques: (a) at 13 camera-projector angles (5° to 35° with 2.5° intervals) and fixed position 25 mm; and (b) 11 plate positions (0 mm to 50 mm with 5 mm intervals) and fixed camera-projector angle 20°.

The plane fitting error SD at the 13 camera-projector angles and fixed position 25 mm are shown in Figure 7-3a, for both CP and CPE techniques. The measurement precision over the camera field of view, determined by the plane fitting error SD, becomes decreasingly better (lower error) as the camera-projector angle increases using both CP and CPE techniques. This suggests that in designing a compact 3D scanner, while the gain in precision may be worthwhile for some loss in compactness, the gain in precision greatly diminishes together with loss in compactness beyond an angle of approximately 20°. The plane fitting error SDs for CP are lower than for CPE at all angles; however, the difference becomes smaller with increasing angle, from 0.689 mm at 5° to 0.031 mm at 35°.

Plane fitting error SD at the 11 plate positions and fixed camera-projector angle 20° are shown in Figure 7-3b, for both CP and CPE techniques. The plane fitting error SD remains approximately constant over the position range using both techniques. The plane fitting error SD with CP is approximately half that for CPE at all positions.

The RMSE at the 13 camera-projector angles and fixed position 25 mm is shown in Figure 7-4a, for CP and CPE techniques. The RMSE decreases with increasing angle with both techniques, and the increase in accuracy (decrease in error) diminishes with greater angle and

less compactness. The RMSE with CP is better than for CPE at all angles. The difference between the RMSE for CP and CPE techniques becomes smaller with increasing angle, from 0.689 mm at angle 5° to 0.031 mm at angle 35°.

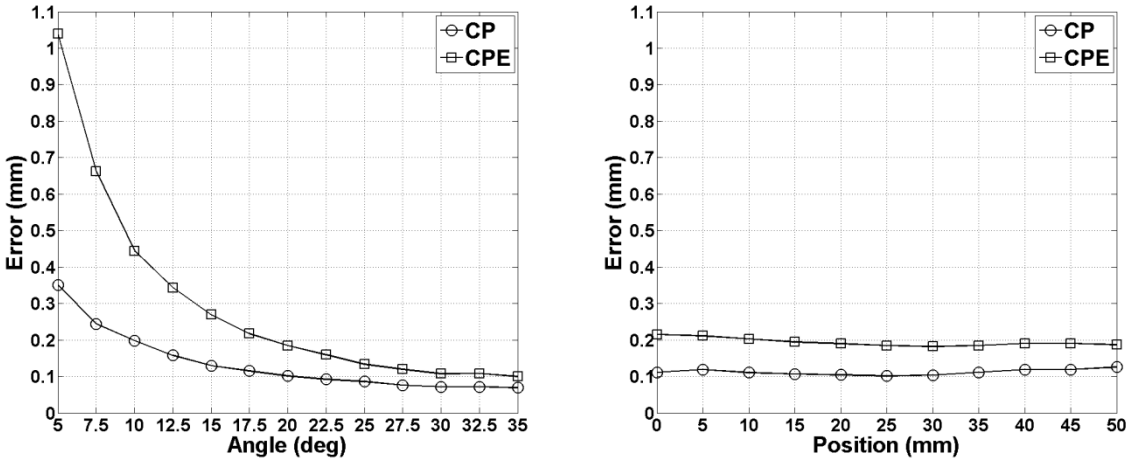

(a) (b)

Figure 7-4 Comparison of CP and CPE techniques: (a) RMSEs at 13 camera-projector angles (5° to 35° with 2.5° intervals), and at fixed position 25 mm; (b) RMSEs at 11 positions (0 mm to 50 mm with 5 mm intervals), and at fixed camera-projector angle 20°.

The RMSE at the 11 positions and fixed camera-projector angle 20° are shown in Figure 7-4b, for CP and CPE techniques. The RMSE remains approximately constant over all plate positions using both techniques. The RMSE for CP are approximately half that for CPE at all positions, demonstrating a gain in accuracy if both horizontal and vertical patterns are used (for CP) compared to only one type of pattern, horizontal or vertical (or CPE).

7.2.2 Double-Sphere Measurement

A double-sphere object was measured at the same 13 camera-projector angles, as shown in Figure 7-5a. The true radii of the two spheres were 50.8 mm, and the true distance between the two sphere centres was 120.0 mm. At each camera-projector angle, the double-sphere object was measured at one position with the front side (with spheres visible) parallel to the camera-projector baseline. A white line mounted on the double-sphere object (Figure 7-5b) and a bold solid line (Figure 7-1) perpendicular to the corresponding camera-projector

baseline were aligned by adjusting the object until a projected laser line was simultaneously coincident with the white line and bold solid line, as shown in Figure 7-5c and Figure 7-5d.

At each camera-projector angle, the object was measured, and a sphere was fitted to each set of measured points for the left and right spheres, respectively. The sphere-fitting error SD, the mean absolute radius error e_r, and the absolute centre-to-centre distance error e_c, (Chapter 3), were calculated from the measured 3D point cloud data of the double-sphere.

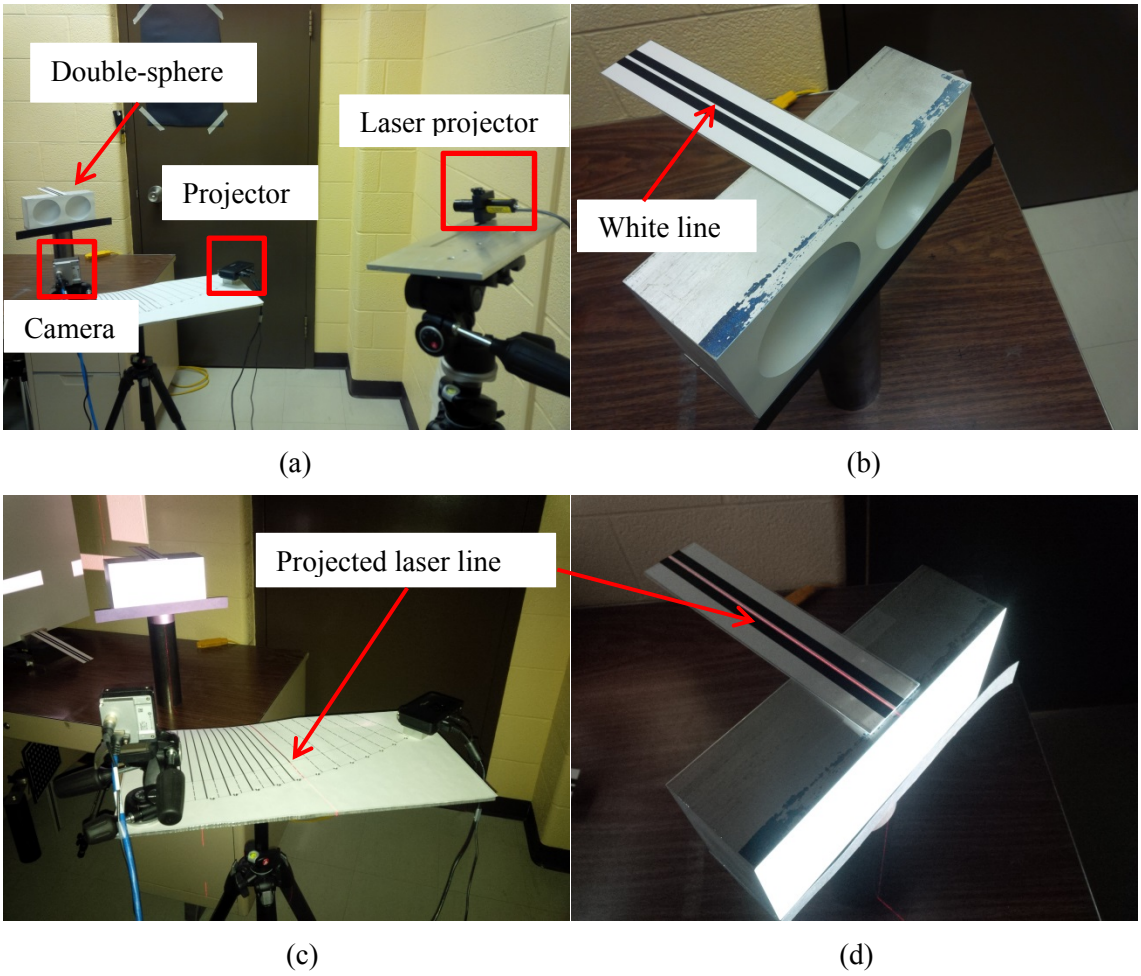

Figure 7-5 System configuration for double-sphere measurement at 13 camera-projector angles: (a) laser projector used for alignment double-sphere object with baseline; (b) white line on double-sphere object; (c) and (d) completed alignment with projected laser line simultaneously coincident with white line in (b) and solid line perpendicular to baseline in Figure 7-1b.

The measured 3D point cloud data of the front side of the double-sphere object at 35° camera-projector angle is shown in Figure 7-6 at two orientations. Some surface regions of the two spheres were not measured (missing data between measured points of the sphere and flat region) due to occlusion. At each camera-projector angle, a plane was fitted to the measured points near the centre of the point cloud data, and a distance threshold was used to separate measured points belonging to the two spheres from the rest of the data. The sphere fitting error SDs, mean absolute radius errors and centre-to-centre distance errors in measuring the double spheres at 13 camera-projector angles (from 5° to 35° with 2.5° intervals) with CP and CPE techniques, respectively, are presented in Table 7-5 and Table 7-6, respectively.

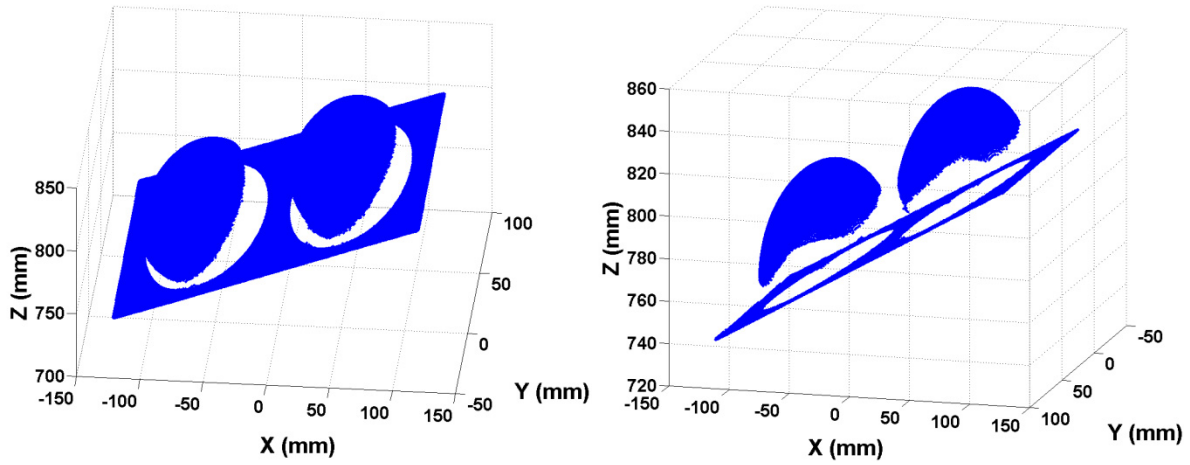

(a) (b)

Figure 7-6 Two views of 3D point cloud data of front side of double-sphere object measured at 35°.camera-projector angle.

Sphere fitting error SDs for measurement of the double-sphere object at 13 known camera-projector angles is shown in Figure 7-7 for CP and CPE techniques, for the left and right spheres, respectively. The sphere fitting error SD in measuring the left and right spheres generally decreased with increasing angle for both CP and CPE techniques, as shown in Figure 7-7a and Figure 7-7b, respectively, except where the SD increased from 0.094 to 0.108 mm from 20° to 22.5° with CP for the left sphere, and from 0.073 to 0.080 mm from 27.5° to 30° with CP for the right sphere.

Table 7-5 Sphere fitting error SDs, mean absolute radius errors, and centre-to-centre distance errors in measuring double-sphere object at 13 known camera-projector angles with CP technique.

Angle	Left Sphere			Right Sphere			Centre-to-Centre Distance Error (mm)
	Number of Points	Mean Absolute Radius Error (mm)	Sphere Fitting Error SD (mm)	Number of Points	Mean Absolute Radius Error (mm)	Sphere Fitting Error SD (mm)	
5°	63,560	0.150	0.191	61,171	0.154	0.197	0.161
7.5°	62,777	0.131	0.168	59,861	0.135	0.172	0.100
10°	62,672	0.114	0.146	59,328	0.115	0.146	0.148
12.5°	61,890	0.100	0.127	58,038	0.100	0.128	0.100
15°	60,947	0.088	0.115	56,800	0.092	0.117	0.037
17.5°	60,214	0.080	0.102	55,633	0.080	0.109	0.040
20°	59,141	0.073	0.094	54,249	0.073	0.093	0.019
22.5°	58,124	0.067	0.108	52,841	0.067	0.085	0.015
25°	57,380	0.062	0.084	51,723	0.062	0.079	0.051
27.5°	56,409	0.057	0.073	50,365	0.057	0.073	0.011
30°	55,517	0.052	0.068	49,212	0.055	0.080	0.030
32.5°	54,487	0.049	0.064	47,941	0.053	0.076	0.002
35°	53,116	0.047	0.062	46,431	0.050	0.064	0.007

Table 7-6 Sphere fitting error SDs, mean absolute radius errors, and centre-to-centre distance errors in measuring double-sphere object at 13 known camera-projector angles with CPE technique.

Angle	Left Sphere			Right Sphere			Centre-to-Centre Distance Error (mm)
	Number of Points	Mean Absolute Radius Error (mm)	Sphere Fitting Error SD (mm)	Number of Points	Mean Absolute Radius Error (mm)	Sphere Fitting Error SD (mm)	
5°	63,607	0.302	0.382	60,889	0.349	0.439	0.601
7.5°	62,704	0.210	0.264	59,738	0.237	0.300	0.666
10°	62,653	0.161	0.203	59,261	0.172	0.217	0.405
12.5°	61,855	0.130	0.164	58,022	0.138	0.174	0.325
15°	60,916	0.110	0.139	56,793	0.117	0.147	0.307
17.5°	60,197	0.095	0.120	55,631	0.099	0.125	0.225
20°	59,138	0.086	0.108	54,247	0.089	0.112	0.195
22.5°	58,122	0.077	0.098	52,848	0.080	0.100	0.168
25°	57,381	0.070	0.096	51,727	0.072	0.091	0.102
27.5°	56,406	0.063	0.081	50,368	0.066	0.083	0.116
30°	55,518	0.058	0.074	49,215	0.062	0.078	0.081
32.5°	54,488	0.056	0.071	47,947	0.059	0.074	0.096
35°	53,120	0.052	0.066	46,435	0.055	0.069	0.094

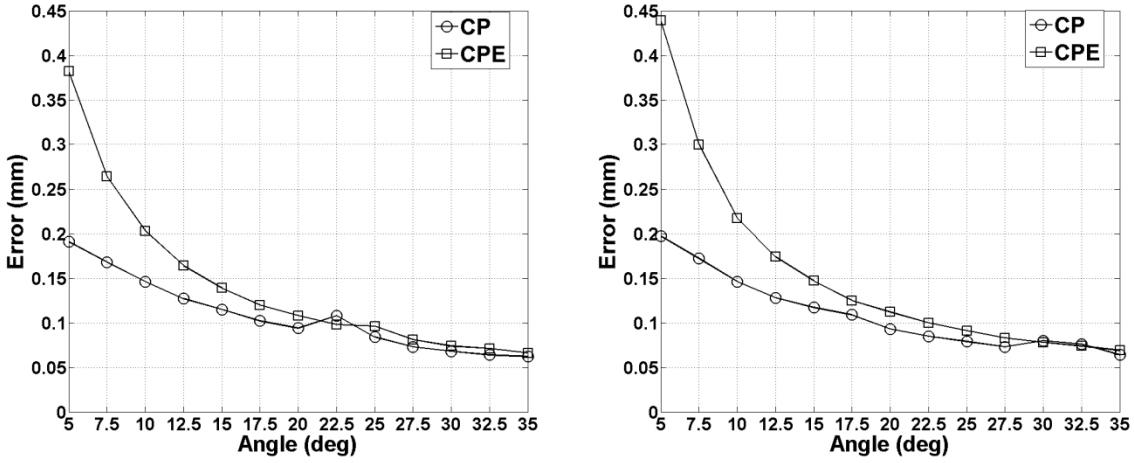

(a) (b)

Figure 7-7 Sphere fitting error SDs for measurement at 13 camera-projector angles (5° to 35° with 2.5° intervals) for CP and CPE techniques: (a) left sphere; (b) right sphere.

The CP technique has lower error SD than the CPE technique at camera-projector angles from 5° to 20° and either the same or minimally lower error SD beyond 20°. The difference between the sphere fitting error SDs for CP and CPE techniques generally decreased with increasing camera-projector angle, from 0.191 mm at 5° angle to 0.004 mm at 35°, and 0.242 mm at 5° to 0.005 mm at 35°, for left and right spheres, respectively.

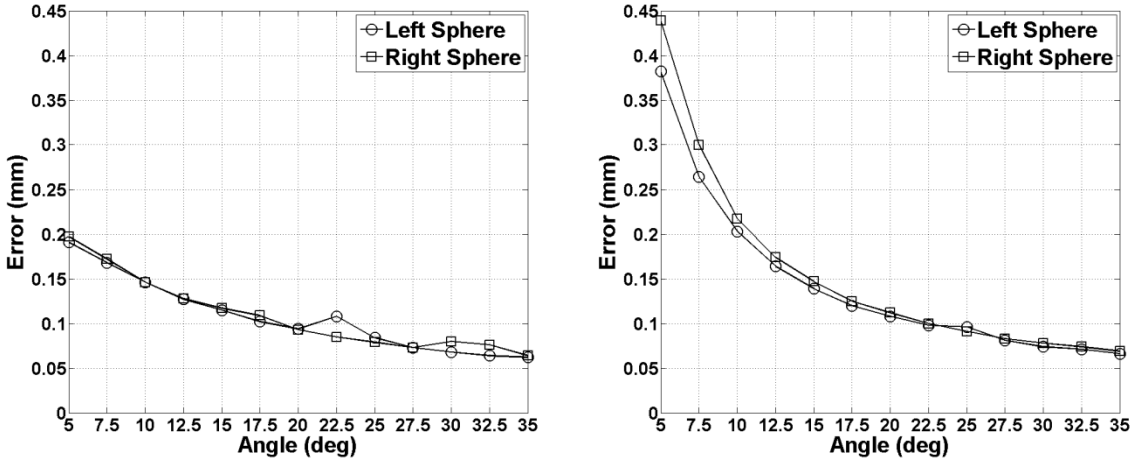

(a) (b)

Figure 7-8 Comparison of uncertainties of measuring left and right spheres at 13 camera-projector angles (5° to 35° with 2.5° intervals): (a) sphere fitting error SDs with CP technique; (b) sphere fitting error SDs with CPE technique.

There was generally little difference between measurement of the left and right spheres at the 13 known camera-projector angles (Figure 7-8), except at small angles below 10° for the CPE technique (Figure 7-8b). Using the CP technique, the difference between the sphere fitting error SDs of measuring the left and right spheres, respectively, was below 0.010 mm over the camera-projector angle range with three exceptions, 0.093 mm, 0.038 mm, and 0.062 mm occurring at angles 22.5°, 30°, and 32.5°, respectively, as shown in Figure 7-8a. Using the CPE technique, the difference between the sphere fitting error SDs of measuring the left and right sphere, was also below 0.010 mm at camera-projector angles 12.5° and higher, as shown in Figure 7-8b.

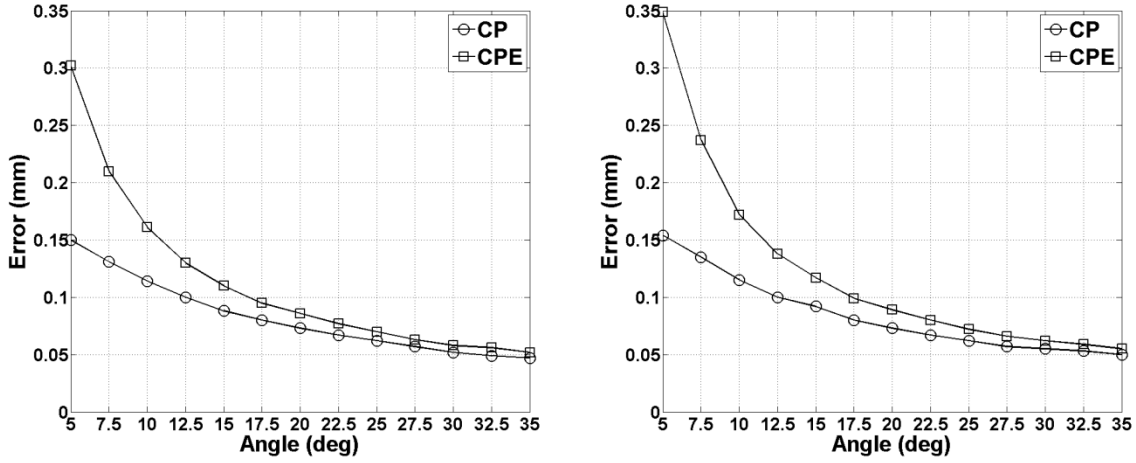

(a) (b)

Figure 7-9 3D shape measurement accuracy, inversely represented by mean absolute radius errors, at 13 known camera-projector angles (5° to 35° with 2.5° intervals) for CP and CPE techniques, for: (a) left sphere, and (b) right sphere.

The 3D shape-measurement accuracy, inversely represented by mean absolute radius errors of the spheres, at the 13 known camera-projector angles, using CP and CPE techniques, is shown in Figure 7-9. The errors decreased with increasing camera-projector angle, and the rate of decrease diminished with increasing angle. The measurement accuracy was higher for CP than CPE at all angles and the difference in errors between the techniques decreased with increasing angle, from 0.152 mm at 5° to 0.005 mm at 35° for the left sphere, and from 0.195 mm at 5° to 0.005 mm at 35° for the right sphere. The difference in measurement accuracy

between the left and right spheres was below 0.010 at all angles for CP (Figure 7-10a) and below 0.010 mm for 12.5° and higher for CPE (Figure 7-10b).

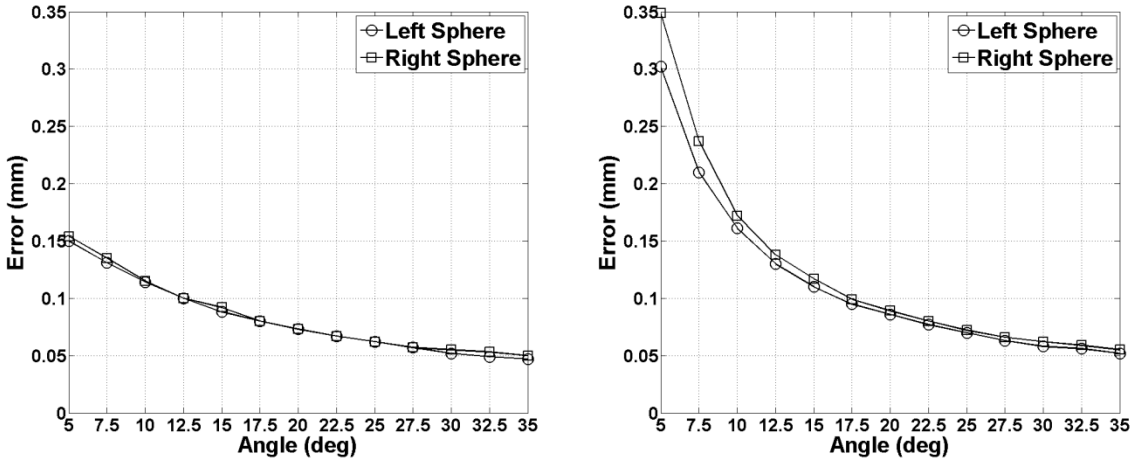

(a) (b)

Figure 7-10 3D shape measurement accuracy, inversely represented by mean absolute radius errors, at 13 known camera-projector angles (5° to 35° with 2.5° intervals) for left and right spheres, for: (a) CP technique, and (b) CPE technique.

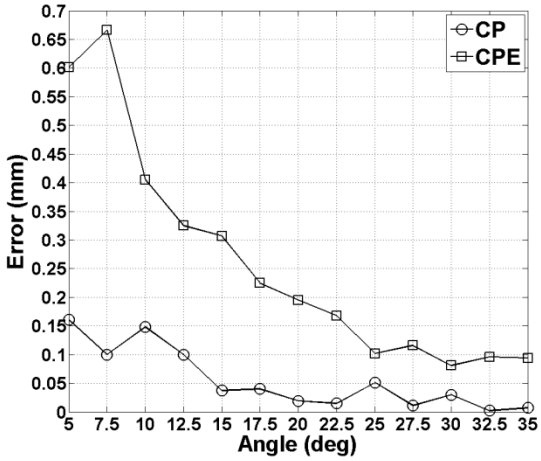

Figure 7-11 Centre-to-centre distance errors in measuring double-sphere at 13 camera-projector angles (5° to 35° with 2.5° intervals) with CP and CPE techniques.

Centre-to-centre distance errors in measuring the double-sphere at 13 known camera-projector angles with CP and CPE techniques, are shown in Figure 7-11. The measurement accuracy for both CP and CPE techniques generally increased (errors decreased) with

increasing angle from 0.161 mm at 5° to 0.007 mm at 35° for CP and from 0.601 mm at 5° to 0.094 mm at 35° for CPE techniques, respectively. The measurement accuracy with the CP technique was considerably higher than for CPE at all angles and the error difference between the techniques generally decreased with increasing angle.

Overall, measurement results of both the flat plate and double-sphere object show that the measurement precision and accuracy both increase as the camera-projector angle increases. In designing a compact 3D measurement system, there is therefore a clear tradeoff in loss of accuracy with increased compactness. Improvement accuracy would be at the cost of loss in compactness. The results also show that the precision and accuracy with the CP technique, which uses both horizontal and vertical projected patterns, are higher than for CPE, which uses only horizontal or vertical patterns. Accuracy improvement and accuracy would therefore be at the cost of lower acquisition speed. However, the differences in precision and accuracy between measurement with CP and CPE techniques, both decrease with increasing camera-projector angle. This suggests that it both techniques can likely satisfy accuracy requirements at large camera-projector angle, and if acquisition speed is more important than compactness, the CPE technique would be preferred as it can reduce the number of fringe patterns to half. However, if compactness is most important, the loss of accuracy in a more compact design can be partly offset by using the CP technique, at the cost of acquisition speed.

7.3 System Configuration for Compactness Study of Consumer System

The system geometry for the compactness study of a consumer system is similar to that for the compactness study of the industrial system, with a few differences, as shown in Figure 7-12. Instead of a fixed camera position, the camera in this study was moved to different positions C1 to C4. The orientation of object surfaces was kept perpendicular to the camera image plane during the entire study. The initial camera working distance from the object (standoff distance) at position C1 was 32 in (81.28 cm), which was identical to the fixed projector working distance during the entire study. The camera was then moved toward the

object to working distances: 28 in (71. cm) (at C4), 24 in (60.96 cm) (at C2) and 16 in (40.64 cm) (at C3). At camera positions C1, C2 and C4, the projector was moved to three positions

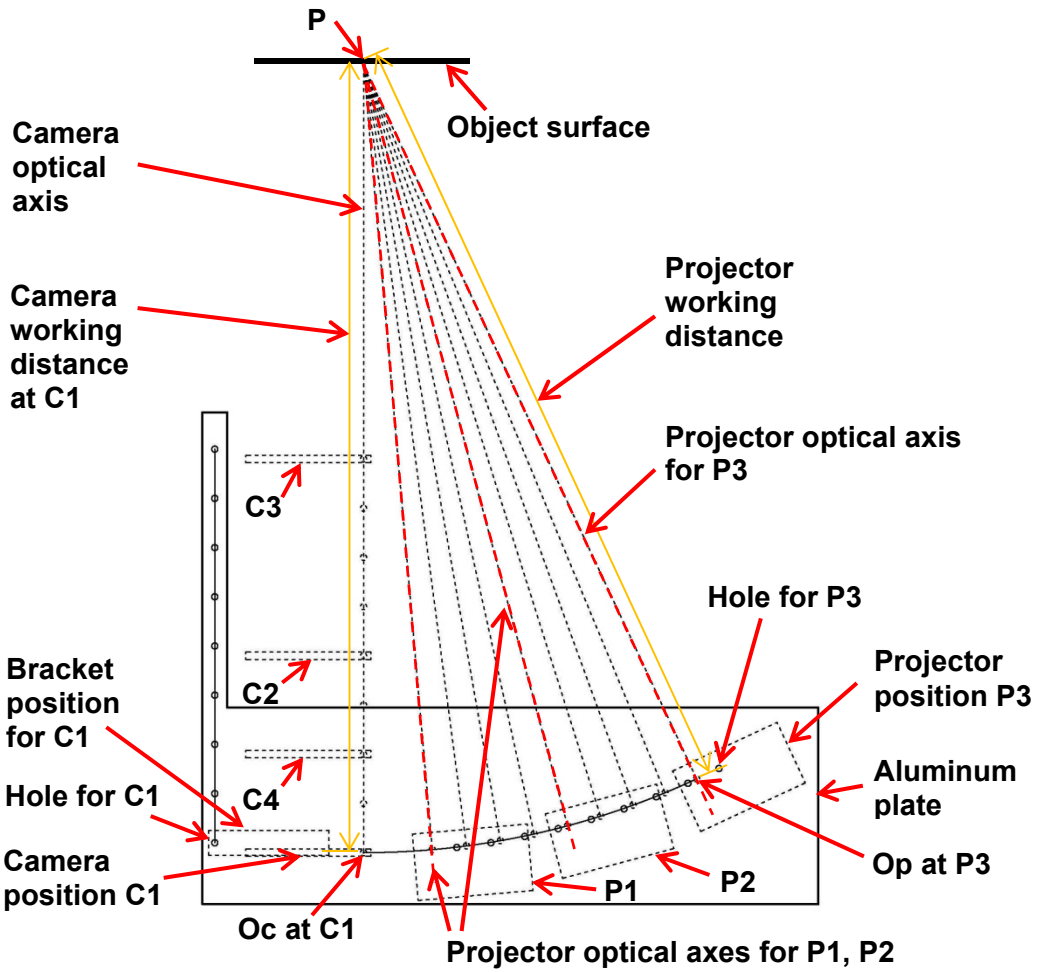

Figure 7-12 System configuration for compactness study of consumer system.

P1, P2 and P3 (the projector orientation was adjusted accordingly to ensure that its optical axis Oc-P meets the camera's optical axis Op-P at surface point P, where Oc and Op are optical centres of the camera and projector, respectively), resulting in three camera-projector angles 5° at P1, 15° at P2 and 25° at P3. At camera position C3, the projector was only positioned at P3. The different camera positions were used to study the effect of camera-projector pixel ratio on 3D measurement accuracy. The camera-projector pixel ratio is related to the number of camera pixels that "see" a surface region illuminated by one projector pixel. The camera-projector pixel ratio increases as the camera is moved closer to the object. This

study is useful because the most compact system at a large camera-projector angle is achieved when the camera is closer to the object compared to the initial position C1. In Figure 7-12, the solid circles along the vertical line on the left side of the aluminum plate indicate positions of holes for mounting a bracket used to hold the camera. The solid circles along an arc on the right side of the aluminum plate indicate positions of holes for mounting the projector. Note that more holes for more camera and projector positions than those used in this study have been made for future study.

7.4 Experiments and Results with Consumer System

7.4.1 Flat Plate Measurement

A flat plate, mounted on the same micrometer translation stage, was measured at the following combinations of camera and projector positions: C1P1, C1P2, C1P3, C2P1, C2P2, C2P3, C4P1, C4P2, C4P3, and C3P3. At each camera-projection position combination, the plate was moved to 11 known positions (0 mm to 50 mm with 5 mm intervals) towards the sensor during the experiment. At each plate position, for each camera-projector-object configuration, the plate was measured and plane fitting error SD and RMSE were computed from raw 3D data to assess the measurement accuracy. The plane fitting errors SD and RMSE in measuring the flat plate at the 11 positions of the translation stage and 10 camera-projector position combinations are presented in Figure 7-13 and Figure 7-14, respectively. The plane fitting error SD and RMSE at different camera-projector position combinations are compared in two ways: 1) fixed camera position and different projector positions (left columns in Figure 7-13 and Figure 7-14), and 2) fixed projector position and different camera positions (right columns in Figure 7-13 and Figure 7-14).

Figure 7-13 Plane fitting error SD at 11 plate positions (0 mm to 50 mm with 5 mm intervals) and different camera-projector position combinations: left column (a)-(c), fixed camera position and different projector positions: (a) C1P1, C1P2, and C1P3; (b) C2P1, C2P2, and C2P3; (c) C4P1, C4P2, and C4P3; and right column (d)-(f), fixed projector position and different camera positions: (d) C1P1, C2P1, and C4P1; (e) C1P2, C2P2, and C4P2; (f) C1P3, C2P3, C3P3 and C4P3.

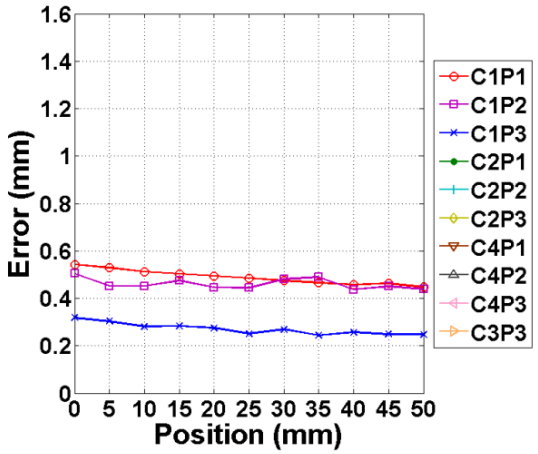
Error (mm)
Position (mm)
C1P1
C1P2
C1P3
C2P1
C2P2
C2P3
C4P1
C4P2
C4P3
C3P3

(a)

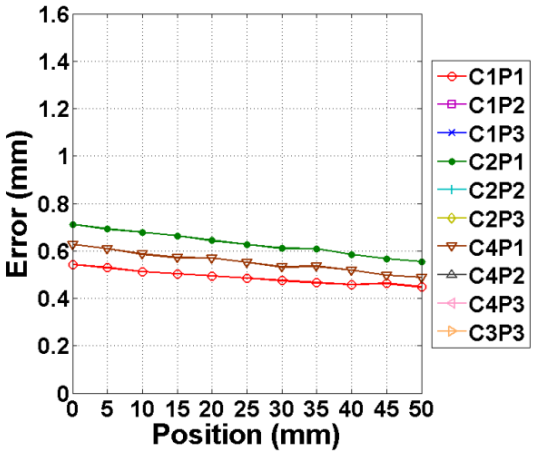
Error (mm)
Position (mm)
C1P1
C1P2
C1P3
C2P1
C2P2
C2P3
C4P1
C4P2
C4P3
C3P3

(d)

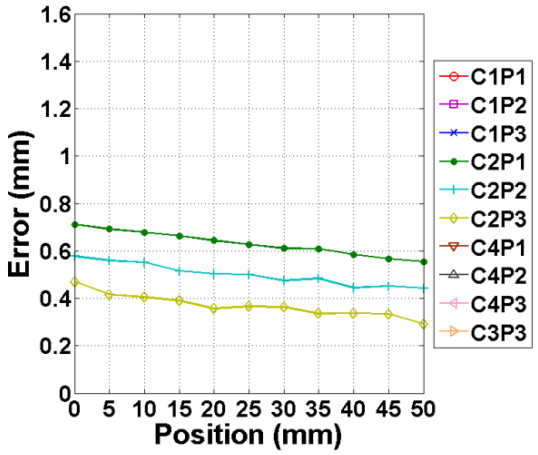
Error (mm)
Position (mm)
C1P1
C1P2
C1P3
C2P1
C2P2
C2P3
C4P1
C4P2
C4P3
C3P3

(b)

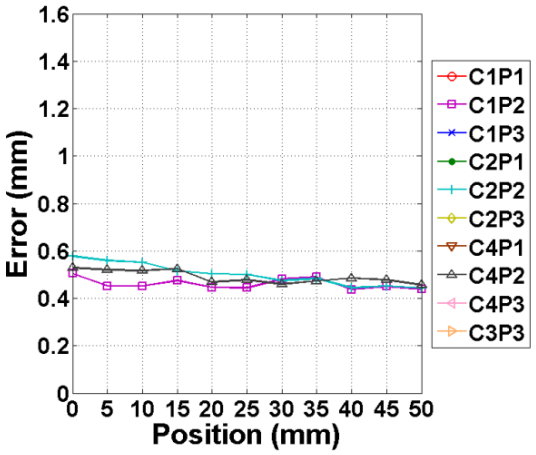
Error (mm)
Position (mm)
C1P1
C1P2
C1P3
C2P1
C2P2
C2P3
C4P1
C4P2
C4P3
C3P3

(e)

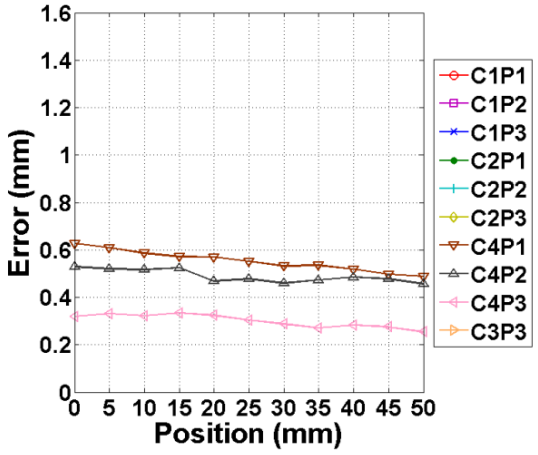
Error (mm)
Position (mm)
C1P1
C1P2
C1P3
C2P1
C2P2
C2P3
C4P1
C4P2
C4P3
C3P3

(c)

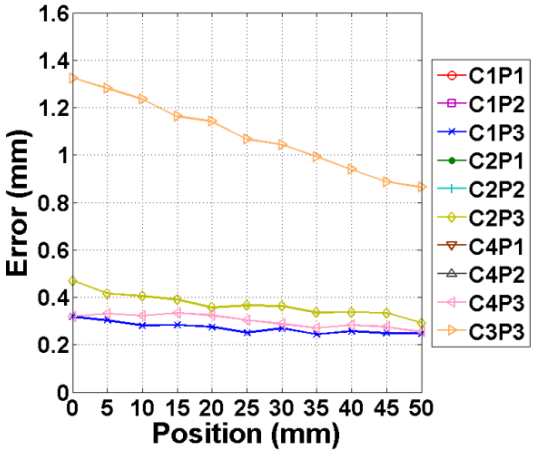
Error (mm)
Position (mm)
C1P1
C1P2
C1P3
C2P1
C2P2
C2P3
C4P1
C4P2
C4P3
C3P3

(f)

For Figure 7-13a to Figure 7-13c (left column), the camera position was fixed at C1, C2 and C4, respectively. At each fixed camera position, the plane fitting error SD decreased with increasing camera-projector angle for all plate positions, except for two plate positions 30 mm and 35 mm, where the error SD at projector position P1 was smaller than at P2 (Figure 7-13a). This suggests that increased compactness would be at the cost of loss of measurement precision across the plate. For Figure 7-13d to Figure 7-13f (right column), the projector position was fixed at P1, P2 and P3, respectively. At each fixed projector position, the plane fitting error SD increased as the camera was closer to the object, suggesting that increased camera-pixel ratio had a detrimental effect on measurement precision across the plate. At fixed projector position P2 (Figure 7-13e), the three plane fitting error SD curves of camera positions C1, C2 and C4 are similar, particularly at plate positions 30 mm, 35 mm, 45 mm and 50 mm. At camera-projector combination C3P3 (Figure 7-13f), the plane fitting error SDs are much larger than those at all other camera-projector position combinations at all plate positions. The error SD is larger than 1 mm at plate positions 0 mm to 30 mm. This poor result is largely due to the large camera-projector pixel ratio (approximately 3:1) at C3P3.

For Figure 7-14a to Figure 7-14c (left column), the camera position was fixed at C1, C2 and C4, respectively. At each camera position, the RMSE decreased with increasing camera-projector angle for all plate positions, except, in Figure 7-14a, where the RMSE curves for projector positions P1 and P2 meet at plate end positions 0 mm and 50 mm, and in Figure 7-14c, at plate positions 45 mm and 50 mm, where the RMSE at P1 was smaller than at P2. For Figure 7-14d to Figure 7-14f (right column), the projector was fixed at P1, P2 and P3, respectively. At each projector position, the RMSE generally increased as the camera was closer to the object. At fixed projector position P1 (Figure 7-14d), the RMSE curves for camera positions C2 and C4 meet at plate position 0 mm, and for C1 and C4 are nearly identical at plate positions 45 mm and 50 mm. At projector position P2 (Figure 7-14e), the

Figure 7-14 RMSE at 11 plate positions (0 mm to 50 mm with 5 mm intervals) and different camera-projector position combinations: left column (a)-(c), fixed camera position and different projector positions: (a) C1P1, C1P2, and C1P3; (b) C2P1, C2P2, and C2P3; (c) C4P1, C4P2, and C4P3; and right column (d)-(f), fixed projector position and different camera positions: (d) C1P1, C2P1, and C4P1; (e) C1P2, C2P2, and C4P2; (f) C1P3, C2P3, C3P3 and C4P3.

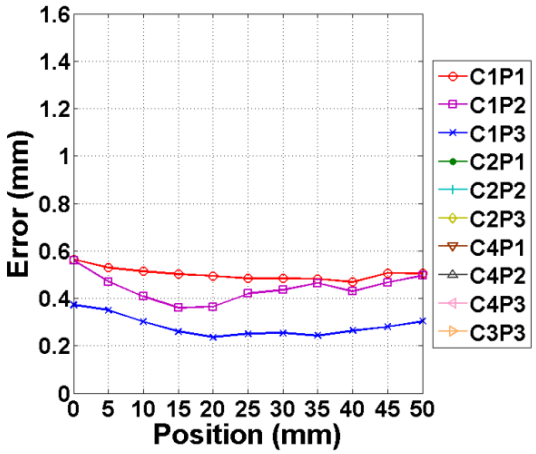
Error (mm)
Position (mm)
C1P1
C1P2
C1P3
C2P1
C2P2
C2P3
C4P1
C4P2
C4P3
C3P3

(a)

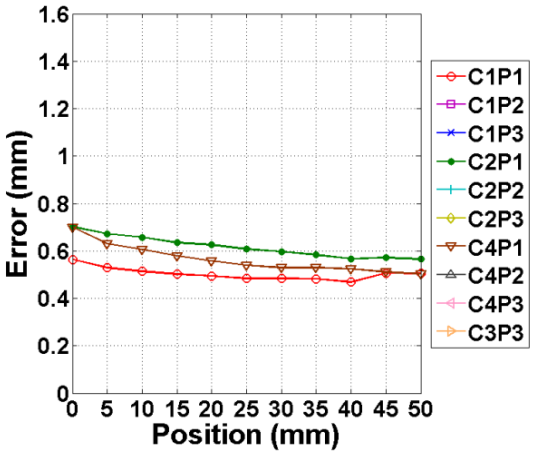
Error (mm)
Position (mm)
C1P1
C1P2
C1P3
C2P1
C2P2
C2P3
C4P1
C4P2
C4P3
C3P3

(d)

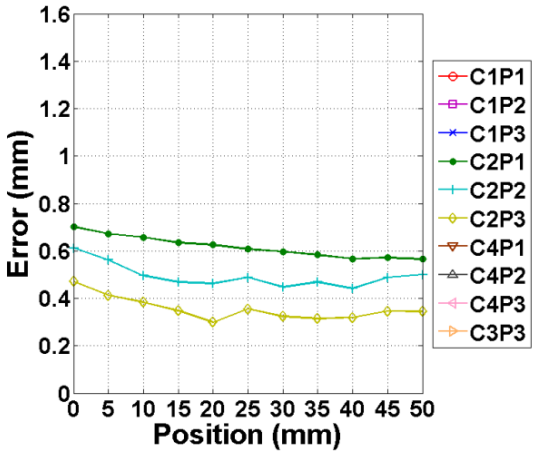
Error (mm)
Position (mm)
C1P1
C1P2
C1P3
C2P1
C2P2
C2P3
C4P1
C4P2
C4P3
C3P3

(b)

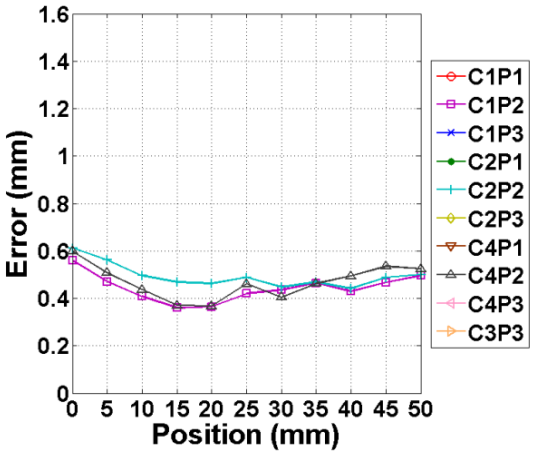
Error (mm)
Position (mm)
C1P1
C1P2
C1P3
C2P1
C2P2
C2P3
C4P1
C4P2
C4P3
C3P3

(e)

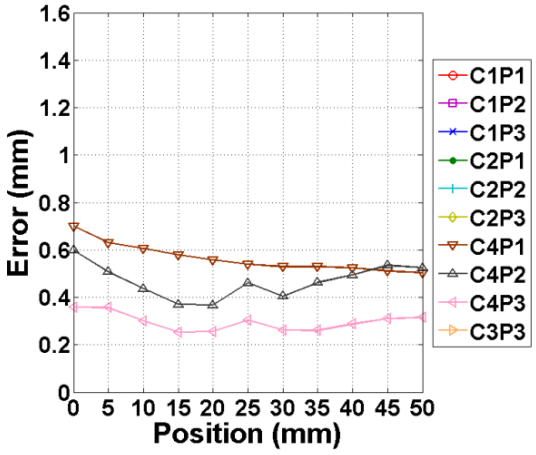
Error (mm)
Position (mm)
C1P1
C1P2
C1P3
C2P1
C2P2
C2P3
C4P1
C4P2
C4P3
C3P3

(c)

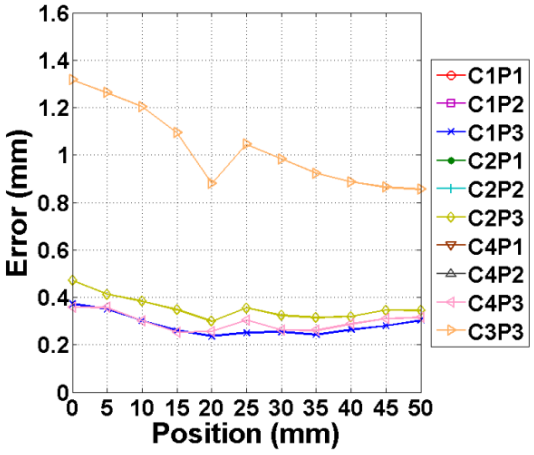
Error (mm)
Position (mm)
C1P1
C1P2
C1P3
C2P1
C2P2
C2P3
C4P1
C4P2
C4P3
C3P3

(f)

RMSE curves for camera positions C1, C2 and C4 are particularly close except at plate positions 15 mm and 20 mm. For Figure 7-14f, for projector position P3, RMSE curves for camera positions C1 and C4 are nearly identical and close to that for C2. At camera-projector combination C3P3, the RMSE was much larger than at all other camera-projector position combinations at all plate positions. The RMSE was larger than 1 mm at plate positions 0 mm to 15 mm and 25 mm. The poor measurement accuracy result for C3P3 was again largely due to the large camera-projector pixel ratio (approximately 3:1) at C3P3.

In flat plate measurement with the consumer system, the best measurement precision (plane fitting error SD) and accuracy (RMSE) were both achieved at the camera-projector position combination C1P3, with camera and projector working at the same stand-off distance and the largest camera-projector angle 25°. This conclusion is in accordance with the conclusion of the compactness study of the industrial system in measuring both the flat plate and double-sphere object. In general, both the measurement precision and accuracy increase with increasing camera-projector angle, and in designing a compact 3D measurement system, increased compactness can be achieved at a cost of loss of accuracy. In design of a measurement system, increased measurement accuracy can be achieved at a cost of loss of compactness. Furthermore, while in computer vision systems, having the object closer to the camera would tend to increase measurement accuracy (more camera pixels per unit area on the object being measured), an important finding of this consumer system compactness study was that the accuracy decreased with the object closer to the camera. This was due to the mismatch of number of camera pixels to number of projector pixels corresponding to the same object surface region, (the large camera-projector pixel ratio (approximately 3:1)) with the object closer to the camera.

7.4.2 Spherical Ball Measurement

A spherical ball, mounted on the micrometer translation stage, was measured at the same camera-projector position combinations as used for the plate measurements: C1P1, C1P2, C1P3, C2P1, C2P2, C2P3, C4P1, C4P2, C4P3, and C3P3, At each camera-projection position, the ball was moved to the same 11 known plate positions (0 mm to 50 mm with 5 mm intervals) toward the sensor during the experiment. At each position, the ball was

measured, and the sphere fitting error SD, mean absolute radius error, and centre-to-centre distance error, were computed from raw 3D data to assess the measurement accuracy. These error parameters in measuring the ball at the 11 plate positions and 10 camera-projector positions are presented in Figure 7-15, Figure 7-16, and Figure 7-17, respectively, and are compared in two ways: 1) fixed camera position and different projector positions (left column) and 2) fixed projector position and different camera positions (right column) in each figure.

For Figure 7-15a to Figure 7-15c, the camera position was fixed at C1, C2 and C4, respectively. At each camera position, the sphere fitting error SD decreased with increasing camera-projector angle at all ball positions on the translation stage. In Figure 7-15d to Figure 7-15f, the projector position was fixed at P1, P2 and P3, respectively. For projector position P1, (Figure 7-15d), there is only a small increase in error SD as the camera gets closer to the object from C1 to C4, and nearly no change as the camera gets even closer to the object from C4 to C2. At projector position P2 (Figure 7-15e), the error SD curves for C1, C2 and C3 are nearly identical at all ball positions. At projector position P3 (Figure 7-15f), the error SD curves for C1, C2, C3 and C4 differ by less than 0.01 mm close to 0.1 mm. For C3P3, this was different from the large plane fitting error SD at C3P3 (Figure 7-13f). The smaller error SD for the spherical ball compared to the flat plate at all camera-projector position combinations may be due to the ball occupying a much smaller region than the plate, and thus suffering less image distortion than the plate measurement. The best sphere fitting error SD was achieved at the camera-projector position combination C1P3, where the sphere fitting error SD at all ball positions was below 0.100 mm. This is the same camera-projector position combination at which the best measurement precision (plane fitting error SD) and accuracy (RMSE) were found for the plate measurements (Section 7.4.1).

Figure 7-15 Sphere fitting error SD at 11 positions (0 mm to 50 mm with 5 mm intervals) and different camera-projector position combinations: left column (a)-(c), fixed camera position and different projector positions: (a) C1P1, C1P2, and C1P3; (b) C2P1, C2P2, and C2P3; (c) C4P1, C4P2, and C4P3; and right column (d)-(f), fixed projector position and different camera positions: (d) C1P1, C2P1, and C4P1; (e) C1P2, C2P2, and C4P2; (f) C1P3, C2P3, C3P3 and C4P3.

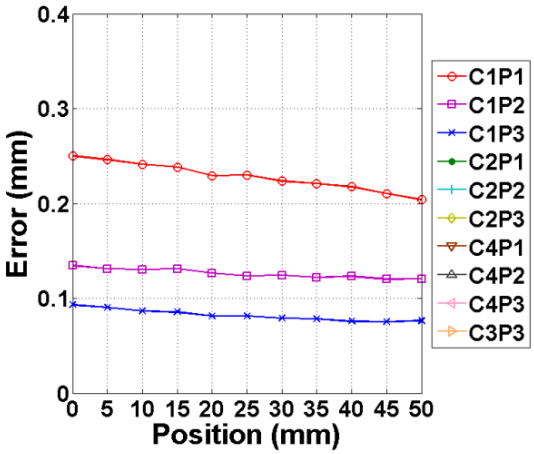
Error (mm)
Position (mm)
C1P1
C1P2
C1P3
C2P1
C2P2
C2P3
C4P1
C4P2
C4P3
C3P3

(a)

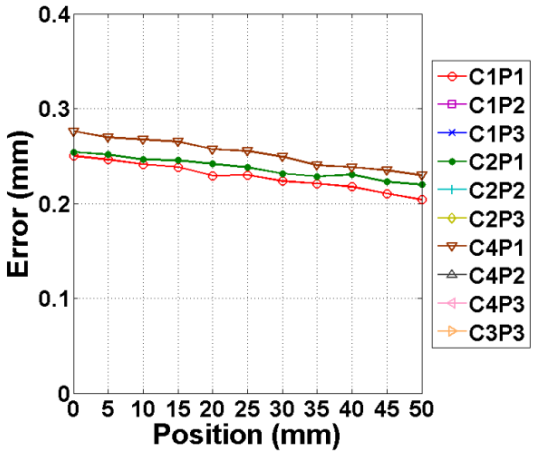
Error (mm)
Position (mm)
C1P1
C1P2
C1P3
C2P1
C2P2
C2P3
C4P1
C4P2
C4P3
C3P3

(d)

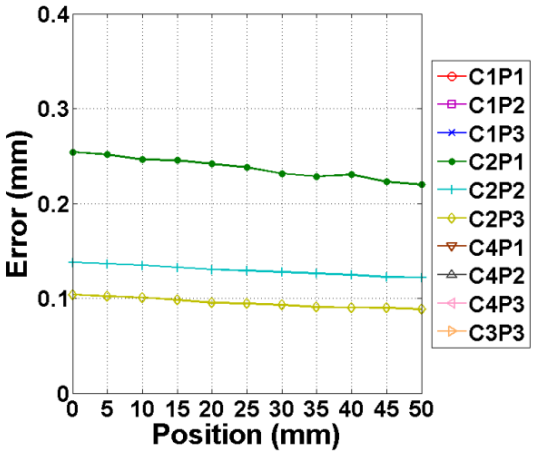
Error (mm)
Position (mm)
C1P1
C1P2
C1P3
C2P1
C2P2
C2P3
C4P1
C4P2
C4P3
C3P3

(b)

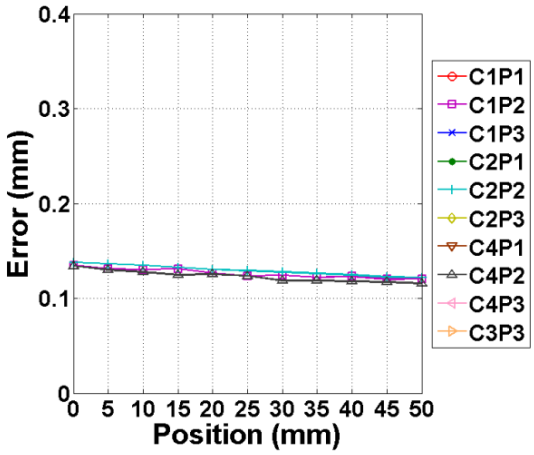
Error (mm)
Position (mm)
C1P1
C1P2
C1P3
C2P1
C2P2
C2P3
C4P1
C4P2
C4P3
C3P3

(e)

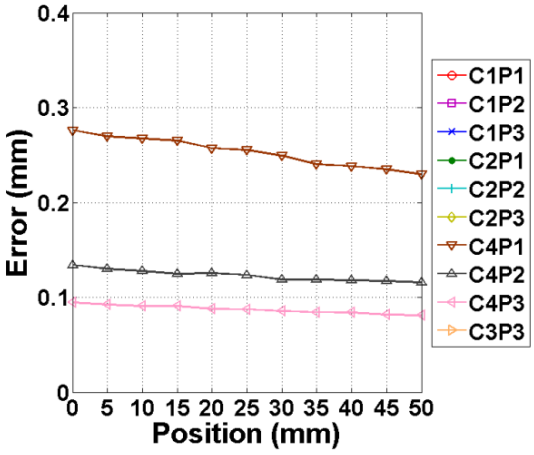
Error (mm)
Position (mm)
C1P1
C1P2
C1P3
C2P1
C2P2
C2P3
C4P1
C4P2
C4P3
C3P3

(c)

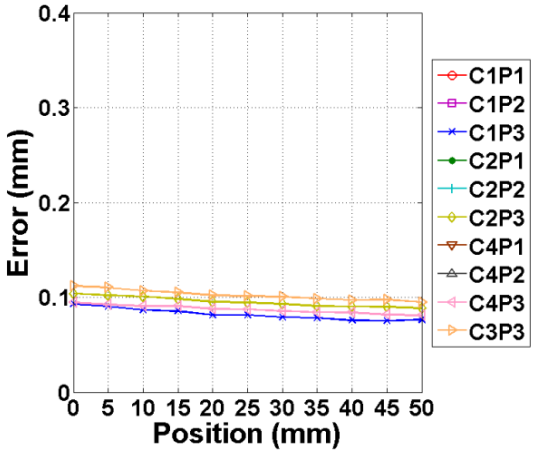
Error (mm)
Position (mm)
C1P1
C1P2
C1P3
C2P1
C2P2
C2P3
C4P1
C4P2
C4P3
C3P3

(f)

The mean absolute radius error for different camera-projector and ball positions are shown in Figure 7-16. For Figure 7-16a to Figure 7-16c, the camera position was fixed at C1, C2 and C4, respectively. The trends in comparing error curves for different camera positions varied for the different projector positions. At camera position C1 (Figure 7-16a), the error at projector position P2 was smaller than at P1 and P3 at all ball positions. The error curves for P1 and P3 intersect at the ball position 25 mm. At camera position C2 (Figure 7-16b), the error decreases greatly with larger camera-projector angle from approximately 0.35 mm at P1 to approximately 0.1 at P3. At camera position C4 (Figure 7-16c), the error at P1 (small camera-projector angle) was much larger than for P2 and P3. The trends for P2 and P3 changed across varying object position, where the error curves for P2 and P3 intersect at the position 25 mm. In Figure 7-16d to Figure 7-16f, the projector position was fixed at P1, P2 and P3, respectively. At projector position P1 (Figure 7-16d), the error was lowest (best accuracy) for the camera position farthest from the object C1, and the error was much lower than for the other camera positions (0.1 mm to more than 0.3 mm lower). The highest error (worst accuracy) was for the middle camera position C4 (between C1 and C2). At projector position P2 (Figure 7-16e), the error at C2 was worse than for C1 and C4. At fixed projector position P3 (Figure 7-16f), the error at C2 was smaller than at C1, C3 and C4 at ball positions 0 to 25 mm. The errors for C1 and C3 increased and for C4 decreased as the ball was moved closer to the sensor, while for C2 the error was low and nearly constant at 0.1 mm across all ball positions.

Figure 7-16 Mean absolute radius errors at 11 positions (0 mm to 50 mm with 5 mm intervals) and different camera-projector position combinations: left column (a)-(c), fixed camera position and different projector positions: (a) C1P1, C1P2, and C1P3; (b) C2P1, C2P2, and C2P3; (c) C4P1, C4P2, and C4P3; and right column (d)-(f), fixed projector position and different camera positions: (d) C1P1, C2P1, and C4P1; (e) C1P2, C2P2, and C4P2; (f) C1P3, C2P3, C3P3 and C4P3.

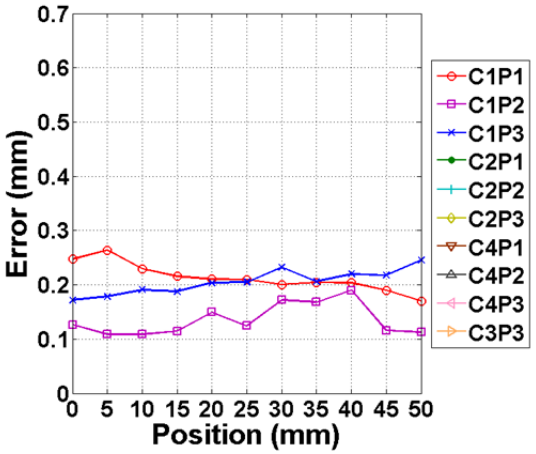
Error (mm)
Position (mm)
C1P1
C1P2
C1P3
C2P1
C2P2
C2P3
C4P1
C4P2
C4P3
C3P3

(a)

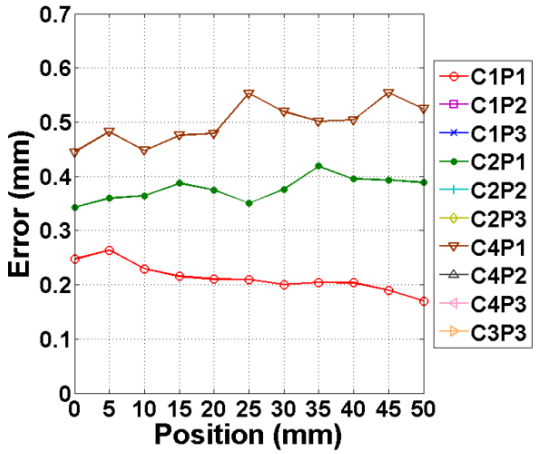
Error (mm)
Position (mm)
C1P1
C1P2
C1P3
C2P1
C2P2
C2P3
C4P1
C4P2
C4P3
C3P3

(d)

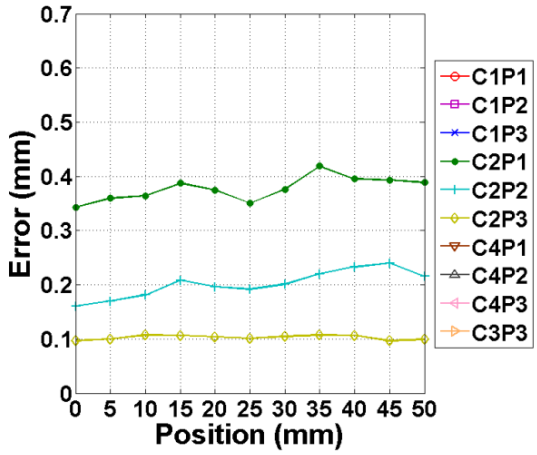
Error (mm)
Position (mm)
C1P1
C1P2
C1P3
C2P1
C2P2
C2P3
C4P1
C4P2
C4P3
C3P3

(b)

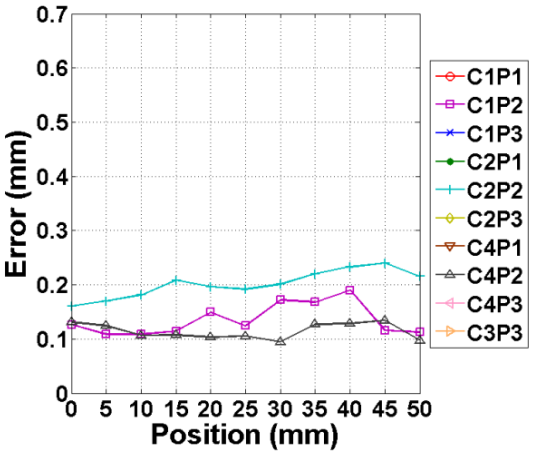
Error (mm)
Position (mm)
C1P1
C1P2
C1P3
C2P1
C2P2
C2P3
C4P1
C4P2
C4P3
C3P3

(e)

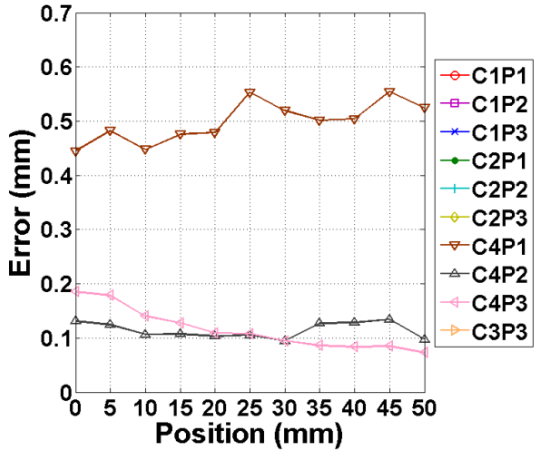
Error (mm)
Position (mm)
C1P1
C1P2
C1P3
C2P1
C2P2
C2P3
C4P1
C4P2
C4P3
C3P3

(c)

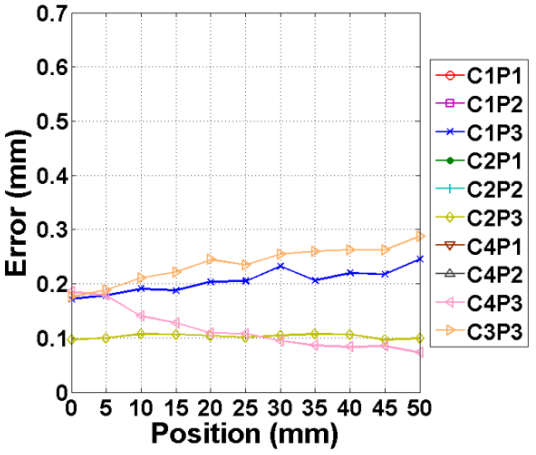
Error (mm)
Position (mm)
C1P1
C1P2
C1P3
C2P1
C2P2
C2P3
C4P1
C4P2
C4P3
C3P3

(f)

The trends in centre-to-centre distance errors at all camera-projector position combinations varied greatly across ball positions, as shown in Figure 7-17. One common characteristic of the centre-to-centre distance error curves for all camera-projector position combinations, except for C1P1 (largest camera-object distance with narrowest camera-projector angle), was that all global minima occur near ball position 25 mm (the mid-range of depth), for which the camera and projector were at best focus. For C1P1, the smallest errors occurred at ball positions 0 and 50 mm (farthest and nearest positions to the sensor, respectively) with errors maximum near mid-depth 25 mm. The more complex error trends across ball positions may be related to sensitive light reflection changes that occur as the ball approaches the sensor compared to a plate.

In spherical ball measurement with the consumer system, the variation of measurement precision with camera-projector angle was consistent with the flat plate measurements with the consumer system, and the flat plate measurement and double-sphere object measurement with the industrial system. The best camera-projector position combination for the consumer system seemed to be C1P3 (shown in blue in all graphs) where the best measurement precision (plane fitting error SD) and accuracy (RMSE) were found for the plate measurements (Section 7.4.1) and where even the sphere centre-to-centre distance errors appeared most consistently best with less than 0.1 mm for most object positions, and at worst 0.18 mm. C1P3 is the camera-projector position with the largest camera-object distance and widest camera-projector angle. The trend of best measurement accuracy and precision for this position for the consumer system is consistent with results for the industrial system, where best accuracy and precision occurred for larger angle. The better accuracy for the greater camera-object distance at C1P3 is likely due to better camera-projector pixel ratio.

Figure 7-17 Centre-to-centre distance errors at 11 positions (0 mm to 50 mm with 5 mm intervals) and different camera-projector position combinations: left column (a)-(c), fixed camera position and different projector positions: (a) C1P1, C1P2, and C1P3; (b) C2P1, C2P2, and C2P3; (c) C4P1, C4P2, and C4P3; and right column (d)-(f), fixed projector position and different camera positions: (d) C1P1, C2P1, and C4P1; (e) C1P2, C2P2, and C4P2; (f) C1P3, C2P3, C3P3 and C4P3.

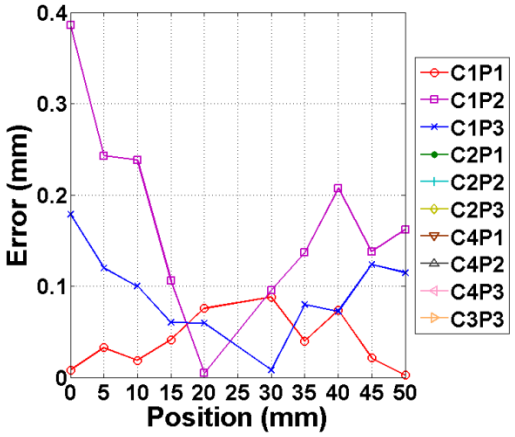
Error (mm)
Position (mm)
C1P1
C1P2
C1P3
C2P1
C2P2
C2P3
C4P1
C4P2
C4P3
C3P3

(a)

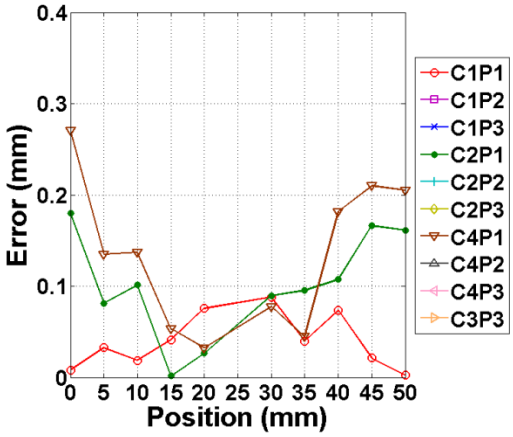
Error (mm)
Position (mm)
C1P1
C1P2
C1P3
C2P1
C2P2
C2P3
C4P1
C4P2
C4P3
C3P3

(d)

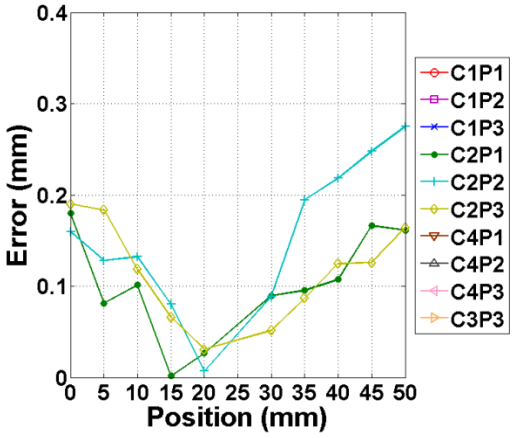
Error (mm)
Position (mm)
C1P1
C1P2
C1P3
C2P1
C2P2
C2P3
C4P1
C4P2
C4P3
C3P3

(b)

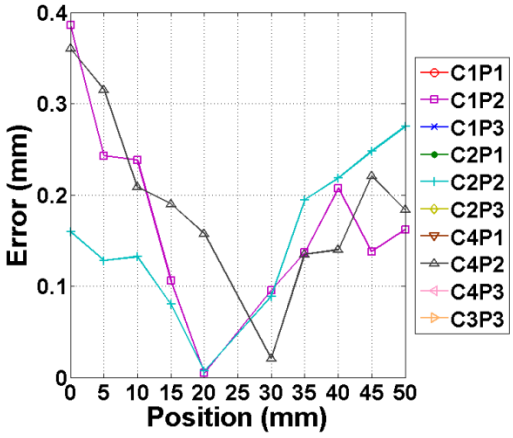
Error (mm)
Position (mm)
C1P1
C1P2
C1P3
C2P1
C2P2
C2P3
C4P1
C4P2
C4P3
C3P3

(e)

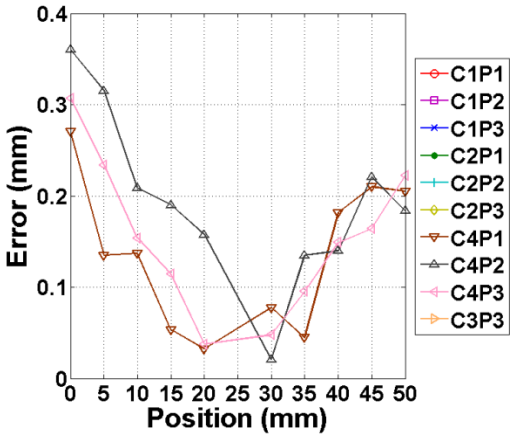
Error (mm)
Position (mm)
C1P1
C1P2
C1P3
C2P1
C2P2
C2P3
C4P1
C4P2
C4P3
C3P3

(c)

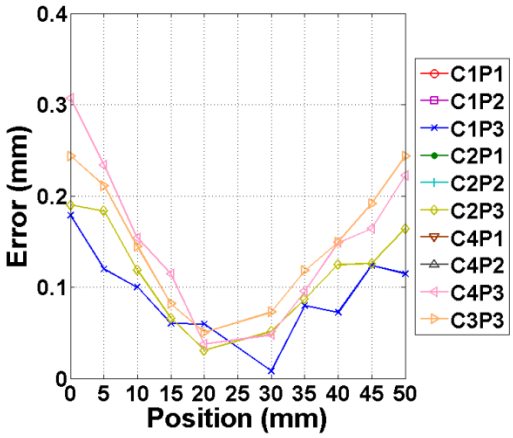
Error (mm)
Position (mm)
C1P1
C1P2
C1P3
C2P1
C2P2
C2P3
C4P1
C4P2
C4P3
C3P3

(f)

7.4.3 Mask Measurement with Consumer System

The same wooden mask as in Section 4.4.3 was measured using the consumer system, and the measurement result is shown in Figure 7-18. In the first row of Figure 7-18, three views of 3D point cloud data without texture show details of wrinkles and teeth. Three views of the same 3D point cloud data with texture overlaid onto every 3D point are shown in the second row. The measurement result of the wooden mask featuring a free-form surface and the accuracy assessment results in measuring the flat plate and spherical ball, together demonstrate that a system comprised of consumer components can measure surfaces with complex surface geometry, while maintaining sub-millimeter measurement accuracy. This sub-millimeter measurement accuracy would be more than sufficient for many consumer applications.

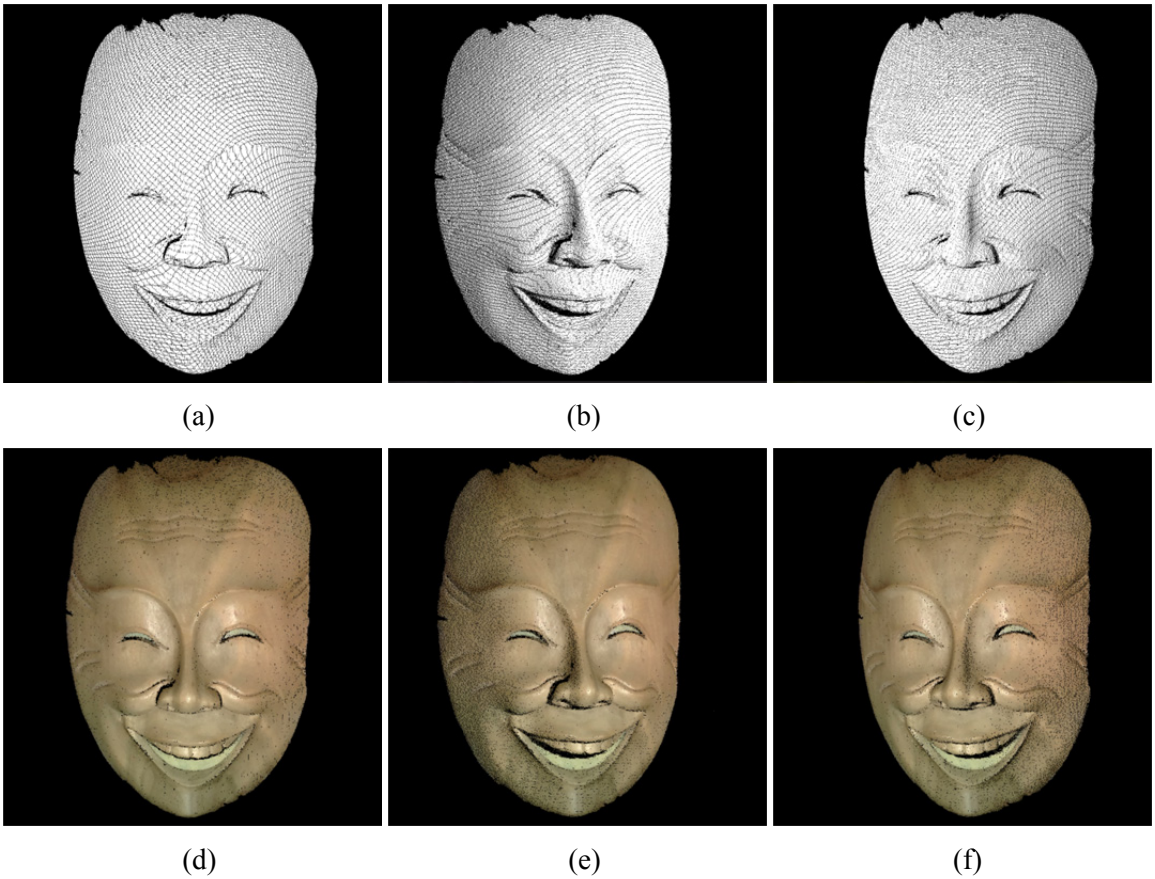

Figure 7-18 Mask measurement result with consumer system: (a-c) three views of point cloud data without texture; (d-f) three views of point cloud data with texture.

7.5 Summary

In designing a compact 3D surface-shape measurement system, the most compact measurement system that can be obtained for a desired accuracy can be determined from the information obtained by this compactness study. The smallest camera-projector angle (for the industrial system) or the smallest physical distance between the camera and projector (for the consumer system) that satisfies the desired accuracy would provide the most compact design. For the industrial system, all measurement results show that the requirements on measurement accuracy and compactness of the measurement system conflict and there is a tradeoff in loss of accuracy for increased compactness and loss of compactness for increased accuracy. If the tradeoff between accuracy and compactness does not satisfy design requirements, the improved methods of calibration and saturation avoidance in Chapter 4 to Chapter 6, which have demonstrated improved measurement accuracy, will contribute to enable a more compact design to achieve the desired measurement accuracy. For the consumer system, the results have demonstrated that the relation of system geometry and measurement precision is similar but may be slightly more complex. The compactness study was therefore necessary and useful for development of 3D scanners that implement fringe-projection phase-shifting profilometry. The compactness study also plays an important role in shortening the development cycle and saving development costs.

Chapter 8
Contributions and Future Work

This chapter summarizes contributions of the thesis research, and proposes future work.

8.1 Contributions

The main contributions of the research include the following:

(1) Improved system calibration and 3D measurement accuracies by new methods in Phase-Shifting Profilometry (PSP):

- an improved heterodyne phase unwrapping method that enables preservation of calibration points on the perimeter of the control-point grid, yielding a larger calibration volume. The method has also demonstrated greatly improved system calibration accuracy compared to calibration without such error compensation.
- An adaptive fringe-pattern projection (AFPP) method has been demonstrated to attain higher 3D measurement accuracy across a surface with a large range in reflectivity than measurement without AFPP. The method has also been demonstrated to handle varying luminance across the surface due to lighting and viewing angles in addition to surface reflectivity. Furthermore, the AFPP method avoids the many fringe-pattern projection and image-capture sets used in previous high-dynamic-range 3D imaging methods, and the added complexity of multiple camera viewpoints, projection directions, and optical and control hardware in other image saturation avoidance methods.
- A pixel-wise adaptive fringe-pattern projection (PWAFPP) method has been demonstrated to preserve all the advantages of the AFPP method over measurement with a global MIGL. More importantly, the method has also been demonstrated to improve the 3D measurement accuracy of measured 3D points suffering from residual image saturation after implementation of AFPP. The method can thus be used to measure surfaces with more complex variation in surface reflectivity.

(2) Better understanding of the relation of system geometry to measurement accuracy to facilitate designing the most compact measurement system that ensures a desired accuracy.

The most compact measurement system, more specifically, the smallest camera-projector angle (for the industrial system) or the smallest physical distance between the camera and projector (for the consumer system) that can be obtained for a desired accuracy can only be determined from the relation of system geometry to measurement accuracy obtained by a compactness study. Similarly, the best accuracy that can be obtained for a given compactness can be better understood. Generally, a wider camera-projector angle will allow greater measurement accuracy. However, the camera-projector pixel ratio is also an important factor that the limits the proximity of the camera to the object that should be employed. Knowledge of the relation of system geometry to measurement accuracy thus plays an important role in shortening the system development cycle and saving development costs.

For the industrial system, all measurement results have shown that the requirements for higher measurement accuracy and greater compactness of the measurement system conflict. There is a tradeoff in loss of accuracy for increased compactness and loss of compactness for increased accuracy. If the tradeoff between higher accuracy and greater compactness does not satisfy design requirements, the improved methods of calibration and saturation avoidance, which have demonstrated improved measurement accuracy, will contribute to enable a more compact design to achieve the desired measurement accuracy. For the consumer system, the similar but slightly more complex measurement results compared to the industrial system, have demonstrated the necessity of the compactness study.

(3) Extended use of phase-shifting profilometry on consumer systems

The measurement results have demonstrated that a measurement system comprised of consumer components can measure complex free-form surfaces, while maintaining a sub-millimeter measurement accuracy. This industrial-level sub-millimeter accuracy would be more than sufficient for many consumer applications, and has never been achieved by any other existing 3D scanner design for the consumer. This research thus contributes to enabling

common people to conveniently get access to accurate 3D data for a wide range of everyday uses.

8.2 Future Work

There are several directions where this thesis research can be extended in future work:

(1) To design new test objects that will further demonstrate the advantages of PWAFPP over AFPP.

According to the measurement results of Board Two with stepped gray levels, error reduction by PWAFPP was demonstrated at measured 3D points suffering from remaining image saturation after implementation of AFPP. One possible reason for this is that there is not any gray level variation within a strip on Board Two. A board with continuous variation of gray levels across surface may show more reduction of error across the board. A board with random gray level distribution within a range of 0-255 may also further show how the PWAFPP performs better than the AFPP method in handling complex variation in surface reflectivity by pixel-wise MIGL adaptation.

(2) To improve image saturation avoidance methods

The AFPP and PWAFPP methods both use the Levenberg-Marquardt (L-M) algorithm in estimating the adapted MIGLs in Round Two. The L-M algorithm is required because the mapping of projector-input intensities to the camera-captured intensities follows a non-linear model largely dependent on the projector gamma nonlinearity. The L-M algorithm iteratively optimizes the parameter in the model; however, a linear intensity mapping could avoid the need for the L-M algorithm, and thus enable use of only two projected patterns with two uniform intensities for MIGL adaptation.

There are three possible approaches for attaining a linear intensity mapping. The first approach could be to use existing gamma-correction methods [68-69] to eliminate the non-linear response of video projectors. However, none of these methods eliminate the nonlinearity completely. The residue nonlinearity could still lead to errors in estimating the adapted MIGLs from two patterns. A second approach would be to investigate improvement

to gamma nonlinearity compensation. A third approach could be to use gamma-free projectors, which have been developed specifically for optical-metrology applications. A good example of those projectors can be found in [70]. At present, most gamma-free projectors are customized comprising high-end components. They are much more expensive and less compact than the off-the-shelf video projectors, such as the pico projector used in this research.

References

[1] F. Chen, G. M. Brown, and M. Song. 2000. Overview of three-dimensional shape measurement using optical methods. *Optical Engineering* 39(1):10-22.

[2] J. Salvi, J. Pagés, and J. Batlle. 2004. Pattern codification strategies in structured light systems. *Pattern Recognition* 37(4): 827-849.

[3] G. K. Knopf, J. Kofman. 2002. Surface reconstruction using neutral network mapping of range-sensor images to object space. *Journal of Electronic Imaging* 11(2): 187-194.

[4] J. Kofman, J. T. Wu, and K. Borribanbunpotkat. 2007. Multiple-line full-field laser-camera range sensor. *Proceedings of SPIE* 6718: 67180A.

[5] M. Halioua, H. C. Liu. 1989. Optical three-dimensional sensing by phase measuring profilometry. *Optics and Lasers in Engineering* 11(3): 185-215.

[6] V. Srinivasan, H. C. Liu, and M. Halioua. 1984. Automated phase-measuring profilometry of 3-D diffuse objects. *Applied Optics* 28(18): 3105-3110.

[7] M. Kujawinska. 1991. Spatial-carrier phase-shifting technique of fringe pattern analysis. *Proceedings of SPIE* 1508: 61-67.

[8] M. Takeda, K. Mutok. 1983. Fourier transform profilometry for the automatic measurement 3-D object shapes. *Applied Optics* 22(24): 3977-3982.

[9] A. Dursun, S. Ozder, and F. N. Ecevit. 2004. Continuous wavelet transform analysis of projected fringe patterns. *Measurement Science and Technology* 15(9): 1768-1772.

[10] Q. Hu, K. G. Harding. 2007. Conversion from phase map to coordinate: Comparison among spatial carrier, Fourier transform, and phase shifting methods. *Optics and Lasers in Engineering* 45(2): 342-348.

[11] L. Huang, Q. Kemao, B. Pan and A. K. Asundi. 2010. Comparison of Fourier transform, windowed Fourier transform, and wavelet transform methods for phase extraction from a single fringe pattern in fringe projection profilometry. *Optics and Lasers in Engineering* 48(2): 141-148.

[12] C. Quan, W. Chen, and C. J. Tay. 2010. Phase-retrieval techniques in fringe-projection profilometry. *Optics and Lasers in Engineering* 48(2): 235-243.

[13] D. W. Phillion. 1997. General methods for generating phase-shifting interferometry algorithms. *Applied Optics* 36(31), 8098-8115.

[14] N. A. Dodgson. 2005. Autostereoscopic 3D Displays. *IEEE Computer* 38(8): 31-36.

[15] T. Judge, P. J. Bryanston-Cross. 1994. A review of phase unwrapping techniques in fringe analysis. *Optics and Lasers in Engineering* 21(4): 199-239.

[16] E. Zappa, G. Busca. 2008. Comparison of eight unwrapping algorithms applied to Fourier-transform profilometry. *Optics and Lasers in Engineering* 46(2): 106-116.

[17] S. Zhang, P. Huang. 2006. Novel method for structured light system calibration. *Optical Engineering* 45(8): 083601.

[18] W. Krattenthaler, K. J. Mayer, and H. P. Duwe. 1993. 3D-suface measurement with coded light approach. *Proceedings of the Őesterr Arbeitsgem Musterer Kennung* 12:103-114.

[19] J. M. Huntley, H. O. Saldner. 1993. Temporal phase-unwrapping algorithm for automated interferogram analysis. *Applied Optics* 32(17): 3047-3052.

[20] J. M. Huntley, H. O. Saldner. 1997. Error reduction methods for shape measurement by temporal phase unwrapping. *Journal of Optical Society of America A* 14(12): 318-396.

[21] J. M. Huntley, H. O. Saldner. 1997. Shape measurement by temporal phase unwrapping: comparison of unwrapping algorithms. *Measurement Science and Technology* 8: 986-992.

[22] C. E. Towers, D. P. Towers, and J. D. C. Jones. 2005. Absolute fringe order calculation using optimized multi-frequency selection in full-field profilometry. *Optics and Lasers in Engineering* 43(7): 788-800.

[23] H. Zhao, W. Chen, and Y. Tan. 1994. Phase-unwrapping algorithm for the measurement of three-dimensional object shapes. *Applied Optics* 33(20): 4494-4500.

[24] W. Nadeborn, P. Andrä, and W. Osten. 1996. A robust procedure for absolute phase measurement. *Optics and Lasers in Engineering* 24(2): 245-260.

[25] C. Reich, R. Ritter, and J. Thesing. 1997. White light heterodyne principle for 3D-measurement. *Proceedings of SPIE* 3100: 236-244.

[26] Asundi, W. Zhou. 1999. Unified calibration technique and its application in optical triangular profilometry. *Applied Optics* 38(16): 3556-3561.

[27] W. S. Li, X. Y. Su, Z. B. Liu. 2001. Large-scale three-dimensional object measurement: a practical coordinate mapping and image data-patching method. *Applied Optics* 40(20): 3326-3333.

[28] H. Guo, H. He, Y. Yu, and M. Chen. 2005. Least-squares calibration method for fringe projection profilometry. *Optical Engineering* 44(3): 033603.

[29] J. Vargas, M. A. Vaz. 2007. Linear calibration procedure for the phase-to-height relationship in phase measurement profilometry. *Optics Communications* 274(2): 307-314.

[30] P. Jia, J. Kofman, and C. English. 2007. Comparison of linear and nonlinear calibration methods for phase-measuring profilometry. *Optical Engineering* 46(4): 043601.

[31] Z. Zhang, C. E. Towers, and D. P. Towers. 2007. Uneven fringe projection for efficient calibration in high-resolution 3D shape metrology. *Applied Optics* 46(24): 6113-6119.

[32] Z. Wang, H. Du, and H. Bi. 2006. Out-of-plane shape determination in generalized fringe projection profilometry. *Optics Express* 14(25): 12122-12133.

[33] H. Du, Z. Wang. 2007. Three-dimensional shape measurement with an arbitrarily arranged fringe projection profilometry system. *Optics Letters* 32(16): 2438-2440.

[34] L. Chen, C. Quan. 2005. Fringe projection profilometry with nonparallel illumination: a least-squares approach. *Optic Letters* 30(16): 2101-2103.

[35] G. Sansoni, M. Carocci, and R. Rodella. 2000. Calibration and performance evaluation of a 3-D imaging sensor based on the projection of structured light. *IEEE Transactions on Instrumentation and Measurement* 49(3): 628-636.

[36] Q. Hu, P. S. Huang, Q. Fu, and F. Chiang. 2003. Calibration of a three-dimensional shape measurement system. *Optical Engineering* 42(2): 487-493.

[37] C. S. Yu, Q. J. Peng. 2007. A unified-calibration method in FTP-based 3D data acquisition for reverse engineering. *Optics and Lasers in Engineering* 5(3): 396-404.

[38] E. Zappa, and G. Busca. 2009. Fourier-transform profilometry calibration based on an exhaustive geometric model of the system. *Optics and Lasers in Engineering* 47(7-8): 754-767.

[39] J. Li, L. G. Hassebrook. 2000. Robust SVD-based calibration of active range sensor. *Proceedings of SPIE* 4041: 68-87.

[40] R. Legarda-Sáenz, T. Bothe, and W. P. Jüptner. 2004. Accurate procedure for the calibration of a structured light system. Optical Engineering 43(2): 464-471.

[41] Z. Li, Y. Shi, C. Wang, and Y. Wang. 2008. Accurate calibration method for a structured light system. *Optical Engineering* 47(5): 053604.

[42] R. Y. Tsai. 1987. A versatile camera calibration technique for high accuracy 3D machine vision metrology using off-the-shelf TV cameras and lenses. *IEEE Journal of Robotics and Automation* RA-3(4): 323-344.

[43] Z. Zhang. 2000. A flexible new technique for camera calibration. *IEEE Transactions On Pattern Analysis* 22(11): 1330-1334.

[44] G. H. Liu, X. Y. Liu, and Q. Y. Feng. 2011. 3D shape measurement of objects with high dynamic range of surface reflectivity. *Applied Optics* 50(23), 4557-4565.

[45] R. M. Kowarschik, J. Gerber, G. Notni, and W. Schreiber. 2000. Adaptive optical three-dimensional measurement with structured light. *Optical Engineering* 39(1), 150-158.

[46] K. Richard, G. Jorg, and N. Gunther. 1999. Adaptive optical 3D-measurement with structured light. *Proceedings of SPIE* 3824: 169-178.

[47] S. Umeyama, G. Godin. 2004. Separation of diffuse and specular components of surface reflection by use of polarization and statistical analysis of images. *IEEE Transactions On Pattern Analysis and Machine Intelligence* 26(5): 639-647.

[48] B. Salahieh, Z. Chen, J. J. Rodriguez, and R. Liang. 2014. Multi-polarization fringe projection for high dynamic range objects. *Optics Express* 22(8): 10064-10071.

[49] Y. Chen, Y. He, and E. Hu. 2008. Phase deviation analysis and phase retrieval for partial intensity saturation in phase-shifting projected fringe profilometry. *Optics Communications* 281: 3087-3090.

[50] S. Zhang, S. Yau. 2009. High dynamic range scanning technique. *Optical Engineering* 48(3): 033604.

[51] H. Z. Jiang, H. J. Zhao, and X. D. Li. 2012. High dynamic range fringe acquisition: a novel 3-D scanning technique for high-reflective surfaces. *Optics and Lasers in Engineering* 50(10): 1484-1493.

[52] C. Waddington, J. Kofman. 2010. Analysis of measurement sensitivity to illuminance and fringe-pattern gray levels for fringe-pattern projection adaptive to ambient lighting. Optics and Lasers in Engineering 48(2): 251-256.

[53] C. Waddington, J. Kofman. 2010. Saturation avoidance by adaptive fringe projection in phase-shifting 3D surface-shape measurement. *Proceedings of International Symposium on Optomechatronic Technologies*, IEEE, DOI 10.1109/ISOT.2010.5687390.

[54] C. Waddington. 2010. Adaptive fringe pattern projection techniques for image saturation avoidance in 3D surface measurement. Master Thesis, Department of Systems Design Engineering, University of Waterloo.

[55] J. Jeong, D. Hong, and H. Cho. 2007. Measurement of partially specular objects by controlling imaging range. *Proceedings of SPIE* 6718:671808.

[56] T. Bothe, W. Osten, A. Gesierich, and W. Jüptner. 2002. Compact 3D-Camera. *Proceedings of SPIE* 4778: 48-59.

[57] C. Munkelt, C. B. Burchardt, P. Kühmstedt, I. Schmidt, and G. Notni. 2007. Cordless hand-held optical 3D sensor. *Proceedings of SPIE* 6618: 66180D.

[58] P. Kühmstedt, C. B. Burchardt, C. Munkelt, M. Heinze, M. Palme, I. Schmidt, J. Hintersehr, and G. Notni. 2007. Intraoral 3D scanner. *Proceedings of SPIE* 6762: 67620E.

[59] L. Chen, C. Huang. 2005. Miniaturized 3D surface profilometer using digital fringe projection. *Measure Science and Technology*. 16: 1061-1068.

[60] G. Abramovich, K. Harding. 2010. A hand held triangulation sensor for small features measurement. *Proceedings of SPIE* 7855: 78550F.

[61] L. Huang, S. S. Chung, C. P. Lee, P. S. K. Chua, A. Asundi. 2010. Compact fringe projection profilometer. *Proceedings of SPIE* 7522: 752256.

[62] W. Lohry, Y. Xu, and S. Zhang. 2009. Optimal checkerboard selection for structured light system calibration. *Proceedings of SPIE* 7432: 743202.

[63] T. Yoshizawa, T. Wakayama, and H. Takano. 2007. Applications of a MEMS scanner to profile measurement. *Proceedings of SPIE* 6762:67620B.

[64] T. Wakayama, T. Yoshizawa. 2012. Compact camera for three-dimensional profilometry incorporating a single MEMS mirror. *Optical Engineering* 51(1): 013601.

[65] C. Bräuer-Burchardt, M. Möller, C. Munkelt, M. Heinze, P. Kühmstedt, and G. Notni. 2013. On the accuracy of point correspondence methods in three-dimensional measurement systems using fringe projection. *Optical Engineering* 52(6): 063601.

[66] D. Li, H. Zhao, and H. Jiang. 2010. Fast phase-based stereo matching method for 3D shape measurement. *Proceedings of International Symposium on Optomechatronic Technologies*, IEEE, 10.1109/ISOT.2010.5687348.

[67] S. Suzuki and K. Abe. 1985. Topological structural analysis of digitized binary images by border following. *Computer Vision, Graphics, and Image Processing* 30(1): 32-46.

[68] C. R. Coggrave, J. M. Huntley. 1999. High-speed surface profilometer based on a spatial light modulator and pipeline image processor. *Optical Engineering* 38(9): 1573-1581.

[69] P. Huang, C. Zhang and F. Chiang. 2003. High-speed 3-D shape measurement based on digital fringe projection. *Optical Engineering* 42(1): 163-168.

[70] H. Zhao, X. Liang, X. Diao and H. Jiang. 2014. Rapid in-situ 3D measurement of shiny object based on fast and high dynamic range digital fringe projector. *Optics and Lasers in Engineering* 54: 170-174.